Universidad Técnica Federica Santa María
Departamento de Física

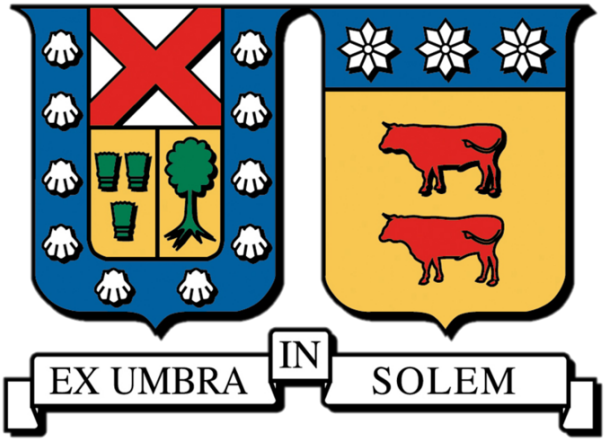

Background estimation in the search for non-resonant Higgs boson pair production in the $bb\tau\tau$ decay channel using 13 TeV pp collision with data from the ATLAS detector

A dissertation submitted to the University Federico Santa Maria
in partial fulfillment of the requirements for
the degree of Master of Physics

Cristian Andres Allendes Flores.
Advisor: Edson Carquín.

Acknowledgements

I would like to first thank my partner and daughter, who inspired me to persevere through this process. I am grateful for their support.

Next, I would like to express my gratitude to my professor, Professor Edson, allowed me the opportunity to work with one of the largest scientific collaborations. Being a part of ATLAS experiment, analyzing and working as a shifter in the ATLAS control room was a defining moment in my career as a physicist.

I would also like to thank the Academia Sinica Institute for providing me with a place to work. Special thanks go to Shahzad Ali Khan, who not only worked alongside me and became a close friend .

Lastly, I am thankful to my friend Nicolas Hermosilla, who always had time to help me whenever I made a mistake in the terminal.

Contents

List of Figures

List of Tables

Chapter 1

Introduction

1.1 Overview

The Standard Model of particle physics (SM) is a theory formalized in the 1960s to describe the fundamental particles. It encapsulates our current best understanding of the fundamental particles which make up everything in the Universe and the fundamental forces through which they interact. As a relativistic Quantum Field Theory (QFT), it treats fundamental particles as excited states of quantum fields, which are defined at all points in space-time. It provides a mathematical formulation for three of the four known fundamental forces – the strong, weak and electromagnetic interactions – the fourth being the gravitational force. According to the SM, 10^{-12} seconds after the Big Bang, the Universe transitioned into the lowest energy state of the Brout-Englert-Higgs (BEH) energy potential inducing the 'spontaneous' breaking of the electroweak symmetry (EWSB), generating physical masses to the weak force carriers (the W and Z vector bosons). This process is known as the BEH mechanism, which also postulates the existence of a fundamental scalar, the Higgs boson (H). Quarks and leptons, the building blocks of matter, obtained their masses from their interactions with it. Moreover, the Higgs boson interaction with itself is responsible for its own mass (m_H) [C$^+$12].

The Standard Model has been hihgly successful so far. In several cases, particles were predicted before their direct experimental observation. Calculations of process rates agree very well with the experimental observation. One of the greatest successes is the calculation of the magnetic dipole moment of the electron. When the Dirac equation was introduced, it predicted a factor 2 compared to the dipole moment of a rotating mass, which agreed with experimental observations at that time. When higher precision data became available deviations were found, at the order of 1h. However the theoretical predictions improved once higher order corrections were added. The factor is today the most precisely measured quantity in physics, known to 12 digits [OAA$^+$14]. So far, no deviation from the theoretical calculation has been found.

In 2012, almost five decades after Peter Higgs et al. published their famous theoretical predictions [EB64, Hig64a, GHK64, Hig64b] CERN Large Hadron Collider (LHC) was able to discover the elusive Higgs particle of the Standard Model. Designed to produce proton-proton (pp) collisions at a center-of-mass energy of $\sqrt{13}$. The (ATLAS) and Compact Muon Solenoid (CMS) experiments in the year of 2012 started a new era for experimental physics, this was the the first confirmation of the existence of the BEH mechanism, and with this we began to explore the mechanism of electroweak symmetry breaking [AA$^+$12, C$^+$12]. Different experiments have studied the physical properties of the Standard Model Higgs and demonstrated that the observed boson is consistent with the theoretically predicted Higgs particle with a mass [EB64, Hig64a, GHK64, Hig64b] around $125.09 \pm 0.24\ GeV$.

This discovery has sparked a new chapter of high-energy physics (HEP) with two main objectives: the precise determination of the properties of the Higgs boson and the search for new physics beyond the Standard Model (BSM).

In the SM, Higgs boson pairs can be produced at the LHC via gluon-gluon fusion (ggF) or through top-quark loops on LHC, as well as the triple Higgs self-interaction, which is predicted in the Standard Model. Thus, studying the Higgs trilinear self-interaction(λ_{hhh}) will be the final examination of the Higgs mechanisms corresponding to the electroweak symmetry breaking. In fact, the future particle accelerator High Luminosity LHC aims for this as one of the primary goals too. Thus precise measurements of the Higgs boson couplings are essential to test the validity of the Brout-Englert-Higgs mechanism, the electroweak theory, and the SM theory itself, as all the couplings are predicted by the SM theory, given the measured values of the masses of the particles and of the vacuum expectation value. The triple Higgs self-coupling (

λ_{hhh}) is present in the SM theory and, its value, corresponding in the theory to $m_H^2/2\nu$, controls the shape of the Higgs potential. The direct way to measure this coupling is by studying the Higgs boson pair production process.

However, the top quark loop di-Higgs production mode and the self-interaction di-Higgs production mode have a negative interference between each other which leads to an extremely small total cross section, which is $\sim 33.41\ fb$ at 13 TeV center-of-mass energy [dF$^+$17, BGH$^+$16] which is three orders of magnitude smaller than the single Higgs boson production cross section. Observing this process and measuring the Higgs self-coupling λ is thus HHH, particularly challenging because of its small cross-section, and it is one of the main goals for the High Luminosity LHC.

It is impossible for the LHC to produce enough luminosity for detecting the pair-production of Standard Model Higgs now, not to say to reach the sensitivity to be able to see the Higgs self-interaction, which has an even smaller cross section. However, it is still significant to conduct a study on the pair-production(Non-Resonant) of the Standard Model Higgs using the recorded data on ATLAS now, as this study will give us a hint about the sensitivity we could reach right now and how much data we will need in the future on the High Luminosity LHC. More importantly, through the decomposition of the experimental errors, we will be able to know what we should do to improve the sensitivity in the future.

The SM is a beautiful and successful description of nature. The SM predictions have been corroborated at particle colliders such as LEP, Tevatron, and LHC. However, it does not provide explanations for some SM features

1 Dark Matter

2 Quantum Gravity

3 Baryon Asymmetry

4 Hierarchy Problem

5 Neutrino Oscillation

Gravity could be one of the most significant obstacles lying on the road. The Standard Model theory gives no single hint on the gravity force or graviton particles. Thus, physicists worked out different models beyond the Standard Model (BSM) to include for example the graviton into the current theoretical framework. The spin-2 Kaluza-Klein excitations of the graviton in the bulk Randall-Sundrum model [RS99] is one of these models which introduces an extra dimension to include the gravitons. The model predicts the process that the RS graviton decays to two Standard Model Higgs. At the same time, there are also other models physicists proposed beyond the Standard Model to cover the shortages of the Standard Model. The Two Higgs Doublet Model(2HDM) [Lee73, HK85] is one of these by extending the Higgs field to two doublets fields. The 2HDM model predicts extra heavy CP, even Higgs, which could decay to two Standard Model Higgs too. The cross sections of the RS graviton decaying to Standard Model Higgs and heavy Higgs decaying to Standard Model Higgs could be significantly enhanced in their corresponding theories. Also modifications to the top-quark Yukawa coupling or the Higgs self-coupling, or the presence of new diagrams with new vertices, could enhance the di-Higgs production rate and modify the kinematic properties of the process showing hints of possible new physics BSM in the non-resonant di-Higgs production.

We choose the final state with one of the Standard Model Higgs decaying to two b quarks and one Higgs decaying to two τ leptons. The $bb\tau^+\tau^-$ channel has the third largest branching fraction(7.4%) among all the Di-Higgs decay channels with a relatively clean signature compared with the channels with larger branching fractions($bbbb$ and $bbWW$) [Mor17]. This is the reason why we choose the $bb\tau\tau$ channel to do the study.

1.2 Brief Review of the Standard Model

The Standard Model is a powerful theoretical framework that describes the phenomena observed in particle physics experiments. We use natural units in this analysis: $c = \hbar = 1$, where c is the speed of light, and $\hbar$ is the reduced Planck constant. Energy, momentum, and mass are

expressed in the same unit, electron volt (eV), under the natural units. After a brief overview of the Standard Model, we discuss in more detail the model considered in this research.

The SM is a relativistic quantum field theory (QFT) that describes how matter can occur in two basic types called quarks and leptons. The fundamental interactions that this theory consider are: Strong, Electromagnetic and Weak, except gravity. Since gravity is much weaker than the other three forces, it does not affect particle physics. Hence, it will not be considered here.

These elementary fermions and quarks, which are considered now 'matter' fields interact among themselves through the electromagnetic, weak and strong interactions mediated by gauge bosons fields. These interactions (forces) that are mediated by bosons, are described based on a gauge-symmetry in $SU(3)_C \otimes SU(2)_L \otimes SU(1)_Y$. Each of these groups consists of six particles, which are organized in pairs, called "generations", having the same properties except the mass. The six quarks are paired in three generations: the up quark⊓ and the "down quark"(d) form the first generation, followed by the charm quark (c) and strange quark (s) forming the second generation, then the "top quark" (t) and "bottom quark"(b) in the third generation. Quarks are all electrically charged, with up-type quarks having charge $+2/3$ and down-type quarks $-1/3$, and also carry a "color" charge (R, G, B). The six leptons are similarly arranged in three generations: the "electron" and the "electron neutrino", the "muon" and the "muon neutrino", and the "tau" and the "tau neutrino". There are three electrically charged leptons ($-l$) while the neutrinos are electrically neutral. These are (ν_l): electron ($-e$), muon (ν^-) and tau ($\tau-$) with charge -1, the neutral particles are: e-neutrino (ν_e), μ-neutrino (ν_μ) and τ-neutrino (τ_ν).

It provides a mass generation mechanism through a scalar field sector. The underlying foundation of the SM is built on the concepts of local gauge symmetry and spontaneous symmetry breaking. It does not include a description of the gravitational interaction, which has a negligible impact at the sub-nuclear scales.

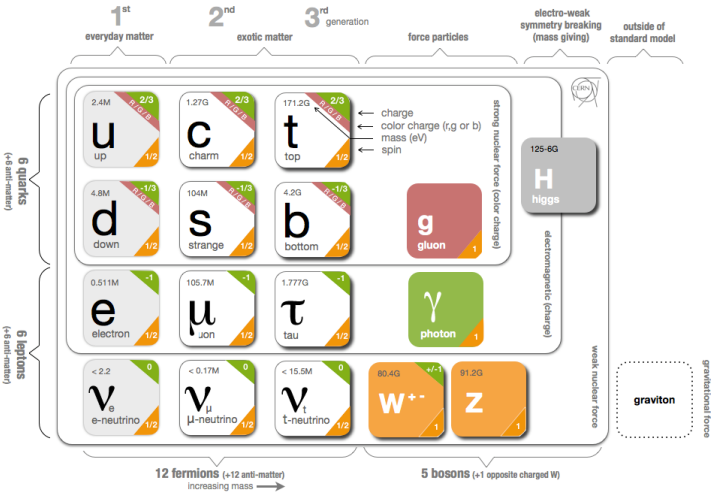

Figure 1.1: Standard model of elementary particles and interactions [Pur12]

The strong, weak and electromagnetic force carriers are the gluons (g), massive vector bosons ($W\pm$ and Z), and the photon (γ), respectively. The last piece is the Higgs boson (H), which is the only elementary scalar is associated with the generation of mass. A summary of the properties and interactions of the SM elementary particles are presented in Figure 1.1. Quarks interact through the strong, weak and electromagnetic interactions, whereas leptons only participate in weak and electromagnetic (if electrically charged) interactions.

Chapter 2

The Standard Model and Beyond

2.1 The Standard Model of Particle Physics overview

The Standard Model of particle physics is the theory that describes three of the four known fundamental interactions, namely the electromagnetic, weak, and strong interactions. It does not include the gravitational interaction.

The Standard Model is a relativistic gauge of quantum field theory (QFT), incorporating special relativity and quantum mechanics. It is based on the symmetry principles, the mathematics of which is provided by group theory. Indeed, the SM is a non-Abelian* gauge theory based on a product of the (special) unitary groups $SU(3)_C \otimes SU(2)_L \otimes U(1)_Y$, where $U(N)$ refers to a group of $N \times N$ unitary matrices and $SU(N)$ is the subset of $U(N)$ with unitary matrices of determinant equal to one.

- The group $SU(3)_C$ describes quantum chromodynamics (QCD), which parameterizes the strong interaction; the letter C refers to the color charge.
- The group $SU(2)_L \otimes U(1)_Y$ constitutes the electroweak interaction, which combines electromagnetism and the weak force. The letter L stands for left and indicates that the symmetry only involves left-handed particles. The letter Y stands for the weak hypercharge, which is related to the electric charge (Q) and the weak isospin (T) by the formula $Q = T_3 + Y/2$, with T_3 being the third component of the weak isospin.

One of the most important consequences of symmetry considerations is the so-called Noether's theorem [Noe71], which states that for every continuous symmetry there is an associated conservation law. Therefore, each group in the SM introduces a conserved quantity denoted by the indices c, L and Y, which represent color, weak isospin, and weak hypercharge, respectively. This theory describes particles as excitations of quantum fields and interactions related to local gauge symmetries of the Lagrangian under local phase transformations of the previously mentioned symmetry group. This introduces the presence of massless boson fields, which are interpreted as the quanta mediating the interaction.

The fields in the SM are described according to the Lagrangian formalism. The SM Lagrangian density (more commonly referred to as simply the Lagrangian), L_{SM}, is constructed from four sectors:

$$\mathcal{L}_{\text{SM}} = \mathcal{L}_{\text{QCD}} + \mathcal{L}_{\text{EW}} + \mathcal{L}_{\text{Higgs}} + \mathcal{L}_{\text{Yukawa}} \tag{2.1}$$

where:

- $\mathcal{L}_{\text{QCD}}$ corresponds to the QCD sector and is responsible for the strong interaction; only quarks and gluons participate in this sector.
- $\mathcal{L}_{\text{EW}}$ corresponds to the electroweak sector. After Electroweak Symmetry Breaking (EWSB), one part will correspond to the electric interaction, involving the photon. The other part is the Weak interaction, whose mediators are the $W^{\pm}$ and Z, two massive bosons responsible for the nuclear decay.
- $\mathcal{L}_{\text{Higgs}}$ is responsible for breaking of the electroweak sector and the mass generation of every massive particle in the SM (except neutrinos).
- $\mathcal{L}_{\text{Yukawa}}$ corresponds to the interaction section between the Higgs and Fermions.

*The group is non-Abelian due to the inclusion of the $SU(3)_C$ and $SU(2)_L$ groups, both of which have non-commuting gauge transformations. The $U(1)_Y$ group is Abelian

2.2 Quantum Electrodynamics (QED)

One of the most important and successful modern examples of gauge QFT is Quantum Electrodynamics (QED). It was the first relativistic gauge quantum field theory historically developed and, describes the dynamics of the interactions of fermions with the electromagnetic field.

The predictions of QED have been successfully tested by very high-precision experiments [Kar05]. One of the greatest successes of the theory was calculating of the anomalous magnetic dipole moment of the electron. The first-order QED contribution was first found by Julian Schwinger in 1948 to be $\alpha/2\pi$.

QED is derived using symmetry arguments, especially the invariance under local phase transformations. A free spin-1/2 fermion is described by the Dirac Lagrangian,

$$\mathcal{L}_{\text{Dirac}} = \bar{\psi}\Big(i\gamma^{\mu}\partial_{\mu} - m\Big)\psi \tag{2.2}$$

where ψ is the 4-component Dirac spinor of the fermion field (the particle's wave function), $\bar{\psi} = \psi\gamma^0$ is the adjoint spinor, γ^{μ} are the Dirac matrices, and $\partial_{\mu} = \partial/\partial x_{\mu}$ are the partial derivatives. The Euler-Lagrange equations associated with this Lagrangian results in the famous Dirac equation:

$$\Big(i\gamma^{\mu}\partial_{\mu} - m\Big)\psi = 0 \tag{2.3}$$

The Dirac Lagrangian is invariant under a global symmetry $\mathrm{U}(1)_{\mathrm{EM}}$, a group of unitary 1×1 matrices. They correspond to rotations $e^{iq\theta}$ (does not vary with space-time coordinate) on the complex plane. The invariance can be shown explicitly by rotating the fermionic field ψ as follows:

$$\begin{aligned}\psi \to \psi^{'} &= e^{iq\theta}\psi \\ \bar{\psi} \to \bar{\psi}^{\prime} &= e^{-iq\theta}\bar{\psi}\end{aligned}$$

Now by plugging in the rotated fields into the Dirac Lagrangian (2.2), we obtain:

$$\begin{aligned}\mathcal{L} \to \mathcal{L}^{'} &= \bar{\psi}^{\prime}\Big(i\gamma^{\mu}\partial_{\mu} - m\Big)\psi^{'} \\ &= e^{-iq\theta}\bar{\psi}\Big(i\gamma^{\mu}\partial_{\mu} - m\Big)e^{iq\theta}\psi \\ &= e^{-iq\theta}e^{iq\theta}\bar{\psi}\Big(i\gamma^{\mu}\partial_{\mu} - m\Big)\psi \\ &= \bar{\psi}\Big(i\gamma^{\mu}\partial_{\mu} - m\Big)\psi \\ &= \mathcal{L}\end{aligned} \tag{2.4}$$

Therefore, the Lagrangian stays invariant under this transformation. Since the parameter θ is kept constant, this is called a GLOBAL TRANSFORMATION.

Now, we want to introduce interactions into the framework, which can be done by invoking the principle of gauge invariance. This principle states that global phase transformations of fields must be promoted to local ones, and the Lagrangian should not be modified by more than a total derivative; this way, the equations of motion remain unchanged. Namely, this means that the previous global phase transformation θ now needs to depend on the space-time coordinates. The spinor now transforms as $\psi \to \psi^{'} = e^{i\theta(x)}\psi(x)$, where $\theta(x)$ is an arbitrary smooth function that defines the local phase transformation, which belongs to the unitary abelian symmetry group U(1). However, note that the above condition is not fulfilled since:

$$
\begin{aligned}
\mathcal{L}_D \to \mathcal{L}_D^{'} &= e^{-iq\theta(x)}\bar{\psi}\Big(i\gamma^\mu\partial_\mu - m\Big)e^{iq\theta(x)}\psi \\
&= e^{-iq\theta}e^{iq\theta}\bar{\psi}\Big(i\gamma^\mu\partial_\mu - m\Big)\psi + ie^{-iq\theta(x)}\bar{\psi}\gamma^\mu\psi(x)\partial_\mu\Big[e^{iq\theta(x)}\Big] \\
&= \bar{\psi}\Big(i\gamma^\mu\partial_\mu - m\Big)\psi - qe^{-iq\theta(x)}e^{iq\theta(x)}\bar{\psi}\gamma^\mu\psi(x)\partial_\mu\Big[\theta(x)\Big] \\
&= \bar{\psi}\Big(i\gamma^\mu\partial_\mu - m\Big)\psi - q\bar{\psi}\gamma^\mu\psi(x)\partial_\mu\Big[\theta(x)\Big] \\
&= \mathcal{L} - q\bar{\psi}\gamma^\mu\psi(x)\partial_\mu\Big[\theta(x)\Big]
\end{aligned} \tag{2.5}
$$

The Lagrangian is not invariant under this transformation due to the $q\bar{\psi}\gamma^\mu\psi(x)\partial_\mu\partial_\mu\theta(x)$ term. It is necessary to introduce a gauge field $A_\mu(x)$, which is the photon field and transforms as:

$$
A_\mu \to A_\mu^{'} = A_\mu - \partial_\mu\theta(x) \tag{2.6}
$$

The term previously violated the invariance. The ordinary derivative ∂_μ can now be replaced with the covariant derivative D_μ defined as

$$
D_\mu(x)\psi(x) = \Big[\partial_\mu + iqA_\mu\Big]\psi(x) \tag{2.7}
$$

Using the Lagrangian with the covariant derivative $\mathcal{L}_{inv} = \bar{\psi}(i\gamma^\mu D_\mu - m)\psi$ and the transformation rules 2.7 and 2.6, we obtain:

$$
\begin{aligned}
\mathcal{L}_{\text{inv}} \to \mathcal{L}_{\text{inv}}^{'} &= \bar{\psi}^{'}(i\gamma^\mu D_\mu - m)\psi^{'} \\
&= e^{-iq\theta(x)}\bar{\psi}\Big(i\gamma^\mu D_\mu - m\Big)e^{iq\theta(x)}\psi \\
&= e^{-iq\theta(x)}\bar{\psi}\Big(i\gamma^\mu\Big[\partial_\mu + iqA_\mu^{'}\Big] - m\Big)e^{iq\theta(x)}\psi \\
&= e^{-iq\theta(x)}\bar{\psi}\Big(i\gamma^\mu\Big[\partial_\mu + iq\{A_\mu - \Big(\partial_\mu\theta(x)\Big)\}\Big] - m\Big)e^{iq\theta(x)}\psi \\
&= e^{-iq\theta(x)}\bar{\psi}\Big(i\gamma^\mu\Big[\partial_\mu e^{iq\theta(x)}\psi\Big] - q\gamma^\mu A_\mu e^{iq\theta(x)} + qe^{iq\theta(x)}\gamma^\mu\Big[\partial_\mu\theta(x)\Big] - me^{iq\theta(x)}\Big)\psi \\
&= e^{-iq\theta(x)}\bar{\psi}\Big(ie^{iq\theta(x)}\gamma^\mu\partial_\mu\psi - \cancel{qe^{iq\theta(x)}\gamma^\mu\Big[\partial_\mu\theta(x)\Big]} - qe^{iq\theta(x)}\gamma^\mu A_\mu\psi \\
&\quad + \cancel{qe^{iq\theta(x)}\gamma^\mu\psi\Big[\partial_\mu\theta(x)\Big]} - me^{iq\theta(x)}\psi\Big) \\
&= e^{-iq\theta}e^{iq\theta}\bar{\psi}\Big(i\gamma^\mu\partial_\mu - q\gamma^\mu A_\mu - m\Big)\psi \\
&= \bar{\psi}\Big(\mathcal{D}_\mu - m\Big)\psi \\
&= \mathcal{L}_{inv}
\end{aligned} \tag{2.8}
$$

This is not the complete QED Lagrangian. We still need the description of photons by themselves. Therefore, we add a third term, L_γ , which corresponds to the photon propagator,

$$
\mathcal{L}_\gamma = -\frac{1}{4}F^{\mu\nu}F_{\mu\nu} \tag{2.9}
$$

where $F_{\mu\nu}$ is the electromagnetic field strength tensor given by $F_{\mu\nu} = \partial_\mu A_\nu - \partial_\nu A_\mu$.

Now, we can finally write the entire QED Lagrangian. The three generations of leptons, which are electrons, muons and taus, have the same coupling to photons, and in order to account for all of them, we sum over the leptonic terms.

$$
\begin{aligned}
\mathcal{L}_{QED} &= \sum\bar{\psi}\Big(i\gamma^\mu\mathcal{D}_\mu + m\Big)\psi - \frac{1}{4}F_{\mu\nu}F^{\mu\nu} \\
&= \underbrace{\bar{\psi}i\gamma^\mu\partial_\mu\psi}_{\substack{\text{fermion}\\ \text{kinematics}}} - \underbrace{\bar{\psi}m\psi}_{\substack{\text{fermion mass}\\ \text{term}}} + \underbrace{\bar{\psi}e\gamma^\mu A_\mu\psi}_{\substack{\text{electromagnetic}\\ \text{interaction}}} - \frac{1}{4}\underbrace{F_{\mu\nu}F^{\mu\nu}}_{\substack{\text{photon}\\ \text{kinematics}}}
\end{aligned} \tag{2.10}
$$

The term $\bar{\psi}e\gamma^\mu A_\mu\psi$ has emerged due to the demanding gauge invariance. This can be interpreted as a fermion with charge e interacting with an electromagnetic potential A_μ. The principle of gauge invariance gives a recipe for generating interaction terms between forces and particles.

Combined gauge and complex phase transformations are collectively referred to as $U(1)$ gauge transformations. A straightforward application of Noether's theorem shows that the $U(1)$ gauge symmetry of QED corresponds to the conservation of electric charge current.

Note that $\mathcal{L}_{QED}$ is not invariant if there is a mass term associated with the photon field (i.e., $1/2m_A^2 A^\mu A_\mu$) [CF12, Pes18]

2.3 Non-Abelian gauge theories

The weak and strong interactions are described by higher dimension symmetry groups $SU(n)$ with $n = 2$ and $n = 3$ for the weak and strong interactions, respectively. The Dirac fields are then n-plets (douplets or triplets) and transform as[†]:

$$\psi \to e^{i\theta_a(x)T_a} \tag{2.11}$$

The T_a matrices are the $n^2 - 1$ linearly independent generators of the symmetry group. The conventional choice in the case of $SU(2)$ is the three Pauli matrices, $T_a = 1/\sigma_a$, and the eight Gell-Mann matrices in the case of $SU(3)$, $T_a = 1/\lambda_a$. Per generator, a gauge field G_μ^a is introduced, transforming at first order as:

$$G_\mu^a \to G_\mu^a - \frac{1}{g}\partial_\mu\theta_a - f_{abc}\theta_b G_\mu^c \tag{2.12}$$

The additional last term is introduced to achieve local gauge invariance despite non-communiting generators, $[T_a, T_b] = ifabcT_c$. Symmetry groups with this behavior are called non-Abelian; in contrast, Abelian groups have all f_{abc} vanish. The $U(1)$ symmetry group this exemplifies the latter.

Figure 2.1: Gluons self interaction

The real-valued constants f_{abc} are called the structure constants of the group. With the coupling constant g and the covariant derivative $D_\mu = \partial_\mu + igT_aG_\mu^a$, the Lagrangian takes the form

$$\begin{aligned}\mathcal{L}_{QED} &= \bar{\psi}\Big(i\gamma^\mu\mathcal{D}_\mu + m\Big)\psi - \frac{1}{4}G_{\mu\nu}^a G^{a\mu\nu} \\ &= \underbrace{\bar{\psi}i\gamma^\mu\partial_\mu\psi}_{\substack{\text{fermion}\\\text{kinematics}}} - \underbrace{\bar{\psi}m\psi}_{\substack{\text{fermion mass}\\\text{term}}} + \underbrace{\bar{\psi}g\gamma^\mu T_a G_\mu^a\psi}_{\text{interaction}} - \frac{1}{4}\underbrace{G_{\mu\nu}^a G^{a\mu\nu}}_{\substack{\text{photon}\\\text{kinematics}}}\end{aligned} \tag{2.13}$$

The field strength tensor is defined as $G_{\mu\nu}^a = \partial_\mu G_\nu^a - \partial_\nu G_\mu^a - gf_{abc}G_\mu^b G_\nu^c$. Therefore, the last term in Eq. 2.13 contains additional terms describing self-interactions:

[†]Summation over the double appearing index a is again implied, $a = 1, ..., (n^2 - 1)$

$$G^a_{\mu\nu}G^{a,\mu\nu} = -\frac{1}{4}(\partial_\mu G^a_\nu - \partial_\nu G^a_\mu)(\partial^\mu G^{a,\nu} - \partial^\nu G^{a,\mu}) \qquad \text{kinematic term} \tag{2.14}$$

$$-\frac{1}{2}g f_{abc}(\partial_\mu G^a_\nu - \partial_\nu G^a_\mu)G^{b,\mu}G^{c,\nu} \qquad \text{3-point self interaction} \tag{2.15}$$

$$-\frac{1}{4}g^2 f_{abe}f_{cde}G^a_\mu G^b_\nu G^{c,\mu}G^{d,\nu} \qquad \text{4-point self interaction} \tag{2.16}$$

2.3.1 Glashow-Weinberg-Salam theory

The weak interaction cannot be described by a simple SU(2) Lagrangian, due to the following peculiarities:

- The observed vector bosons of the weak interaction, W and Z bosons, are massive. However it is not possible to add a mass term to the Lagrangian in Eq. 2.13 without violating local gauge invariance.
- The charged weak interaction mediates only between left-handed[‡] fermions and right-handed antifermions.
- The coupling strength of the neutral weak interaction dependens on the electromagnetic charge and chirality of the fermion.
- Besides charged current interactions of quarks within the same generation (ud/cs/tb), inter-generation interactions occur (us/ub/cd/cb/td/ts).

2.4 Weak Interaction

The theory of the electroweak interaction was proposed by Glashow, Salam and Weinberg [Gla61, Wei67, Sal68] to describe the electromagnetic and weak interactions between quarks and leptons, the theory for which the authors received a Nobel Prize in physics in 1979. The electromagnetic and weak interactions are combined as two aspects of the same force. Electroweak theory is based on the combination of the gauge symmetry groups $SU(2)_L \times U(1)_Y$. The non-Abelian special unitary group $SU(2)_L$ describes the fermion doublet fields, whilst an additional $U(1)_Y$ group is required to include the electromagnetic interaction, where L and Y are, respectively, the left-handed weak isospin and the weak hypercharge, related to the electric charge (Q) and the weak isospin (T) by the formula $Q = T_3 + Y/2$, which are the generators of the symmetry group.

The weak interaction is the only interaction violating parity symmetry $\mathcal{P}$. The parity operation flips the sign of a spatial coordinate. For example, $P_x x = -x$. The weak interaction also breaks charge conjugation parity symmetry CP, which on top of a parity transformation, also changes the particle into its antiparticle. This was first experimentally detected by looking at decays of $CP - odd K^0$ particles decaying into CP-even pions by Christenson et al in 1964 [CCFT64]. This symmetry breaking leads to the weak force coupling differently to left-handed and right-handed particles. The handedness is determined by a property called chirality. In the limit of a massless particle, it coincides with helicity, which is defined as the normalized projection of the spin vector onto the spatial momentum vector. For massive particles, helicity depends on the reference frame, whereas chirality is frame-invariant. The left and right handed fields can be obtained by operating the fields by the fifth Dirac gamma matrix $\gamma^5 = i\gamma^0\gamma^1\gamma^1\gamma^2\gamma^3$.

$$\gamma^5 = \begin{pmatrix} 0 & 0 & 1 & 0 \\ 0 & 0 & 0 & 1 \\ 1 & 0 & 0 & 0 \\ 0 & 1 & 0 & 0 \end{pmatrix} \tag{2.17}$$

[‡]Handedness in terms of chirality. For massless particles, chirality is identical to helicity, the spin-projection onto the direction of motion. A spin parallel to the momentum gives positive helicity (right-handed), while an anti-parallel spin gives negative helicity (left-handed)

The left and right handed fields have eigenvalues of ± 1 when operated by γ^5 . Therefore, we may write:

$$\psi = \psi_L \psi_R \tag{2.18}$$

$$\psi_R = \frac{1}{2}(1+\gamma^5)\psi \tag{2.19}$$

$$\psi_R = \frac{1}{2}(1-\gamma^5)\psi \tag{2.20}$$

Generation	Name	Symbol	Electric charge, $Q[e]$	Weak isospin, T_3	Mass $m[GeV]$
Quarks					
1	up	u	$+2/3$	$+1/2$	0.0023
	down	d	$-1/3$	$-1/2$	0.0047
2	charm	c	$+2/3$	$+1/2$	1.275
	strange	s	$-1/3$	$-1/2$	0.095
3	top	t	$+2/3$	$+1/2$	173.0
	bottom	b	$-1/3$	$-1/2$	4.18
Leptons					
1	electron	e	-1	$-1/2$	0.000511
	electron neutrino	ν_e	0	$+1/2$	$< 2 \times 10^{-9}$
2	muon	μ	-1	$-1/2$	0.106
	muon neutrino	ν_μ	0	$+1/2$	$< 2 \times 10^{-9}$
3	τ-lepton	τ	-1	$-1/2$	1.777
	τ-neutrino	ν_τ	0	$+1/2$	$< 2 \times 10^{-9}$

Table 2.1: The elementary fermions of the SM. [WO22]

This also allows us to separate the fermion Lagrangian as well.

$$L = L_L + L_R = \bar{\psi}_L(i\gamma^\mu \partial_\mu - m)\psi_L + \bar{\psi}_R(i\gamma^\mu \partial_\mu - m)\psi_R \tag{2.21}$$

The fermions in Table 2.1 are comprised of components with negative and positive chirality, referred to as left- and right-handed particles, respectively. Left-handed fermions are organized in $SU(2)_L$ doublets, ψ_L , with weak isospin component $T_3 = \pm 1/2$, whilst right-handed particles are represented by singlets, ψ_R, with $T_3 = 0$. The left-handed doublets interact through the weak force, while the right-handed singlets remain invariant under transformations of $SU(2)_L$. Fermions are organized in doublets with weak isospin $T = 1/2$ for the left-handed states and singlets with $T = 0$ for the right-handed ones:

$$\chi = \begin{pmatrix} \nu_l \\ l \end{pmatrix}_l, \begin{pmatrix} q^u \\ q^d \end{pmatrix}_l \tag{2.22}$$

$$\Psi_R = l_R, q^u_R, q^d_R \tag{2.23}$$

With l indicating charged leptons $(e, , \nu, \tau)$, ν_l the corresponding neutrinos and $q^{u,d}$ the up-type and down-type quarks (up type u, c, t and down type d, s, b), the subscript R also run trough $(e, , \nu, \tau, u, c, t, d, s, b)$. In Eq 2.23, the down-type mass eigenstates are rotated into flavor eigenstates of the weak interaction $d_i^{'} = V_{ij} d_j$, with V_{ij} being the Cabibbo-Kobayashi-Maskawa matrix. This also enables a transition between generations for quarks interacting with the weak interaction, which is not the case for leptons. The relation between the eigenstates of the weak interaction and the mass eigenstates is given by the Cabibbo–Kobayashi–Maskawa (CKM) matrix [KM73, Cab63]. where $|V_{ij}|^2$ is the probability that a quark's flavor is changed from i to j undergoing an interaction with the W boson. An example is the decay of the lambda baryon, $\Lambda^0(uds) \rightarrow p(uud) + \pi^-(ud)$, where the strange quark transforms into an up quark under the transmission of a (virtual) W boson.

Symmetries of the weak interaction

Since the symmetry group of the weak interaction is $SU(2)$, the field must stay invariant when operated by a special unitary 2×2 matrix U for which:

$$UU^{\dagger} = U^{\dagger}U = 1, \qquad det(U) = 1 \tag{2.24}$$

Since any special unitary group $SU(N)$ has $N^2 - 1$ linearly independent generators, $SU(2)$ has three generators. In fact, the matrices U can be written as:

$$U = \exp^{i\omega_a(x)T^a} \tag{2.25}$$

where ω_a are real parameters and T^a are the generators of $SU(2)$, which can be written as one half times the corresponding Pauli matrix.

$$T^1 = \frac{1}{2}\sigma^1 = \begin{pmatrix} 0 & 1 \\ 1 & 0 \end{pmatrix} \qquad T^2 = \frac{1}{2}\sigma^2 = \begin{pmatrix} 0 & -i \\ i & 0 \end{pmatrix} \qquad T^3 = \frac{1}{2}\sigma^3 = \begin{pmatrix} 1 & 0 \\ 0 & -1 \end{pmatrix} \tag{2.26}$$

These are called the weak isospin operators. The weak isospin is the charge of the weak interaction. The operators satisfy the commutation relation:

$$[T^a, T^b] = \epsilon_{abc}T^c \tag{2.27}$$

We can test the Dirac Lagrangian's invariance under local SU (2) transformations. All indices of handedness and particle type are omitted for convenience, we will just consider a generic term.

$$\mathcal{L} = \bar{\psi}(i\gamma^{\mu}\partial_{\mu} - m)\psi \rightarrow \mathcal{L}^{'} = \bar{\psi}U^{\dagger}(x)(i\gamma^{\mu}\partial_{\mu} - m)U(x)\psi \tag{2.28}$$

$$= \bar{\psi}(i\gamma^{\mu}\partial_{\mu} - m)\psi + \bar{\psi}U^{\dagger}(x)i\gamma^{\mu} + \Big(\partial_{\mu}U(x)\Big)\psi \tag{2.29}$$

So, the Lagrangian is once again not invariant and we must introduce the covariant derivative. This time, it is of the form:

$$D_{\mu} = \partial_{\mu}\mathbb{1} + igW_{\mu} \tag{2.30}$$

Where g is a coupling constant and the gauge field W_{μ} transforms to preserve the in-variance as:

$$W_{\mu} \rightarrow W_{\mu}^{'} = U(x)W_{\mu}U^{\dagger}(x) + \frac{i}{g}\Big(\partial_{\mu}U(x)\Big)U^{\dagger}(x) \tag{2.31}$$

Similar procedure as QED and indeed, using this covariant derivative, the Lagrangian stays invariant: $\Big(D_{\mu}^{'} = \partial_{\mu}\mathbb{1} + igW_{\mu}^{'}\Big)$

$$
\begin{aligned}
\mathcal{L}^{'} &= \bar{\psi}U^{\dagger}(x)\Big(i\gamma^{\mu}D_{\mu}^{'} - m\Big)U(x)\psi \\
&= \bar{\psi}U^{\dagger}(x)\Big[i\gamma^{\mu}\Big(\partial_{\mu} + igW_{\mu}^{'}\Big) - m\Big]U(x)\psi \\
&= \bar{\psi}U^{\dagger}(x)\Big[i\gamma^{\mu}\Big(\partial_{\mu} + ig\Big\{U(x)W_{\mu}U^{\dagger}(x) + \frac{i}{g}\Big(\partial_{\mu}U(x)\Big)U^{\dagger}(x)\Big\}\Big) - m\Big]U(x)\psi \\
&= \bar{\psi}U^{\dagger}(x)\Big[i\gamma^{\mu}\partial_{\mu}U(x)\psi - g\gamma^{\mu}\Big\{U(x)W_{\mu}U^{\dagger}(x) + \frac{1}{g}\Big(\partial_{\mu}U(x)\Big)U^{\dagger}(x)\Big\}U(x)\psi - mU(x)\psi\Big] \\
&= \bar{\psi}U^{\dagger}(x)i\gamma^{\mu}\partial_{\mu}\Big(U(x)\psi\Big) - g\gamma^{\mu}\bar{\psi}U^{\dagger}(x)U(x)W_{\mu}U^{\dagger}(x)U(x)\psi - m\bar{\psi}U^{\dagger}(x)U(x)\psi \\
&- g\gamma^{\mu}\bar{\psi}U^{\dagger}(x)\cdot\frac{i}{g}\Big(\partial_{\mu}U(x)\Big)U^{\dagger}(x)U(x)\psi \\
&= \bar{\psi}\Big(U^{\dagger}(x)U(x)\Big)i\gamma^{\mu}\partial_{\mu}\psi + \bar{\psi}U^{\dagger}(x)i\gamma^{\mu}\Big(\partial_{\mu}U(x)\Big)\psi - \bar{\psi}\Big(U^{\dagger}(x)U(x)\Big)g\gamma^{\mu}W_{\mu}\Big(U^{\dagger}(x)U(x)\Big)\psi \\
&- \cancel{g}\bar{\psi}U^{\dagger}(x)\cdot\frac{i}{\cancel{g}}\Big(\partial_{\mu}U(x)\Big)\Big(U^{\dagger}(x)U(x)\Big)\psi - m\bar{\psi}\Big(U^{\dagger}(x)U(x)\Big)\psi \\
&= \bar{\psi}i\gamma^{\mu}\partial_{\mu}\psi - \bar{\psi}g\gamma^{\mu}W_{\mu}\psi - m\bar{\psi}\psi + \cancel{\bar{\psi}U^{\dagger}(x)i\gamma^{\mu}\Big(\partial_{\mu}U(x)\Big)\psi} - \cancel{\bar{\psi}U^{\dagger}(x)i\gamma^{\mu}\Big(\partial_{\mu}U(x)\Big)\psi} \\
&= \bar{\psi}\Big(i\gamma^{\mu}D_{\mu} - m\Big)\psi = \mathcal{L}
\end{aligned}
$$

Next, we want to write the covariant derivative 2.30 explicitly. We can use the generators T a from 2.27 as a basis for the components of W_{μ}:

$$
D_{\mu} = \partial_{\mu}\mathbb{1} + igW_{\mu}^{A}T_{A} = \partial_{\mu}\mathbb{1} + \frac{ig}{2}\begin{pmatrix} W_{\mu}^{3} & W_{\mu}^{1} - iW_{\mu}^{2} \\ W_{\mu}^{1} + iW_{\mu}^{2} & -W_{\mu}^{3} \end{pmatrix} \tag{2.32}
$$

The off-diagonal terms correspond to charged-current weak interaction and the physical particles $W\pm$. However, it turns out that for the neutral-current weak interaction, the physical force-carrier boson Z is a linear combination of the neutral field W_{μ}^{3} and another neutral field B_{μ}. This extra field comes from requiring the Lagrangian also to be $U(1)$ symmetric. Since $U(1)$ is the symmetry group of the electromagnetic force, this allows us to unify these two forces.

The electroweak unification

Now we want to include the $U(1)$ hypercharge interaction. For that, the Lagrangian for these fermions is required to be invariant under local transformations of $SU(2)_{L} \otimes U(1)_{Y}$, which transform the fields as:

$$
\psi(x)_{L} \rightarrow \psi^{'}(x)_{L} = e^{i\alpha(x)Y + i\omega^{a}(x)T_{a}}\chi(x) \tag{2.33}
$$

$$
\psi_{R}(x) \rightarrow \psi_{R}^{'}(x) = e^{i\beta(x)Y}\psi_{r}(x) \tag{2.34}
$$

The Abelian unitary group $U(1)_{Y}$ implies the conservation of the weak hypercharge, Y , which is given by the Gell-Mann-Nishijima relation [NN53]. Where T^{3} is the 3rd component of weak isospin. All particles in the SM have non-zero hypercharge excep for gluons and Here Q is the familiar electric charge.

$$
Y = 2\Big(Q - T^{3}\Big) \tag{2.35}
$$

On equation 2.34 $\omega(x)$ and $\alpha(x)$ are the phase transformation factors of the local gauge $SU(2)_{L}$ and $U(1)_{Y}$ σ symmetry groups, $a = 1, 2, 3$ and $T_{a} = \sigma_{a}/2$, with σ_{a} being the Pauli matrices, are the generators of $SU(2)$. To achieve local gauge invariance the covariant derivative is modified by adding an extra term so that

$$D\mu = \partial_\mu + igW_\mu^a T_a + ig^{'} Y B_\mu \tag{2.36}$$

The transformation of the field W_μ is already given in equation 2.31 and the field B_μ transforms as follows:

$$B_\mu \rightarrow B_\mu^{'} = B_\mu + \frac{iY}{g}\partial_\mu \alpha \tag{2.37}$$

Now we may finally write the entire $U(1) \otimes SU(2)$ covariant derivative 2.36 in explicit form.

$$D_\mu = \partial_\mu \mathbb{1} + igW_\mu^A T_A + ig^{'}\frac{Y}{2}B_\mu \mathbb{1} = \partial_\mu \mathbb{1} + \frac{ig}{2}\begin{pmatrix} W_\mu^3 + i\frac{g^{'}}{2}B_\mu & W_\mu^1 - iW_\mu^2 \\ W_\mu^1 + iW_\mu^2 & -W_\mu^3 + i\frac{g^{'}}{2}B_\mu \end{pmatrix} \tag{2.38}$$

We have now generated a matrix that describes the weak interaction: the diagonal elements describe the neutral currents, and the off-diagonal elements describe the charged currents. These so-called currents describe interactions where either positive or negative charge flows or a neutral Z boson interacts. We can now also see the reason why we use the notation $SU(2)_L$: only left-handed fields are affected by the $SU(2)$ part of the transformation, but both right and left handed fields are affected by the U(1) part. We have now combined the QED described by $U(1)_Y$ and weak interaction described by $SU(2)_L$ into combined symmetry $SU(2)_L \otimes U(1)_Y$. This is called the electroweak unification.

Furthermore, covariant derivatives are defined separately for left-handed and right-handed fermions:

$$D_\mu^L = \partial_\mu + igW_\mu^a T_a + i\frac{g^{'}}{2}Y B_\mu \tag{2.39}$$

$$D_\mu^R = \partial_\mu + i\frac{g^{'}}{2}Y B_\mu \tag{2.40}$$

The transformation of B_u is identical to the one obtained in QED for the photon, while the $SU(2)_L$ W_μ^i fields transform in a way analogous to the gluon fields of QCD. Note that the ψ couplings to B_μ are completely free as in QED, i.e., the hypercharges Y can be arbitrary parameters. Since the $SU(2)_L$ commutation relation is non-linear, this freedom does not exist for the W_μ^i : there is only a unique $SU(2)_L$ coupling g. The Lagrangian

$$\mathcal{L} = i\bar{\psi}\gamma^\mu \mathcal{D}_\mu \psi$$

is invariant under local G transformations. In order to build the gauge-invariant kinetic term for the gauge fields, we introduce the extension corresponding to the field strengths: Where four gauge fields are introduced: W_μ^a , with $a = 1, 2, 3$, are the fields associated to the $SU(2)_L$ symmetry, B_μ is the field associated to the $U(1)_Y$ symmetry and $g, g^{'}$ are the respective coupling constants. The field strength tensors are:

$$W_{\mu\nu}^a = \partial_\mu W_\nu^a - \partial_\nu W_\mu a + g\epsilon^{abc} W_{b\mu} W_{c\nu} \tag{2.41}$$

$$W_{\mu\nu} = \partial_\mu B_\nu - \partial_\nu B_\mu. \tag{2.42}$$

The resulting Lagrangian density of the electroweak sector before the symmetry breaking is

$$\mathcal{L}_{\mathrm{EF}} = \bar{\psi}_L \gamma^\mu \Big(i\partial_\mu - \frac{g}{2} W_\mu^a T_a + \frac{g^{'}}{2} B_\mu \Big) \psi_L + \bar{\psi}_R \gamma^\mu \Big(i\partial_\mu + g^{'} B_\mu \Big) \psi_R - \frac{1}{4} W_{\mu\nu}^a W_a^{\mu\nu} - B_{\mu\nu} B^{\mu\nu} \tag{2.43}$$

The weak interaction is mediated by three gauge bosons and couples to the weak isospin, T_W. The three gauge bosons are: two charged $W\pm$ bosons and a neutral Z^0 boson. The Standard Model The exchange of a $W\pm$ boson modifies both the flavor and the electric charge of the fermions and is called the charged current. In contrast, the Z^0 boson exchange leaves the flavor intact and is called the neutral current.

However, it must be noted that the observed particles do not directly correspond to the fields W_μa and B_μ , but their linear combinations. The observed $W\pm$ bosons are linear combinations of W^1 and W^2. The mixing between the W^3 and B fields gives the Z boson as well as the photon. Finally the physical gauge bosons $\gamma, Z, W\pm$ are given by((the A_μ field gives the photon)):

$$W_\mu^\pm = \frac{1}{\sqrt{2}} \Big(W_\mu^1 \mp W_\mu^1 \Big) \tag{2.44}$$

$$Z_\mu = W_\mu^3 \cos_\theta - B_\mu \sin\theta_W \tag{2.45}$$

$$A_\mu = W_\mu^3 \sin_\theta + B_\mu \cos\theta_W \tag{2.46}$$

where θ_W is the Weinberg angle defined in terms of the coupling constants g and g_0 through:

$$\sin\theta_W = \frac{g^{'}}{\sqrt{g^2 + g^{'2}}} \qquad\qquad \cos\theta_W = \frac{g}{\sqrt{g^2 + g^{'2}}} \tag{2.47}$$

One peculiar property of the $W\pm$ bosons is the parity violation; they couple only to left-handed particles and right-handed anti-particles. The laws of nature were long thought to be invariant under the parity transformation, which is described by simultaneously flipping the sign of all spatial coordinates. However, it was first proposed in 1956 by Chen-Ning Yang and Tsung-Dao Lee that the weak interaction might be parity violating, specifically in α decays [LY56]. One year later, this was experimentally confirmed [WAH$^+$57], earning Yang and Lee the 1957 Nobel Prize in Physics. Because of these properties, the $SU(2)$ symmetry group is denoted as $SU(2)_L$, and the hypercharge Y is defined. The connection between the hypercharge, the electric charge Q, and the third component of the weak isospin I3 is given by the Gell-Mann–Nishijima formula [GM56, Nis55]

However, this Lagrangian 2.43 requires both the fermions and the gauge bosons to be massless fields and massless gauge fields, as any explicit mass term would violate the gauge invariance itself. This contradicts all observations of various HEP experiments that measured the mass of the Z^0 and $W\pm$ bosons to be massive to high precision. Notably, Carlo Rubbia and Simon van der Meer received the Nobel Prize in physics in 1984 for their decisive contributions to the discovery of Z and W bosons by the UA1 and UA2 Collaborations [AAA$^+$83, BBB$^+$83]. Moreover, the ATLAS Collaboration recently presented a precise measurement of the $W\pm$ bosons masses [A$^+$18], but adding mass terms would violate the gauge invariance. As described in the following section, the solution to this problem is given by introducing an additional field, the Higgs field, with the mechanism of electroweak symmetry breaking, which gives rise to massive gauge bosons. Mass terms for the fermions are introduced as well by introducing a gauge invariant interaction between the Higgs field and the fermions, i.e. the Yukawa interaction.

2.5 Quantum Chromo Dynamics (QCD)

Similarly, as the QED describes the interaction between charged fermions and the quanta of the electromagnetic field, the photon, Quantum Chromodynamics (QCD) is the theory of the strong

interaction among quarks and gluons, collectively called partons, collectively called partons. The interaction particle gluon, a spin 1 massless boson, is the generator of this interaction. Gluons bind quarks together to form hadrons. These are made of Quarks, which make up bound states like mesons ($q\bar{q}$) and baryons (qqq). Quarks carry electric charge, so interact through electromagnetic interaction while also carrying an additional quantum number called color charge. QCD is vital in hadron collisions because the constituents of protons are partons.

In 1964-65, the color charge was introduced as an $SU(3)$ gauge degree of freedom [Gre64, HN65] to explain the existence of the spin $S = 3/2$ Baryon, Δ^{++} , which is composed of three up-quarks with parallel spins and, therefore, would otherwise violate the Pauli exclusion principle. This also helps resolve a dilemma of the inconsistency of the Pauli exclusion principle to three identical quarks in the same state in a baryon, such as $\Omega - baryon$, consisting of three identical s quarks [ESW03]. The exclusion principle states that identical quarks are not allowed to exist in the same quantum state. Each of the identical quarks is given one of three possible color charges (red, green, or blue). The dilemma was solved by defining the three quarks as no longer identical. A quark can carry one of three colors and its antiquark carries the corresponding anticolor [Per00]

Like weak interaction, the strong interaction is described with a non-abelian gauge theory, and therefore, the operators describing the fields don't commute. Although the strong interaction shares the same kind of properties as the weak interaction through the behavior of non-abelian theory, there is a difference between the two; the force of strong interaction is large at large distances.

Since QCD is a non-Abelian gauge theory based on the $SU(3)$ symmetry group, where the quark fields are represented as a color triplet, ψ:

$$\psi = \begin{pmatrix} \psi_r \\ \psi_g \\ \psi_b \end{pmatrix} \tag{2.48}$$

With the r, b and g indices corresponding to the quark color charges: red, blue and green respectively.

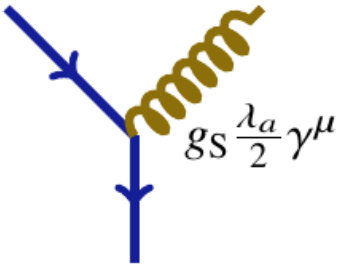

Figure 2.2: 1 vertex interaction

Figure 2.3: 3 vertex interaction

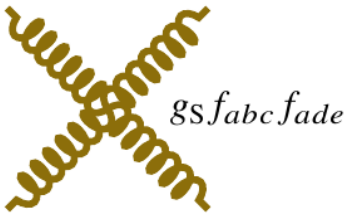

Figure 2.4: 4 vertex interaction

Figure 2.5: The fundamental couplings of the strong interaction: (2.2) gluon radiation, (2.3) gluon splitting, and (2.4) gluon self-interaction.

As stated, QCD is a non-abelian gauge theory, and non-abelian theories are asymptotically free. In the case of SU(3), the running of the coupling constant α also behaves differently at small distances compared to the weak interaction. At large distances (small energies), the constant is large, which means that quarks are bound to be in hadrons. However as the energy grows, α gets weaker meaning that the particles are almost non-interacting. This is called the asymptotic freedom.

Gluons

QCD has the symmetry group $SU(3)$ so it has 8 generators, and there are 8 gluons carrying the force. The generators are called the Gell-Mann matrices:

$$\lambda_1 = \begin{pmatrix} 0 & 1 & 0 \\ 1 & 0 & 0 \\ 0 & 0 & 0 \end{pmatrix} \qquad \lambda_2 = \begin{pmatrix} 0 & -i & 0 \\ i & 0 & 0 \\ 0 & 0 & 0 \end{pmatrix} \qquad \lambda_3 = \begin{pmatrix} 1 & 0 & 0 \\ 0 & -1 & 0 \\ 0 & 0 & 0 \end{pmatrix} \tag{2.49}$$

$$\lambda_4 = \begin{pmatrix} 0 & 0 & 1 \\ 0 & 0 & 0 \\ 1 & 0 & 0 \end{pmatrix} \qquad \lambda_5 = \begin{pmatrix} 0 & 0 & -i \\ 0 & 0 & 0 \\ -i & 0 & 0 \end{pmatrix} \qquad \lambda_6 = \begin{pmatrix} 0 & 0 & 0 \\ 0 & 0 & 1 \\ 0 & 1 & 0 \end{pmatrix} \tag{2.50}$$

$$\lambda_7 = \begin{pmatrix} 0 & 0 & 0 \\ 0 & 0 & -i \\ 0 & i & 0 \end{pmatrix} \qquad \lambda_8 = \frac{1}{\sqrt{3}} \begin{pmatrix} 1 & 0 & 0 \\ 0 & 1 & 0 \\ 0 & 0 & 2 \end{pmatrix} \tag{2.51}$$

The gluons can be written for example as the following linear combinations of color-anticolor pairs:

$$\frac{r\bar{b} + b\bar{r}}{\sqrt{2}}, frac r\bar{b} + b\bar{r}\sqrt{2}, \qquad \frac{-i(r\bar{b} - b\bar{r})}{\sqrt{2}}, \frac{r\bar{g} + g\bar{r}}{\sqrt{2}}, \qquad \frac{-i(r\bar{b} - b\bar{r})}{\sqrt{2}} \tag{2.52}$$

$$\frac{b\bar{g} + g\bar{b}}{\sqrt{2}}, \frac{-i(b\bar{g} - g\bar{b})}{\sqrt{2})}, \qquad \frac{r\bar{r} - b\bar{b}}{\sqrt{2}}, \frac{(r\bar{r} + b\bar{b} - 2g\bar{g})}{\sqrt{6}} \tag{2.53}$$

All of these are linearly independent and also independent of the forbidden singlet state $1/3(r\bar{r} + g\bar{g} + b\bar{b})$. The problem with this state is that it would be colorless, making this gluon not experience the strong force itself. This would make the lifetime of the gluon extremely long, which would in turn significantly increase the range of the strong force and completely change QCD physics.

Again we want to perform the gauge transformation, and in the SU(3) case the. Transformation is:

$$\partial_\mu \to \mathcal{D}_\mu = \partial_\mu + ig_s G_\mu \tag{2.54}$$

And finally, the field transforms as well:

$$G_\mu = U G_\mu U^\dagger + \frac{i}{g_s} G_\mu \tag{2.55}$$

But similarly as in the previous case in equation 2.29. The Lagrangian it is not invariant. And the U now being the transformation matrix of $SU(3)$. To write the Lagrangian, we will need the propagation term for the gluons. For this we will define

$$G_\mu \to G_\mu^{'} = \partial_\mu G_\nu - \partial_\nu G_\mu + igs f_{abc} G_\mu^b G_\nu^c \tag{2.56}$$

Here f_{abc} are the structure constants of $SU(3)$ defined by the commutation relation:

$$[\lambda_a, \lambda_b] = 2i \sum_{c=1}^{8} f_{abc} \lambda^c$$

Written explicitly, this amounts to:

$$
\begin{aligned}
f_{123} &= 1 \\
f_{458} = f_{678} &= \frac{\sqrt{3}}{2} \\
f_{147} = f_{246} = f_{257} = f_{345} = f_{516} = f_{637} &= \frac{1}{2} \\
f_{ijk} = f_{jki} &= -f_{jik} \\
f_{ijk} &= 0 \qquad \textbf{for other permutations}
\end{aligned}
$$

Now we can write the dynamical term for the gluon Lagrangian analogously to the photon propagator, the only difference being the extra term added to the gluon propagator 2.54 and using the new field in equation 2.56 for gauge invariance.

$$
\begin{aligned}
\mathcal{L} &= \frac{-1}{4}\sum_{a=1}^{8} G'^{a}_{\mu\nu} G'^{\mu\nu}_{a} \\
&= \left(\partial_\mu G^a_\nu - \partial_\nu G^a_\mu\right)\left(\partial_\mu G^\nu_a - \partial_\nu G^a_\mu\right) - \frac{1}{4} f^{abc} f_{ade} G^\mu_b G^\nu_c G^d_\mu G^e_\nu \\
&+ \frac{1}{2} f_{abc}\left(\partial_\mu G^\nu_a - \partial_\nu G^a_\mu\right) G^{\mu b} G^{\nu c}
\end{aligned}
$$

The QCD Lagrangian

After introducing color charge in the strong interactions, we discuss the properties of the strong force inside the proton and the structure of partons inside the proton. The colors are conventionally taken as red, green and blue The Lagrangian for a free quark $q(x)$ is:

$$
\begin{aligned}
\mathcal{L}_{QCD} &= \sum_f \bar{\psi}(i\gamma^\mu \partial_\mu - m)\psi_f \qquad \text{kinematic term} && (2.57)\\
&- \sum_f g\bar{\psi}_f \gamma^\mu G^\mu \psi_f \qquad \text{gluon- fermion interaction} && (2.58)\\
&- \frac{1}{4}(\partial_\mu G^a_\nu - \partial_\nu G^a_\mu)(\partial^\mu G^{a,\nu} - \partial^\nu G^{a,\mu}) \qquad \text{kinematic term} && (2.59)\\
&+ \frac{1}{2} g f_{abc}(\partial_\mu G^a_\nu - \partial_\nu G^a_\mu) G^{b,\mu} G^{c,\nu} \qquad \text{3-point self interaction} && (2.60)\\
&- \frac{1}{4} g^2 f_{abe} f_{cde} G^a_\mu G^b_\nu G^{c,\mu} G^{d,\nu} \qquad \text{4-point self interaction} && (2.61)
\end{aligned}
$$

One problem with carrying out QCD calculations is that the coupling is too strong for perturbation theory to be applicable. However, in the high energy regime, the coupling strength of the strong interaction weakens, making perturbation theoretical calculations possible. This is known as asymptotic freedom.

2.5.1 Spontaneous symmetry breaking and The Brout-Englert-Higgs mechanism

As stated previously for the Electro-Weak lagnrangian 2.43, the theory requires both the fermions and the gauge bosons to be massless, as any explicit mass term would violate the gauge invariance. Because of the gauge principle, we cannot just add additional mass terms to the system. We also cannot put away the gauge invariance as the whole theory becomes non-renormalizable.

The mechanism needed to generate masses for Z and W bosons is called spontaneous symmetry breaking (SSB), where the $SU(2) \otimes U(1)$ symmetry gets broken. In SSB, the Lagrangian is symmetric, or invariant, under a transformation, but the ground state, describing the minimum

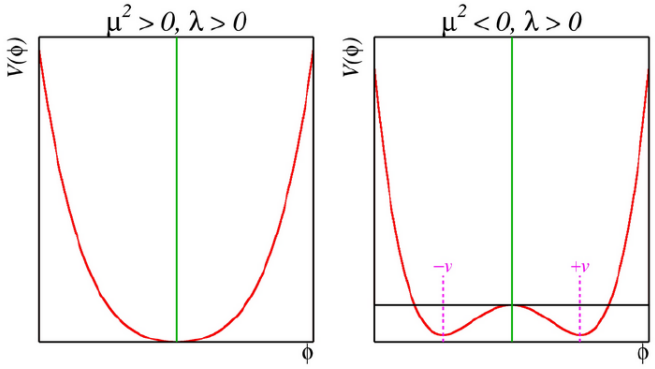

Figure 2.6: Potential of the scalar field for different parameters

of the system, is not. This model introduces a new scalar boson with spontaneous electroweak symmetry breaking mechanism as it does not happen for external reasons.

This model introduces a new scalar boson with a mechanism of spontaneous electroweak symmetry breaking: the Higgs boson. In this model, a complex scalar field in the form of a doublet of $SU(2)$ with $Y = 1$ is introduced. Now we want to break the electroweak symmetry. For this we need to introduce a new scalar SU(2) doublet:

$$\Phi = \begin{pmatrix} \phi^+ \\ \phi^0 \end{pmatrix} = \frac{1}{\sqrt{2}} \begin{pmatrix} \phi_1 + i\phi_2 \\ \phi_3 + i\phi_4 \end{pmatrix} \tag{2.62}$$

The BEH lagrangian can consequently be written as:

$$\mathcal{L}_{BEH} = (D_\mu \Phi)^\dagger (D_\mu \Phi) - \mu^2 \Phi^\dagger \Phi - \lambda (\Phi^\dagger \Phi)^2 \tag{2.63}$$

where $D_\mu$is the $SU(2)_L \otimes U(1)_Y$ covariant derivative from 2.36. We can separate the potential out of the Lagrangian:

$$V(\Phi) = \mu^2 \Phi^\dagger \Phi + \lambda (\Phi^\dagger \Phi)^2 \tag{2.64}$$

The extrema of the potential can be found by calculating the zeros of the derivative.

$$\frac{\partial V}{\partial \Phi^\dagger} = (\mu^2 + 2\lambda \Phi^\dagger \Phi)\Phi = 0 \tag{2.65}$$

Next, we will allow the mass (or the minimum) to be negative $^\mu < 0$, which gives us the so-called Mexican hat potential like on the right-hand side in Figure 2.6 as a maximum appears in $\Phi = 0$. The minimum is now

Symmetries of the vacuum state

We are free to choose the minimum. From Eq. (2.65), we may write the vacuum state (minimum) now as,

$$\Phi^\dagger \Phi = \begin{pmatrix} \phi^{+\dagger} & \phi^{0\dagger} \end{pmatrix} \begin{pmatrix} \phi^+ \\ \phi^0 \end{pmatrix} \tag{2.66}$$

from where

$$< \Phi^\dagger \Phi >= \phi^{+\dagger}\phi^+ + \phi^{-\dagger}\phi^- = -\frac{\mu^2}{2\lambda} \tag{2.67}$$

It follows that

$$\phi^- = 0 \quad \text{and} \quad \phi^+ = \sqrt{\frac{-\mu^2}{2\lambda}} = \frac{v}{\sqrt{2}} \tag{2.68}$$

This corresponds to choosing the so-called unitary gauge. We can explicitly check how this ground state responds to the symmetries of $SU(2)_L \otimes U(1)_Y$. If it was invariant, we would get:

$$e^{ia\Lambda}\Phi_{ground} = \Phi_{ground} \Rightarrow \Lambda\Phi_{ground} = 0$$

where Λ is one of the generators of$SU(2)_L \otimes U(1)_Y$, namely $\Lambda = T^{1,2,3}$ defined in 2.26. or $\Lambda = Y/2 = 1$. However, we have:

$$T^1\Phi_{ground} = \frac{1}{2}\begin{pmatrix}0 & +1\\ 1 & 0\end{pmatrix}\begin{pmatrix}0\\ v/\sqrt{2}\end{pmatrix} = \frac{+1}{2}\begin{pmatrix}v/\sqrt{2}\\ 0\end{pmatrix} \neq 0 \tag{2.69a}$$

$$T^2\Phi_{ground} = \frac{1}{2}\begin{pmatrix}0 & -i\\ i & 0\end{pmatrix}\begin{pmatrix}0\\ v/\sqrt{2}\end{pmatrix} = \frac{-i}{2}\begin{pmatrix}v/\sqrt{2}\\ 0\end{pmatrix} \neq 0 \tag{2.69b}$$

$$T^3\Phi_{ground} = \frac{1}{2}\begin{pmatrix}1 & 0\\ 0 & -1\end{pmatrix}\begin{pmatrix}0\\ v/\sqrt{2}\end{pmatrix} = \frac{-1}{2}\begin{pmatrix}0\\ v/\sqrt{2}\end{pmatrix} \neq 0 \tag{2.69c}$$

$$Y\Phi_{ground} = \frac{1}{2}\begin{pmatrix}1 & 0\\ 0 & +1\end{pmatrix}\begin{pmatrix}0\\ v/\sqrt{2}\end{pmatrix} = \frac{+1}{2}\begin{pmatrix}0\\ v/\sqrt{2}\end{pmatrix} \neq 0 \tag{2.69d}$$

The ground state does not respect any of these symmetries. But we can find one symmetry that is still there. We know from 2.35 that the electric charge Q can be written as $Q = T^3 + Y/2$. We can operate Φ_{ground} by Q:

$$Q\Phi_{ground} = (T^3 + Y/2)\Phi_{ground} = \frac{1}{2}\Big[\begin{pmatrix}1 & 0\\ 0 & -1\end{pmatrix} + \begin{pmatrix}1 & 0\\ 0 & 1\end{pmatrix}\Big]\begin{pmatrix}0\\ v/\sqrt{2}\end{pmatrix} = 0 \tag{2.70}$$

The electroweak symmetry group is thus broken with the pattern: $SU(2)_L \otimes U(1)_Y \to U(1)_{em}$ is, therefore, still a symmetry of the Lagrangian around this minimum. Hence we have broken three generators out of the original four. According to Goldstone's theorem [GSW62], this corresponds to three massless particles

Gauge boson masses and the Higgs boson

If we now wish to take a local gauge transformation, we must expand the state around the minimum. The field $\Phi(x)$ can be written in terms of S $U(2)$ transformations adding four scalar fields$\theta_1, \theta_2, \theta_3$, h, which parameterise fluctuations around the minimum:

$$\Phi(x) = \exp^{iT^a\theta_a/v}\begin{pmatrix}0\\ \frac{v+h}{\sqrt{2}}\end{pmatrix} \simeq \frac{1}{2}\begin{pmatrix}\theta_2 + i\theta_1\\ v + h - i\theta_3\end{pmatrix} \tag{2.71}$$

The fields $\theta_1, \theta_2, \theta_3$ are the massless Goldstone bosons generated by the electroweak symmetry breaking and they can be removed from the Lagrangian by doing a S U(2) gauge transformation so that the resulting field, in the so-called unitary gauge, can be written as:

$$\Phi(x) = \begin{pmatrix}0\\ \frac{v+h}{\sqrt{2}}\end{pmatrix} \tag{2.72}$$

Where $h(x)$is the Higgs scalar field. We will drop the explicit dependence of the field h on the space-time coordinate and use the gauge principle as before. By using the covariant derivative,

we wish to examine the first term of the Lagrangian: $|D_\mu \Phi|^2$, as it holds all the interesting kinematic contributions of the system. By inserting the covariant derivative into the term 2.36.

$$\begin{aligned}\mathcal{D}\Phi &= \frac{1}{\sqrt{2}} \begin{pmatrix} \partial_\mu + i\frac{g}{2}W_\mu^3 + i\frac{g^{'}}{2}B_\mu & \frac{ig}{2}\big(W_\mu^1 - iW_\mu^2\big) \\ \frac{ig}{2}\big(W_\mu^1 + iW_\mu^2\big) & \partial_\mu - i\frac{g}{2}W_\mu^3 + i\frac{g^{'}}{2}B_\mu \end{pmatrix} \begin{pmatrix} 0 \\ v+h \end{pmatrix} \\ &= \frac{1}{\sqrt{2}} \begin{pmatrix} \frac{ig}{2}\big(W_\mu^1 - iW_\mu^2\big)\big(v+h\big) \\ \partial_\mu h - i\big(v+h\big)\big(\frac{g}{2}W_\mu^3 - \frac{g^{'}}{2}B_\mu\big) \end{pmatrix}\end{aligned}$$

And the congujate is:

$$\mathcal{D}\Phi^\dagger = \frac{1}{\sqrt{2}} \Big(\tfrac{-ig}{2}\big(W_\mu^1 + iW_\mu^2\big)\big(v+h\big), \partial_\mu h + i\big(v+h\big)\big(\tfrac{g}{2}W_\mu^3 - \tfrac{g^{'}}{2}B_\mu\big)\Big)$$

Using the fields for the physical particles for the photon(A_μ or γ^μ), $W^\pm$ and Z^0 bosons 2.46 The kinetic term can be then written as:

$$|\mathcal{D}\Phi|^2 = \frac{1}{2}(v+h)^2 \begin{pmatrix} 0 & 1 \end{pmatrix} \begin{pmatrix} \partial_\mu + i\frac{g}{2}W_\mu^3 + i\frac{g^{'}}{2}B_\mu & \frac{ig}{2}\big(W_\mu^1 - iW_\mu^2\big) \\ \frac{ig}{2}\big(W_\mu^1 + iW_\mu^2\big) & \partial_\mu - i\frac{g}{2}W_\mu^3 + i\frac{g^{'}}{2}B_\mu \end{pmatrix}^2 \begin{pmatrix} 0 \\ 1 \end{pmatrix} \tag{2.73}$$

This equals to

$$|\mathcal{D}\Phi|^2 = \frac{1}{2}\partial_\mu h \partial^\mu h + \frac{1}{2}(v+h)^2\big(\frac{g^2}{4}W_\mu^- W^{+\mu} + \frac{1}{4}(g^2 + g^{'2})Z_\mu Z^\mu\big) \tag{2.74}$$

Mass terms have appeared in the Lagrangian. The masses for W± and Z can be read from the Lagrangian and are:

$$m_W = \frac{vg}{2} \qquad\qquad m_Z = \frac{v\sqrt{g^2 + g^{'2}}}{2} \tag{2.75}$$

It is also worth noting that the photon is still massless. Also, the Weinberg angle introduced previously can be written as the ratio between the weak gauge boson masses:

$$\cos\theta_W = \frac{m_W}{m_Z} \tag{2.76}$$

This angle is a phenomenologically interesting factor. It states that by measuring the Weinberg angle and the masses, the relation has a remarkable consistency check of the SM. Indeed, the factor

$$\rho = \frac{m_W}{m_Z \cos\theta_W} \tag{2.77}$$

has been experimentally measured to be close to one [BCLT10]

Because the photon field does not appear in this mass term means that the photons stay massless after the SSB as they should. The potential part 2.63 of the scalar Lagrangian 2.58 is easy to calculate using the fact that $\Phi^\dagger\Phi = 1/22(v+h)^2$ and that $\lambda = -(\mu v)^2$ (as defined in 2.68)

$$V(\Phi) = \mu^2\Phi^\dagger\Phi + \lambda(\Phi^\dagger\Phi)^2 \tag{2.78}$$
$$= \frac{1}{2}(v+h)^2(\mu^2 + \lambda\frac{1}{2}(v+h)^2) \tag{2.79}$$
$$= \frac{1}{2}(v+h)^2(\mu^2 - (\frac{\mu}{v})^2\frac{1}{2}(v+h)2) \tag{2.80}$$
$$= \frac{\mu^2 v^2}{2} - \mu^2 h^2 - \frac{\mu^2}{v}h^2 - \frac{\mu^4}{v^4}h^4 \tag{2.81}$$

The first term does not depend on any fields, and therefore, it does not affect the physics of the system and can be dropped. The entire Lagrangian is:

$$\mathcal{L}_{BHE} = \frac{1}{2}\partial_\mu h\partial^\mu h - \frac{1}{2}(2\lambda)h^2 \tag{2.82}$$
$$+ \Big[(\frac{gv}{2})^2 W^{\mu+}W^-_\mu + \frac{1}{2}\frac{v^2(g^2+g'^2)}{4}Z^\mu Z_\mu\Big]\Big(1+\frac{h}{v}\Big)^2 \tag{2.83}$$
$$- \lambda v h^3 - \frac{\lambda}{4}h^4 + \frac{\lambda}{4}v^4 \tag{2.84}$$

The degrees of freedom carried by the massless Goldstone bosons are transferred to the massive $W^\pm$ and Z bosons. It can be observed that the Goldstone bosons, removed with the unitary transformation, are absorbed as additional degrees of freedom of the $W^\pm$ and Z bosons, corresponding to their longitudinal polarizations: the mechanism gives mass to the weak bosons. Here are also the terms hWW and a hZZ interactions from the $2h/v$ term and a $hhWW$ and a $hhZZ$ interaction from the h^2/v^2 term. In addition, this terms have triple and quartic coupling terms of the field h with the heavy 2 gauge bosons $W^\pm$ and Z, which are proportional to the mass squared of the gauge boson, $\lambda_{VVh} = 2m_v^2/v^2$ and $\lambda_{VVhh} = m_v^2/v^2$respectively.

This boson masses terms can now be identified by looking at the terms in the equation 2.75. Respectively. and the Higgs boson has mass m_h, given by

$$m_h = \sqrt{-2\mu^2} = v\sqrt{2\lambda} \tag{2.85}$$

The remaining terms in Equation 2.84 represent the interactions of the weak bosons with the Higgs field and the trilinear and quadlinear Higgs self-interactions, h^3 and h^4.

The third line in 2.84 is that cubic and quartic self-interactions of the Higgs boson are predicted. The BEH potential can be rewritten in terms of a trilinear and a quadrilinear coupling as:

$$V(H) = \frac{1}{2}m_v^2 h^2 + \lambda_{hhh}vh^3 + \lambda_{hhhh}h^4 - v^4 \tag{2.86}$$

With the self-coupling constants defined as:

$$\lambda_{hhh} = \lambda_{hhhh} = \lambda = \frac{m_H^2}{2v^2} \tag{2.87}$$

An important remark is that both Higgs boson self-couplings and the scale of the weak boson masses are directly related to the parameters of the scalar potential and are entirely determined from the Higgs boson mass and the VEV (vacuum expectation value) v. Their measurement, thus represents a test of the validity and coherence of the SM. It can be evaluated using the empirical value of the Fermi constant G_F from the muon decay or the expectation value of the Higgs field, given by $v = (\sqrt{2}G_F)^{-1/2} \sim 246$ GeV.

On a broader perspective, the Higgs boson self-couplings have no equal in the SM: In contrast to the weak boson self-interactions, that have a gauge nature, the Higgs boson self-interactions are purely related to the scalar sector of the theory, and they are responsible for the mass of the Higgs boson itself.

Their experimental determination is thus crucial to reconstruct the Higgs boson potential and exploring the nature of the EWSB (Electro-Weak symmetry breaking). Finally, there is a constant term in the Lagrangian density of BEH . While this is irrelevant in the SM, it contributes to the vacuum energy, which is related to the cosmological constant that determines the curvature of the Universe. The value of this constant predicted in the SM is not compatible with astronomical observations. This is a puzzle that requires either a proper quantum theory of gravity with additional interactions or a mechanism to reduce the Higgs field vacuum energy density.

Nevertheless, the Higgs boson mass m_h and the masses of the vector bosons cannot be predicted as λ and g, $g^{'}$ are free parameters of the theory. Precise measurements of the boson masses and their couplings to the Higgs boson are essential to test the validity of the Brout-Englert-Higgs mechanism, the electroweak theory, and the SM theory itself. This thesis works aims to improve the measurement with and accurate calculations of the fakes factors and visualization of the modeling in the search for di-Higgs production in order to test the triple Higgs self-coupling λ_{hhh} and therefore probe the structure of the Higgs potential.

2.5.2 Yukawa coupling and fermion masses

So far, the fermions are all massless. The first idea to fix this would be to add a naive mass terms of the form:

$$m(\psi_L^\dagger \psi_R + \psi_R^\dagger \psi_L)$$

However, this is not gauge invariant. The left-handed object transforms under $SU(2)$, but the right-handed one does not. Therefore we introduce Yukawa couplings.

$$\mathcal{L}_{Yuk} = -g_e \Big[\begin{pmatrix} \bar{\nu}_{eL} & \bar{e}_L \end{pmatrix} \begin{pmatrix} 0 \\ \frac{1}{2}(v+h)) \end{pmatrix} e_r + \bar{e}_R \begin{pmatrix} 0 & \frac{1}{2}(v+h). \end{pmatrix} \begin{pmatrix} \nu_{eL} \\ e_L \end{pmatrix} \Big] \tag{2.88}$$

$$= -\frac{1}{\sqrt{2}} g_e (v+h)[\bar{e}_L e_R + \bar{e}_R e_L] = -\frac{1}{\sqrt{2}} g_e (v+h)\bar{e}e \tag{2.89}$$

This is indeed a mass term, letting us identify that

$$m_e = \frac{g_e(v+h)}{\sqrt{2}} \tag{2.90}$$

We see that the electron mass is proportional to the Yukawa coupling constant and the Higgs vacuum expectation value, as are all fermion masses in general. The Yukawa coupling, however, is different for each particle. Since there currently are no right-handed neutrinos in the Standard Model, this mechanism cannot be used to create masses for the neutrinos, even though experimentally, we know from neutrino oscillations that the masses must be nonzero.

2.6 The Higgs boson and Higgs pair production phenomenology and experimental status

Experimental confirmation of the BEH mechanism came in July 2012 with the discovery of a new scalar boson of a mass of approximately 125 GeV announced by the ATLAS and CMS Collaborations [C$^+$12, Col12].

The discovery was performed in the data collected at $\sqrt{s} = 8$ TeV (Run I) and lead by the high-resolution $H \to ZZ^* \to l^+l^-l^{'+}l^{'-}(l, l^{'} = e, \mu)$ and $H \to \gamma\gamma$ decay channels. The existence of this scalar particle is now firmly established and further confirmed with the data collected at $\sqrt{s} = 13TeV$(Run II), as shown in Figure 2.7.

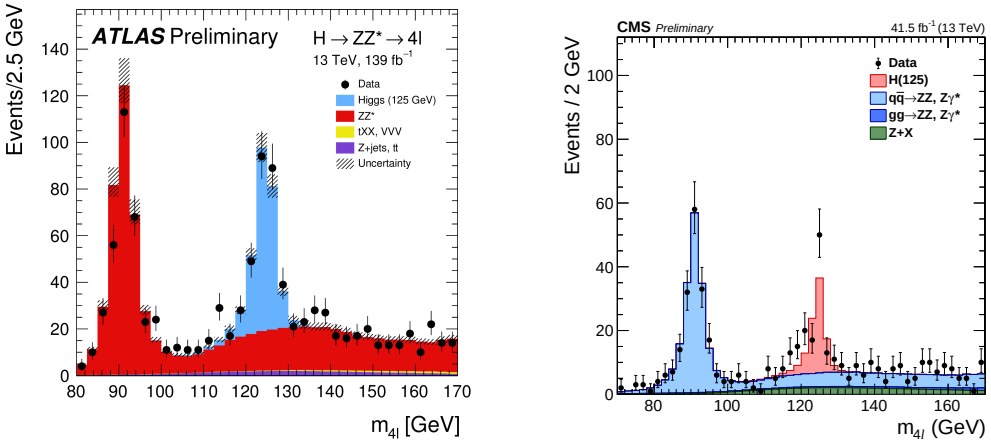

(a) The ATLAS experiment observation was given by the combination of the decay channels $H \to ZZ^* \to 4l, H \to \gamma\gamma$ and $H \to WW^* \to lvlv$ with a significance of 5.9σ

(b) The CMS experiment observation by the combination of the decay channels $H \to ZZ^* \to 4l, H \to \gamma\gamma$ and $H \to WW^* \to lvlv, H \to b\bar{b}$ and $H \to \tau^+\tau^-$ with a significance of 5.0σ

Figure 2.7: Distribution of the reconstructed four-lepton invariant mass m4l in the low ass range, with full Run II data, in CMS [CMS18] (on the right) and ATLAS [ATL19] (on the left) experiments. Points with error bars represent the data, and stacked histograms represent expected distributions of the signal and background processes.

The Higgs boson production and decay modes are described in the following sections.

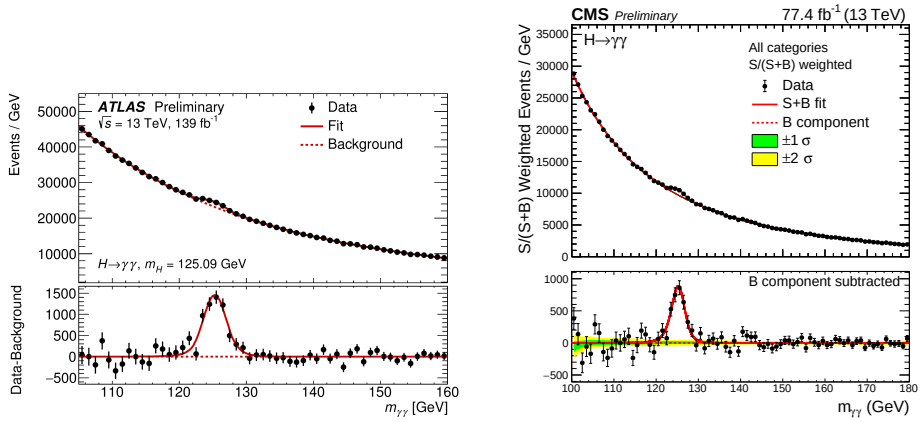

Figure 2.8: Distribution of the reconstructed di-photon invariant mass $m_{\gamma\gamma}$ in the low-mass range, with 2016 and 2017 data collected by CMS [CMS19] (on the right) and the full Run II data collected by

With the observation of the Higgs boson and the measurement of its mass, the last important

parameter of the SM has been determined. However, the observation of this new particle only represents the first step in the exploration of the EWSB. The efforts of the experimental community are thus focusing on the characterization of this boson. The measurements of its couplings via exclusive production modes and decay channels, of its spin-parity, and of its differential production cross-section, the properties of the new particle need to be thoroughly investigated to verify that they correspond precisely to the SM predictions. To date, its mass has been measured [Col15a] from the combination of the ATLAS and CMS results in the four leptons final state to be:

$$m_H = 125.09 \pm 0.24(0.21_{stat} \pm 0.11_{syst}) \quad GeV \tag{2.91}$$

and studies on the spin and parity quantum numbers show that the particle is compatible with the SM neutral spin-0 boson with $J^P = 0^+$ [Col13a]. It was also proven that it couples to the gauge bosons and to the fermions of the third generation [Col15b, Col19], with couplings being consistent with the SM predictions.

However, the observed couplings need to be measured with higher precision in order to be compared with the expectations and check that there are indeed no deviations. Moreover, only some couplings predicted by the SM have been observed so far: couplings of the Higgs boson to fermions of the first and second generations and the Higgs self-coupling are still unobserved. Testing the Higgs self-coupling by studying the di-Higgs production process is the main goal of the $b\bar{b}\tau\tau$ analysis.

2.6.1 Higgs production and decay

Several mechanisms contribute to the production of a Higgs boson at a pp collider. The dominant one, with a cross-section of about 49 pb, is the gluon fusion (ggF) production, that proceeds through a heavy quark loop. The second most frequent mechanism, about 10 times rarer than ggF is vector boson fusion VBF, where the Higgs bosonis produced in association with a jet pair of large invariant mass. The third main mechanism is the production in association with a single vector boson ($VH, V = W\pm, Z$). Studying the rare VH and VBF production mechanisms allows for probing the Higgs boson coupling to vector bosons. Finally, Higgs bosons can be produced in association with a pair of top quarks (ttH) or a single top quark (tH). The ttH mechanism is of particular interest as it allows for the direct determination of the magnitude of the top Yukawa coupling y_t , in contrast with the indirect determination from ggF. The tH mechanism, about a factor of 10 rarer than the previous, allows for the determination of the sign of y_t .

The mass m_H is a free parameter of the theory. When the mass of the Higgs boson is fixed, its couplings are well known, the production rates and the partial widths can be calculated. Now let us explain a bit more in detail the production modes of the Higgs boson.

a gluon-gluon fusion (ggF):

at high center-of-mass energy, the gluon-gluon fusion $pp \to gg \to H$ is the Higgs boson production with the largest cross-section [§]. This production is mediated by the exchange of a virtual heavy quark (top or bottom) loop. The contribution from lighter quarks propagating in the loop are suppressed proportionally to m_q^2.

b Vector boson fusion (VBF):

It is the process with the second-largest cross-section. Two W or Z bosons produced from colliding quarks interact to originate the Higgs boson. The scattered quarks give rise to two hard jets in the forward and backward regions. The jets are the characteristic signature of the process used in the analyses to exploit this production mode.

c Associated production with a vector boson (VH):

In this channel, the Higgs boson is produced in association with a W or a Z boson. As for the VBF case, this channel is driven by quarks, which produces the vector boson V (with $V = W$ or Z) that emits the Higgs boson. The ZH production also has the contribution

[§]The gluon fusion represents almost 90% of the total Higgs cross-section.

from the two gluon's initial state and constitutes an irreducible background. The presence of the vector boson in the finals state is used experimentally to identify better the events as well as to reduce the contribution of background events.

d Associated production with a pair of heavy quarks ($tt^{-}H$, $bb\bar{b}H$):

Two colliding gluons emit a quark and anti-quark pair in which the quark can be the top or the bottom quark. One quark from one gluon and an anti-quark from the other gluon combine and form a Higgs boson. These production mechanisms have the lowest cross-sections at LHC but they present the opportunity to study the direct coupling of the Higgs boson to fermions.

Fig.2.9a shows the Feynman diagrams for the main Higgs production modes at LHC and Fig. 2.9c shows the cross-sections of the Higgs boson with $m_H = 125\ GeV$ as a function of the $\sqrt{s}$ center of mass energy. And Figure 2.9b shows the Higgs boson decay branching ratios as a function of its mass m H and the corresponding values for a mass of m_H

Table 2.2 summarizes the Higgs boson production cross-sections for a Higgs boson mass $m_H =$ 125 GeV at a center of mass energy $\sqrt{s} = 13$ TeV.

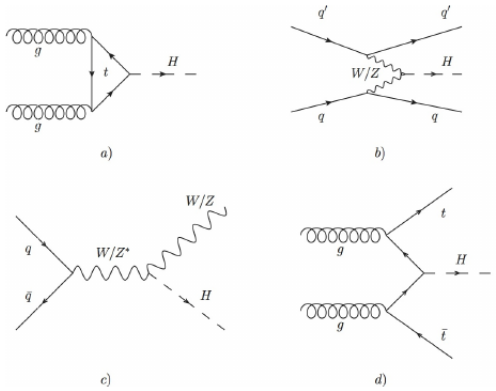

(a) Feynman diagram

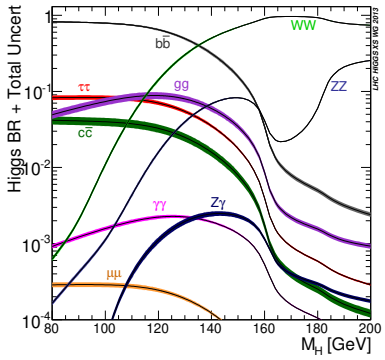

(b) Higgs boson decay branching ratios

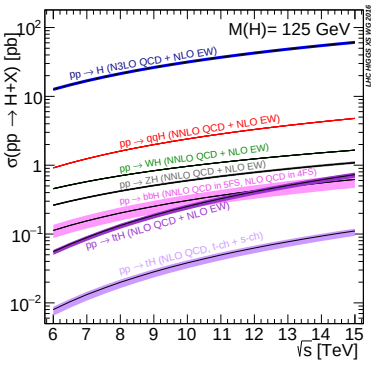

(c) SM Higgs boson production cross sections

Figure 2.9: In the Figure 2.9a we have the Feynman diagram for the Higgs production: (a) gluon-gluon fusion, (b) vector boson fusion, (c) associated production with a vector boson, (d) associated production with a pair of top quarks. In Figure 2.9b we have the Standard Model Higgs boson decay branching ratios as a function of the Higgs mass m_H. In Figure 2.9c we have the standard Model Higgs boson production cross sections as a function of the centre-of-mass energy for $m_H = 125$ GeV [Gro23]

Decay	BR	Observed
bb	58%	✓
WW	22%	✓
gg	8.6%	
ττ	6.3%	✓
cc	2.9%	
ZZ	2.6%	✓
$\gamma\gamma$	0.23%	✓
$Z\gamma$	0.15%	
$\mu\mu$	0.02%	

Table 2.2: Branching fractions of the main Higgs boson decay modes for a SM Higgs boson of mass $m_H = 125.09$ GeV. [dF$^+$17]

2.6.2 Higgs pair production and decay

The potential of the scalar Higgs field, Φ, written in Equation 2.71, is given by

$$V(\Phi) = \frac{1}{2}m_h^2 h^2 + \lambda v h^3 + \frac{\lambda^{'}}{4}h^4$$

Where λ is known as the Higgs trilinear self-coupling and $\lambda^{'}$is the quartic Higgs self-coupling. In the SM, λ is given by:

$$\lambda = \lambda^{'} = \frac{m_h^2}{2v^2}$$

and, therefore, is predicted when the Higgs mass is known. Experimental measurement of the true value of λ is an essential task in determining the shape of the Higgs potential; any deviation from the predicted value implies the existence of BSM phenomena. By experimentally measuring m_h and λ, the value of the VEV, v, can be calculated and compared with the predicted value - a direct test of electroweak symmetry breaking and, hence, the SM.

Terms of the form $\lambda v h^3$ and $\lambda/4h^4$ (assuming $\lambda = \lambda^{'}$) in the SM Lagrangian, Equation 2.84, generate di-Higgs and triple-Higgs production, respectively. Higgs pair-production is the only LHC process in which the coupling between three Higgs bosons can be tested at tree level.

At the LHC, di-Higgs production proceeds through the five main mechanisms that are listed below in decreasing order of their cross-section. Some representative Feynman diagrams illustrate the Higgs boson couplings involved [B$^+$13]: The dominant Higgs boson pair production mode is ggF through the destructive interference of two LO diagrams shown in Figure 2.10a, involving top-quark loops and the triple Higgs self-coupling.

a **Gluon fusion $gg \to HH$:**

The dominant Higgs boson pair production mode is ggF. It involves either the production of a Higgs boson pair through the trilinear Higgs boson self-coupling (triangle-type contributions), or the radiation of two on-shell Higgs bosons from a heavy quark loop (box-type contributions), as shown in the Feynman diagrams in Figure 2.10a [FFH$^+$14]. [EMNN87]. The cross-section consequently depends on λ_{HHH} and on the top quark Yukawa couplings y_t. In The **triangle diagram** in which a virtual Higgs boson is produce by the same mechanism as a single Higgs productions, it decays into a Higgs pair, involving the self coupling. We can see that the Feynman diagram is in the s-channel in which a virtual Higgs boson propagator decays to a Higgs pair via the Higgs self-coupling λ. And the **Box diagram**, the two Higgs bosons are directly radiated from a heavy top-quark in a process only involving the Yukawa couplings. The destructive interference of two LO diagrams shown in Figure 2.10a, involving top-quark loops and the triple Higgs self-coupling. In the box diagram of the top-quark loops. The top-quark Yukawa coupling y_t is present in

two vertices. Hence, the contribution of this diagram to the amplitude is proportional to y_t^2. In contrast in the triangle diagram there is y_t in one vertex and the triple Higgs self-coupling λ_{HHH} in the other vertex and the contribution of this diagram is proportional to the product of y_t and λ_{HHH}. Therefore, studying this process allow us directly test both the triple Higgs self-coupling and the top-quark Yukawa coupling. The SM cross-section for Higgs boson pair production via ggF at $\sqrt{s} = 13$ TeV [BSG13], calculated at Next-to-Leading Order (NLO), is:

$$\sigma = 33.41 \quad fb$$

Three orders of magnitude smaller than the single Higgs production cross section. This accounts for more than 90% of the total Higgs boson pair production cross-section, followed by the V BF production which is two orders of magnitude smaller, therefore, only this production mode is considered in this thesis.

The di-Higgs system decay has a variety of different final states resulting from all the possible combinations of the decays of the two Higgs bosons. Figure 2.11 shows the branching ratios for all the possible combinations of Higgs decay channels that have been observed, assuming SM Higgs bosons with $m_H = 125.09$ GeV. The search presented in this thesis is performed in the $bb\bar{\tau}^+\tau^-$ final state, where one Higgs boson decays to a b-quark pair and the other to a τ-lepton pair, which has the third largest observable BR corresponding to 7.4%. Particularly, this work focuses on the final state with both τ-leptons decaying hadronically, $bb\bar{\tau}^+_{lep}\tau^-_{had}$, which makes up 45.6%

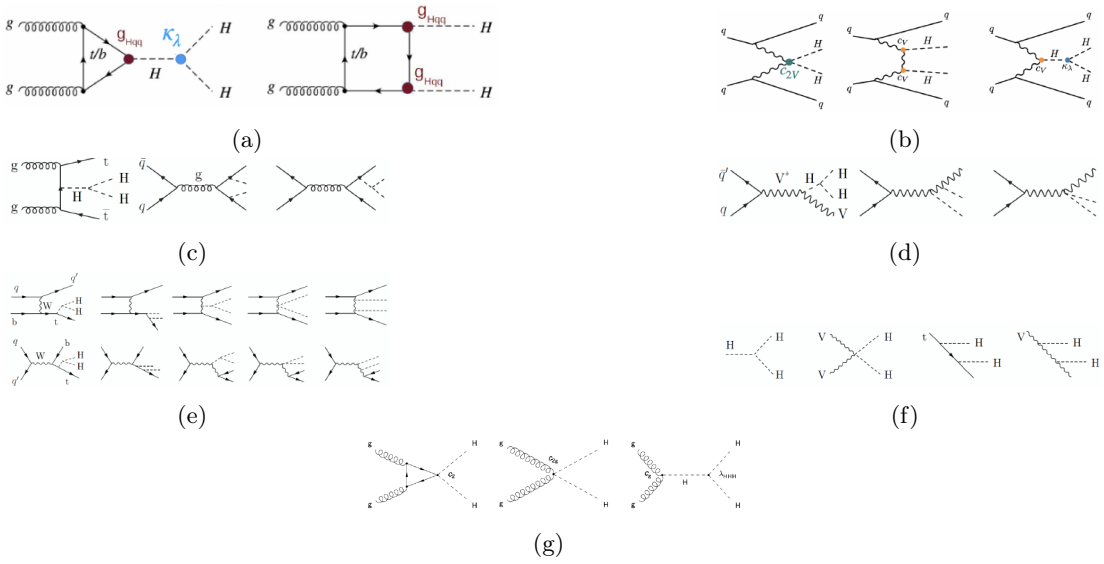

Figure 2.10: Diagrams contributing to Higgs pair production: Figure 2.10a gluon gluon fusion diagrams, Figure 2.10b vector-boson fusion, Figure 2.10d double Higgs-strahlung and Figure 2.10c double Higgs bremsstrahlung off top quarks and Figure 2.10e single top quark associated production. Figure 2.10f Double Higgs boson interaction modes. Figure 2.10g BSM new Feynman diagrams predicted at the same perturbative order of SM diagrams in Figure 2.10a. The trilinear (quadrilinear) Higgs coupling $\lambda_{HHH}(\lambda_{VVHH})$. Contribution is visible between three dashed (two dashed plus two waves) lines.

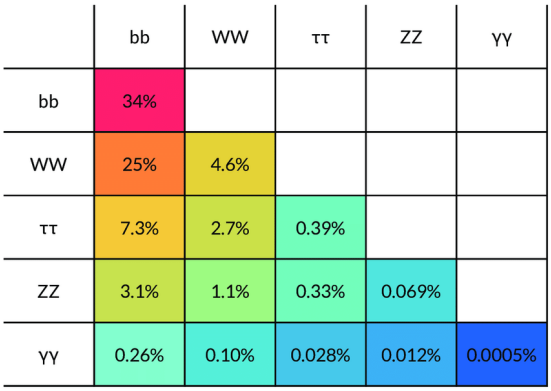

Figure 2.11: Di-Higgs system decay branching ratios assuming SM Higgs bosons $m_H = 125.09$ GeV

Chapter 3

The Large Hadron Collider(LHC)

3.1 Overview of the LHC

The Large Hadron Collider(LHC) is the world's largest and most powerful particle accelerator. The LHC aim is to become a tool for physicists to test the predictions of different particle physics theories and hunt for many new particles predicted by super-symmetric theories. The discovery of the Higgs boson is considered one of the most significant achievements of the LHC.

The LHC, built by the European Organisation for Nuclear Research (CERN) between 1998 and 2008, is underground inside a 27 km depth of 50-175 m below the Franco-Swiss border, which is located at the border as shown in Figure 3.1. Inside the tunnel, it is a ring consisting of about 10000 superconducting magnets with an accelerating structure to boost the energy of the particles. The superconducting magnets ring guides two different high-energy beams that travel in the opposite direction in the ring with its strong magnetic field. In order to get magnetic field strong enough, most parts of the accelerator are connected to the distribution system of liquid helium, especially the superconducting magnets, to cool down. The temperature in the ring could be as low as -271.3 $C^{\cdot}$, which is very close to absolute zero degrees.

The LHC had its first run started on 10th, Sept, 2008. While the first operational run started from 2009 to 2013 with the beams center of mass energy around 7 TeV. After this first operational run, which is Run I, the LHC was shut down from 2013 to 2015 for system upgrades aiming collisions at 14 TeV . On 5th, April 2015, the LHC restarted after the 2 year-long break. The center of mass collision energy had reached 13 TeV after the upgrades, which is $Run\ II$. During Run II, the combined energy increased, and the proton-proton collisions luminosity has been increased to 40% above the design value.

The LHC primarily collides proton beams, while it also collides with beams of lead nuclei. There are four crossing points on the LHC ring where the two opposite beams get collided. Seven different detectors designed for different research purposes are placed around these crossing points. The four major ones are ATLAS, CMS, ALICE and LHCb. Among them, ATLAS [dF+17] and CMS are the two general purpose detectors. ALICE [Col08a] is to study quark-gluon plasma which existed shortly after the Big Bang. LHCb [Col08b] has another different purpose of research which is to mainly investigate anti-matter. The data analysis described in this article uses the data recorded by the ATLAS detector.

The protons are extracted from the hydrogen atoms and are accelerated in the order of LINAC (50 MeV), BOOSTER (1.4 GeV), Proton Synchrotron (PS ; 25 GeV), Super Proton Synchrotron (SPS ; 450 GeV), and LHC (6.5 TeV) as shown in Figure 3.2. In the LHC, protons are bundled into 2500 bunches, and each consists of 1.1 × 1011 protons and the oppositely running bunches collide in 40 MHz with the center-of-mass energy of 13 TeV. The size of the bunch is 8 cm in the direction of the acceleration and 16.7 μm in the vertical direction. As a result, the instantaneous luminosity of the pp collision reaches about $1034 cm^{-2}\ s^{-1}$ ($\sim$ 40 MHz $\cdot$ (1.1 × 1011)2 /(4π $\cdot$ (16 μ)2)). There are four interaction points in the LHC; ATLAS, CMS, LHCb, and ALICE. ATLAS and CMS are detectors for the general purpose of measuring of high energy physics.

Here will be focusing on the ATLAS detector, which has been designed to allow several types of research:

- the search for the SM Higgs boson and the measurement of its properties;
- Supersymmetry searches;
- precision tests of electroweak interactions, flavor physics and QCD;
- measurements of the properties of the top quark;

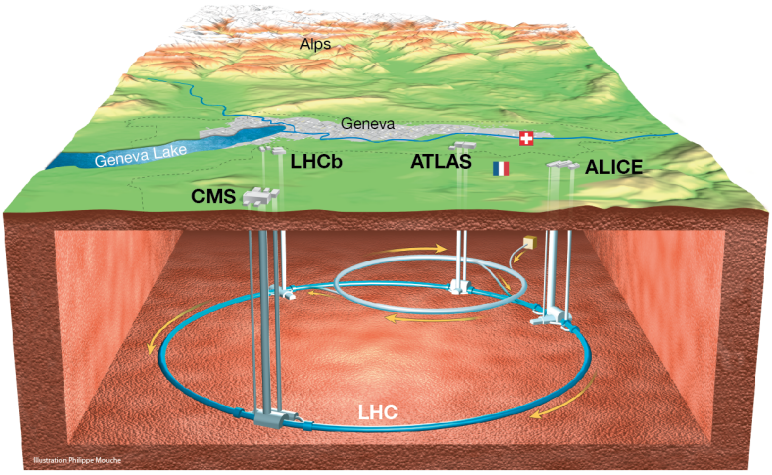

Figure 3.1: LHC tunnel and the main experiments placed at its collision points (ATLAS, ALICE, CMS and LHCb) relative to Geneva and the French-Swiss border.

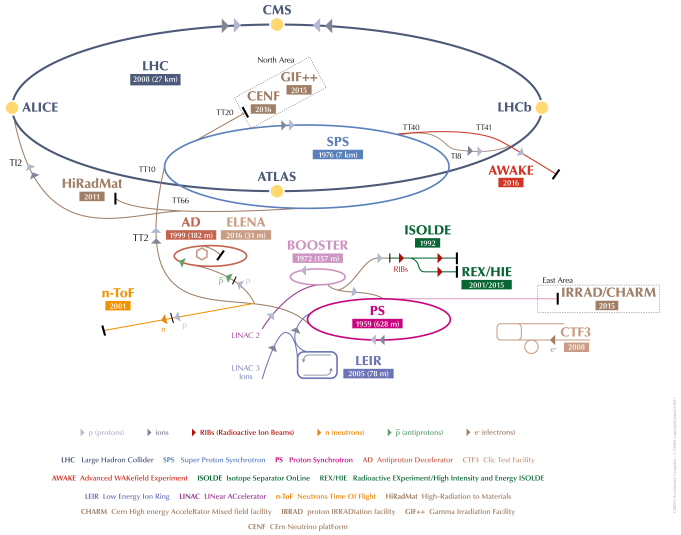

Figure 3.2: The CERN Accelerator Complex [Mob16]

- generic searches for new particles and interactions (the so-called exotic searches).

In order to deal with these challenges, ATLAS was designed to have:

Detector Component	Design Resolution	η Coverage	
		Measurement	Level 1 Trigger
Tracking	$\sigma_{P_T}/p_T = 0.05\%\ p_T \bigoplus 1\ \%$	± 2.5	None
EM Clorimeter	$\sigma_E/E = 10\ \% \sqrt{E} \bigoplus 0.7\ \%$	± 3.2	± 2.5
Hadronic Calorimeter			
Barrel and End-Cap	$\sigma_E/E = 50\ \% \sqrt{E} \bigoplus 3\ \%$	± 3.2	± 3.2
Forward	$\sigma_E/E = 100\ \% \sqrt{E} \bigoplus 10\ \%$	$3.1 < \lvert\eta\rvert < 4.9$	$3.1 < \lvert\eta\rvert < 4.9$
Muon Spectrometer	$\sigma_{P_T}/p_T = 10\%$ at $p_T = 1$ Tev	± 2.7	± 2.4

Table 3.1: Performance goals of the ATLAS detector. Units of p_T and E are GeV [A$^+$99]

3.2 The ATLAS Detector

All our experimental discoveries that underpin our understanding of particle physics and rely on particle detectors. The toroidal LHC apparatus (ATLAS) is the largest volume general-purpose particle detector ever constructed, it is installed at the Large Hadron Collider (LHC), a particle accelerator at CERN (the European Organization for Nuclear Research) in Switzerland. The goal of the ATLAS detector is to measure the momentum,energy and charge of every decay product of particles produced through highly energetic proton-proton collisions. For example: The ratio of the momentum over the electric charge of a particle can be determined from the curvature of the particle's path in a magnetic field. The energy of a particle can be estimated by sampling how its energy propagates through layers of absorbing material like lead and iron.

ATLAS 3.3 is one of two general purpose particle physics detectors at the LHC (the other one is CMS). It is designed to detect particles from both pp and ion-ion interactions. The high center-of-mass energy and the high luminosity of the LHC pp collisions allow for the study of physics at the TeV scale. The detector has been designed to allow several types of research: [EC21a].

- The search for the SM Higgs boson and the measurement of its properties;
- Supersymmetry searches;
- precision tests of electroweak interactions, flavor physics and QCD;
- measurements of the properties of the top quark;
- generic searches for new particles and interactions (the so-called exotic searches)

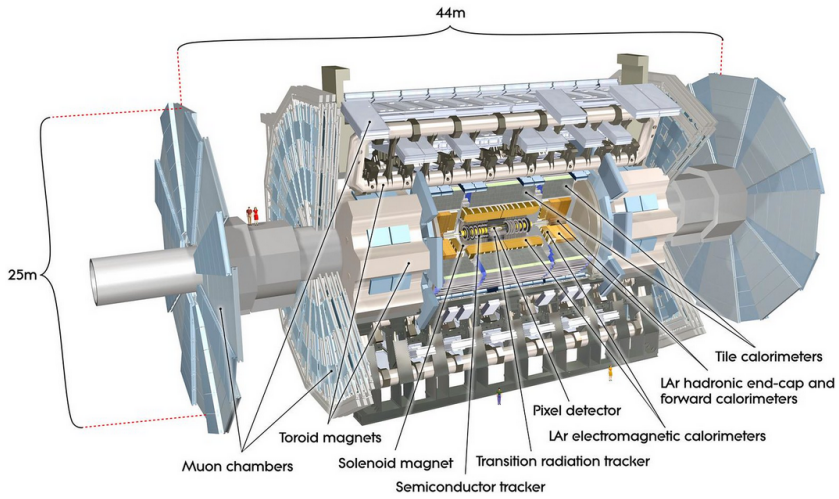

Figure 3.3: Cut-away view of the ATLAS detector and sub systems

The ATLAS detector systems can be broken into four major categories, listed here in radialorder, starting closest to the beam pipe and moving outwards:

- **Inner Detector (ID)**: Measures particle tracks in a uniform longitudinal magnetic field.
- **The calorimetry system** : Comprised of an electromagnetic calorimeter and a hadronic calorimeter measuring respectively energy deposits of particles originated from electromagnetic and from hadronic showers
- **Muon Spectrometer (MS)**: Measures the tracks of charged particles which make it through the Hadronic Calorimeter. These are predominantly muons.
- **Trigger system** : In charge of selecting the interesting event for permanent storage, while rejecting a high rate of background processes.

Many types of particles decay before they reach the detector, so their properties must be inferred from the properties of their decay products using conservation laws. The production of a Higgs boson ($m_H = 125GeV$), for example, may be inferred with the event selection that requires two isolated photon candidates satisfying p_T and photon identification criteria.

Conversely, sufficiently long-lived particles which are not charged under the electromagnetic or strong nuclear forces such as neutrinos, will fly through the detector without being measured.

3.3 Luminosity and pile-up

3.3.1 Luminosity

The number of events expected from a process with a cross-section σ is given by the product:

$$N = L\sigma$$

where L is the integrated luminosity given by $\int_0^T \mathcal{L}dt$. Here, T is the length of 0time the ATLAS detector has been collecting data for and $\mathcal{L}$ is the instantaneous luminosity. The instantaneous luminosity depends only on the parameters of the beam and is given by the equation:

$$\mathcal{L} = \frac{N_b n_b f_{rev} \gamma_r}{4\pi\epsilon_n \beta^*} F$$

Where (the nominal parameters for the LHC are given in parenthesis):

- N_b: is the number of particles per bunch ($\sim 10^{10} \sim 10^{11}$
- n_b: is the number of bunches per beam (2808)
- f_{rev}: is the revolution frequency (11,245 Hz)
- γ_r: is the relativistic gamma factor (~ 7000)
- ϵ_n: is the transverse normalized beam emittance, related to the spread of particles in the beam (3.75 μm)
- β^*: is the beta focus function at the collision point, related to how tightly the magnets are focused at the interaction point (0.55 m)
- F: is the geometric luminosity reduction factor if the beams do not collide head-on. A crossing angle of 285 μ rad is introduced to prevent collisions outside the nominal interaction points

Currently, the LHC is in what is known as Run 3. During Run 3, the LHC is expected to deliver an integrated luminosity of 300 fb^{-1} from collisions at a center-of-mass energy of 14 TeV. After that there will be a third long shutdown followed by a new operation period called High-Luminosity-LHC (HL-LHC), during which the instantaneous luminosity will reach$5 - 7 \times 10^{34}$ $cm^{-2}s^{-1}$

3.3.2 Pile-Up

In a single bunch crossing, multiple proton-proton interactions give rise to final state particles which traverse the detector. Proton-proton collisions surplus to the collision of interest are collectively referred to as **pile-up**. **Pile-up** events pollute the reconstruction of the final state of the collision of interest, forming a background which is difficult to model and must be considered in every physics analysis.

The pile-up background originates from five sources [MtAC14]:

- **In-time pile-up**: Which refers to the additional proton-proton collisions occurring in the same bunch-crossing as the collision of interest, of which up to 80 are expected in Run II;
- **Out-of-time pile-up**: Which refers to the additional proton-proton collisions occurring in bunch-crossings just before and after the collision of interest, which are a challenge for the detector subsystems that have sensitivity windows longer than 25 ns (the interval between bunch crossings);

- **The cavern background**: i.e, the gas of neutrons and protons inundating the detector during an LHC run, which give rise to random hits in the muon detector;
- **Beam halo events**: Which are sprays of sprays of muons induced by an outlier of the proton beam hitting beam collimators;
- **beam gas events**: which occur when protons collide with residual gas inside the beam pipe.

The two main sources of pile-up are in-time pile-up and out-of-time pile-up. These present a growing concern as the instantaneous luminosity increases.

3.4 Magnet System

The ATLAS detector uses a unique hybrid system of four large superconducting magnets [94] to bend charged particles to facilitate the measurement of their momenta. The momentum of a charged particle is directly proportional to the curvature of its trajectory through a magnetic field. The four magnets generate a magnetic field over a volume of 12000 m^3 (defined as the region in which the field exceeds 50 mT). Their configuration is shown in Figure 3.4.

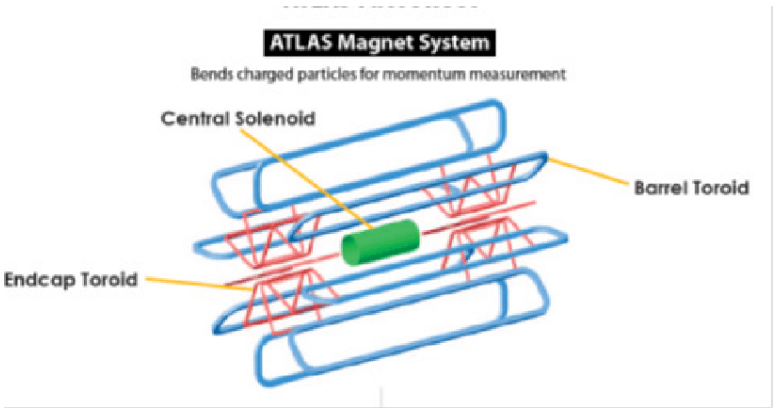

Figure 3.4: Diagram of the ATLAS detector magnet system.

The inner solenoid magnet [cs97] immerses the ID in a 2.0 T axial magnetic field which runs parallel to the beam axis. A field of this strength is required to bend the most energetic particles sufficiently for their momenta to be determined. At around 5.3 m in length, 2.4 m in diameter, and 4.5 cm thick, the solenoid is a single-layer coil wound with 9 km of aluminium-stabilized superconducting wire. Because the magnet is situated in front of the calorimeters, it is imperative that the radiative thickness of the magnet (0.66 radiation lengths) is minimised. It operates at a nominal current of 7.73 kA and produces a field with a store energy of 38 MJ.

Three toroid magnets, one in the barrel region [BBBB97] and two smaller end-cap magnets [ect97], provide a toroidal field for the MS. The barrel toroid is 25.3 m in length with a 20.1 m outer diameter, providing 0.5 T magnetic field storing storing a total energy of 1.08 GJ. It is constructed from 8 separated coils surrounding the calorimets and the end-cap toroids and covers $|\eta| < 1.4$ The end-cap covers the range $1.6 < |\eta| < 2.7$ and has a field strength of 1.0 T. The field in the transition region,$1.4 < |\eta| < 1.6$, is the result of contributions from the barrel and end-cap magnets. This magnet configuration provides a field that is mostly orthogonal to the muon trajectories.

3.5 Inner Detector (ID)

The magnetic field produced by the superconducting magnets is able to immerse the inner detector [CER97] of ATLAS(2 T solenoidal field).

The responsibility of the Inner Detector The (ID) [CER97] pattern recognition, measuring momentum and vertex and identifying electrons with the discrete high-resolution semiconductor

pixel [Jac05] and the strip detector in the inner part of the tracking volume. The straw-tube tracking detector of the inner detector is designed to be able to generate and detect transition radiation [Min17].

The Inner Detector (ID) is composed of three sub-detector systems that exploit different technologies. The high-granularity pixel detector that utilizes silicon pixels is closest to the interaction point. This allows precise measurements of tracks from charged particles close to the interaction point. This enables reliable Reconstruction of the primary interaction point and secondary vertices. This is followed by the Semi-Conductor Tracker (SCT) detector that utilizes silicon micro-strips. The silicon detectors are surrounded by a transition radiation tracker (TRT) that uses straw-tubes. The ID is shown in Figure 3.5. It is immersed in the 2 T magnetic field produced by the solenoid, which is placed between the ID and the calorimeter. The inner detector is divided into two sections, the barrel, which is parallel to the beam axis and two end-caps perpendicular to the beam axis. In the barrel region, both the Pixel and SCT detectors are arranged as concentric cylinders around the beam axis while in the end-cap regions, the detectors are disks. This set up means the ID is capable of reconstructing charged particle tracks. And at the end of Run 1, the insertable b-layer (IBL) was added to the pixel detector in order to improve the tracking and b-tagging efficiency for Run 2. This setup means the ID is capable of reconstructing charged particle tracks up to $|\eta| \leq 2.5$

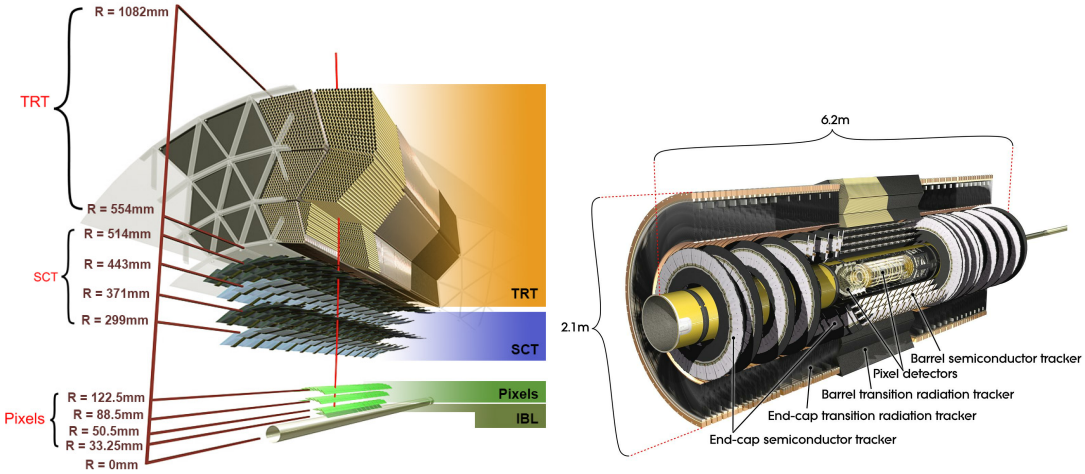

(a) Pixel detector

(b) Inner Detector

Figure 3.5: Left: The ATLAS Inner Detector. Right: Vertical cut out of the ATLAS Inner Detector. The drawing shows a charged track with $p_T = 10$ GeV at an η of 0.3 [Col08a].

Semiconductor tracker

The SCT surrounds the pixel detector. It consists of four layers of silicon strip detector modules in the barrel and nine layers in the end caps. Particles typically pass four of these layers. The modules in the barrel have two layers of silicon that are slightly rotated against each other, which allows for the determination of the position along the strips. The resolution in the barrel (end caps) is about 17 μm in the$R - \phi$-plane (along ϕ) and about 580 μm along the z-axis (R-axis) [Col08a].

Pixel Detector

The silicon Pixel Detector (PD) [101] is the first detector a particle from the interaction point will traverse: The first layer is 50.5 mm away from the interaction point. The pixel detector has 3 layers in the barrel and in the end-cap. Each module has 46080 pixels, resulting in a total of 80.4 million pixels. The pixel size is 50 μm in the $R - \phi$ direction and 400 μm in the z-direction.

The pixel detector is the next closest detector to the interaction point, the innermost layer being located at R = 50.5 mm. It consists of cylindrical layers ordered around the beam in the

central region (barrel) and of disks arranged radially in the end caps. Particles typically pass three of these layers. The pixels have a minimum size of $R-\phi \times z = 50 \times 400 \mu m^2$ and a total of 80 million read-out channels is reached. The track resolution in the barrel (end caps) is about 10 μm in the$R-\phi$-plane (along ϕ) and about 115 μm along the z-axis (R-axis) [Col08a]

Insertable B-Layer

During Run I, the PD was the innermost sub-detector of the ATLAS detector. For Run II, the Insertable B-Layer (IBL) [CDE$^+$10] was commissioned. The main motivation of the IBL was to improve the pixel detector performance for Run II despite possible radiation damage to the first layer of the PD and the increasing bandwidth requirements associated with the increasing LHC luminosity. During the first Long Shutdown, the IBL was inserted between the new, smaller-radius beryllium beam pipe and the existing first layer of the PD.

The IBL is positioned at a radius of 33.2 mm from the beam axis and consists of around 12 million pixels with dimensions $50 \times 250 \mu m^2$. These are arranged such that the IBL gives full coverage in azimuthal angle, ϕ, and covers a pseudorapidty of $|\eta| < 2.9$. Studies [CDE$^+$10] show that the IBL is robust against pile-up and improves the quality of the impact parameter reconstruction and vertexing and, therefore, the b-tagging performance.

Semiconductor tracker

The SCT is a silicon microstrip detector that consists of strip-type semiconductor sensor with 4 layers in barrel region and 9 layers in end-cap region as we can see in Figure 3.5, thus allowing for a two-dimensional measurement. Four layers are used in the SCT barrel region and provide a spatial resolution of$17 \mu m(R-\phi) \times 580 \mu m(z)$. Nine disks with one set of strips running radially are placed in the end-cap region. The SCT is able to distinguish tracks if they are separated by more than 200 μm.

Both silicon detectors cover the pseudorapidity region up to $|\eta| < 2.5$ and they are complemented by 4 mm diameter straw tubes of the TRT, which provide track measurement in $R-\phi upto|\eta| < 2.0$. The straw tubes are filled with a X_e-based gas mixture and have an unique ability to identify electrons by detecting the transition radiation photons. The TRT typically measures 36 hits per track with a hit position accuracy of 130 μm per straw. A track is usually considered to be of good quality if it crosses three-pixel layers and eight strip layers. The designed resolution of the tracking system is

Transition Radiation Tracker

The TRT surrounds the SCT and is the outermost part of the inner detector. It consists of gas-filled drift tubes along the z-axis in the barrel (144 cm long) and along the radial direction in the end caps (37 cm long) [A$^+$08]. The gas consists of Xenon (70%), CO2 (27%), and O2 (3%), and the charged particle ionize the gas. The tubes have a diameter of 4 mm and a thin wall out of two 35 μm thick multi-layer films [62]. The TRT contains a large number of polypropylene fibers with a diameter of 9 μm, which serve as transition radiation material.

The TRT only provides $R-\phi$ information with an intrinsic accuracy of 130 μm per straw. In the barrel region, the straws of the TRT are parallel to the beam axis with a length equal to 144 cm. The barrel straws are divided into two halves at around $|\eta| = 0$. In the end-cap region, the straws are arranged radially in wheels with a length of approximately 37 cm long. The total number of TRT readout channels is approximately 351000.

The combination of precision trackers at small radius together with the TRT at a larger radius gives very robust pattern recognition and high precision in$R-\phi$ and z coordinates. Hits at large radius contribute significantly to the momentum measurement.

The inner detector system provides tracking measurements in a range matched by the precision measurements of the electromagnetic calorimeter. Besides these features, the electron identification capabilities are enhanced by the detection of transition-radiation photons in the xenon-based gas mixture of the straw tubes. Impact parameter measurements and vertex measuring for heavy-flavor and $\tau-$lepton tagging could also be done by the semi-conductor trackers. The innermost layer of pixels can also enhance the measurement of the secondary vertex too.

The amount of material used by the ID is essential to understand the behavior of particles before they reach the calorimeters. For example, photons can convert into e^+e^- pairs, and electrons can lose energy through bremsstrahlung emissions which impacts the energy measurements of these particles in the calorimeter.

3.6 Calorimeters

The main purpose of the calorimeters is to measure the energy and direction of motion of electrons, photons and sufficiently-long-lived hadrons. With this one can reconstruct the hadronic jets. All particles apart of muons and weekly interacting particles will deposit almost all of their energy in the calormeters.

For electrons, the energy loss at high energy is dominated by Bremsstrahlung, while energetic photons undergo e^+e^- pair production. The characteristic radiation length,X_0, depends on the type of medium through which the particles are travelling. ATLAS utilizes sampling calorimetry, which means that the calorimeters are constructed from alternating layers of a passive absorber, which produces the particle showers, and active detector layers, which measure the particle energy. As such, a fraction of the total particle energy is deposited in the passive material and is not measured; the overall energy must be deduced from the definite measurements taken in the active detector layers.

An incoming electron or photon causes a cascade of interactions which are electromagnetic (an (EM) shower), After the particles in the shower reach sufficiently low energy, they are stopped and absorbed. This creates a cluster of measurable signals that is later calibrated to measure the energy of the initial particle.

Energetic hadrons develop hadronic showers through a succession of inelastic hadronic interactions. The interaction length, λ, is significantly larger than chi_0 for the same medium. The Hadronic Calorimeter (HCal) is thus positioned further away from the interaction point compared to the Electromagnetic Calorimeter (ECal). In addition, hadronic showers spread more in the transverse direction compared to EM showers since the opening angle of the cascade scales with the interaction length. Pions, being the lightest mesons, dominate hadronic showers. Approximately one-third of the produced pions are neutral,π^0, and, as a result of $\pi^0 \to \gamma\gamma$ decays, their energy is dissipated in the form of EM showers.

ATLAS has two distinct calorimeter subsystems [cp96], as illustrated in Figure 3.6: the Electromagnetic Calorimeter (ECAL), which measures electrons, photons and the electromagnetically interacting components of jets; and the Hadronic Calorimeters, which measure the strongly-interacting components of jets.

As mentioneted above. The calriometers are divided as mention above into two Electromagnetic (EM) and Hadronic sections as we can appreciate in Figure 3.6. Each type has sub-components that enables the reconstruction of the tranverse and longitudinal energy depositions. The ECal has an acceptance of $|\eta| < 3.2$ and the acceptance of HCal is $|\eta| < 4.9$. And to be able to account for the missing energy and momentum, it is essential that the calorimeter cover a solid angle as close to 4π as possible *.

The ATLAS detector uses sampling calorimeters, meaning that the system is designed to have alternating layers of passive and active material, the passive material acts as an absorber while the active one interacts with the event particles and originates cascades of secondary particles.

3.6.1 EM Calorimeters

At The innermost calorimeter system is the liquid argon (LAr). The Electromagnetic Calorimeter (ECAL) [lac96]. All particles besides neutrinos and muons will deposit significant fractions of their energy in the EM calorimeter. However photons and electrons deposit most or all of their energy at this stage.

The ATLAS electromagnetic calorimeter is a sampling calorimeter using lead absorbers and liquid argon (LAr) as the active material. The absorber and active layers in each section have

*For more details refer to [BDWW16]

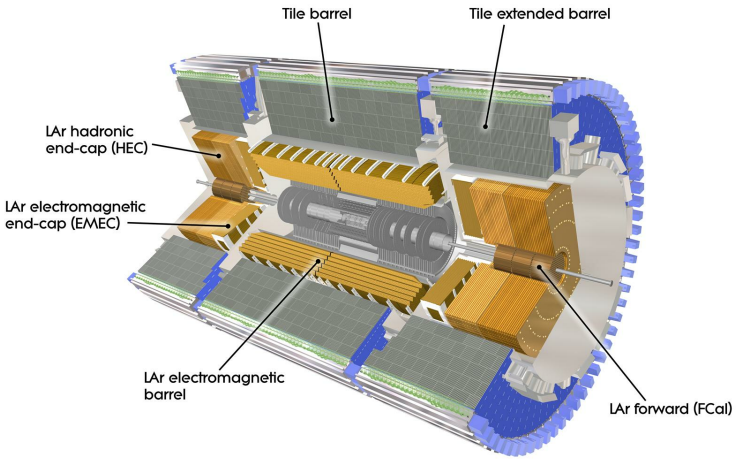

Figure 3.6: The calorimetry system of the ATLAS detector

an accordion shape (see Figure 3.6). The Layers of each material are placed in alternating order. A particle traveling through the detector is likely to interact with the high-density absorber material, lead (Pb), and produce a shower of particles. The products of this shower can ionize the active material, LAr, leading to drifting charges that can be measured by electrodes placed between the LAr and the absorber. the (EM) calorimeter is divided into a barrel section, covering the pseudorapidity region $|\eta| < 1.475$, and two end-cap sections, covering the pseudorapidity regions $1.375 < |\eta| < 3.2$. The transition region between the barrel and the end-caps, $1.37 < |\eta| < 1.52$,. The $|\eta|$ region between 1.37 and 1.52 ("crack region"), which corresponds to the transition region between the barrel and end-cap cryostats, suffers from a significantly reduced resolution compared to the rest of the ECal. This region is excluded in many physics analyses that require high-precision measurements of electrons, $\tau-$leptons or photons, including those in this thesis.

Electrons, photons and pions are discriminated by checking for isolated tracks pointing to the given EM calorimeter deposit, by the shower shape, and by the fraction of energy deposited in the first and last layers of the EM calorimeter and in the hadronic calorimeter .

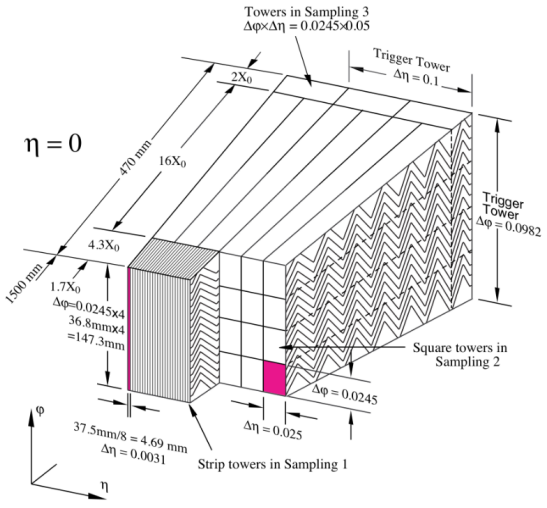

(a) Electro Magnetic calorimeter

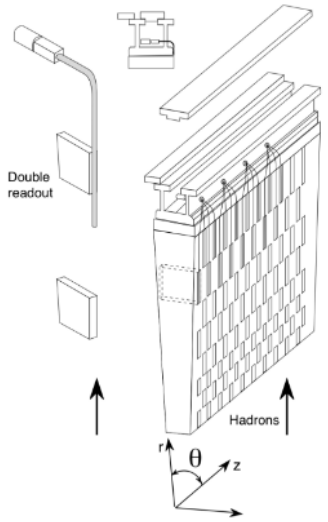

(b) Tile Calorimeter

Figure 3.7: Left: The ATLAS Inner Detector. Right: Vertical cut out of the ATLAS Inner Detector. The drawing shows a charged track with $p_T = 10$ GeV at an η of 0.3 [Col08a].

Electrons, photons and pions are discriminated by checking for isolated tracks pointing to the

given EM calorimeter deposit, by the shower shape, and by the fraction of energy deposited in the first and last layers of the EM calorimeter and in the hadronic calorimeter.

3.6.2 Hadronic Calorimeter

The hadronic calorimeter uses two types of sampling detectors: Liquid argon-copper in the end-cap region and iron-scintillating *tiles* in the barrel region. The LAr/Cuend-cap calorimeters are similar to the ones described in the ECal, with the cave at that the layers are planes rather than accordion shaped as shown in 3.6 Hadrons only leave a fraction of their energy in the ECAL systems so the hadronic calorimeter system (HCAL) surrounds the ECAL system in both the barrel and the end-cap. The HCAL relies on the strong interaction to measure the hadrons energy and to stop them reaching the muon system.

A steel-scintillator-sampling calorimeter (called TileCal) is used in the barrel region. It consists of three parts, the barrel, which extends to $|\eta| \leq 1.0$ and two extended barrels which cover $0.8 \leq |\eta| \leq 1.7$. The steel absorber causes hadrons to produce lower momentum hadrons, electrons and photons. These particles excite atoms within the scintillator material which produce scintillation light which is read out by photomultiplier tubes. In the hadronic end-cap calorimeter (HEC), liquid argon is used as the active material and copper and tungsten as the passive material. It shares the same cryostat as the EMEC and covers the region $1.5 \leq |\eta| \leq 3.2$

3.6.3 Forward calorimeter

The Forward calorimeter (FCal) covers the $3.1 < |\eta| < 4.9$ region. It is split into one electromagnetic- and two hadronic-calorimeter layers.The electromagnetic layer uses copper (LAr) as its passive (active) medium.For the hadronic components of FCal, tungsten is used instead of copper.

3.7 Muon Spectrometer

The ATLAS detector's outermost and largest subdetector is the high-resolution Muon Spectrometer (MS), which is designed to identify and measure the momenta of muons leaving the calorimeters in the range $|\eta| < 2.7$. A diagram of the MS is shown in Figure 3.8a. If the calorimeter is sufficiently thick, the majority of particles emerging from the calorimeters will be muons (ignoring neutrinos), because they do not tend to produce electromagnetic showers like electrons or have hadronic interactions. The trajectories of the muons are measured in large wire chambers and can be matched to high-transverse-momentum charged particles measured in the tracker, reducing the effects of hadrons 'leaking' out of the back of the calorimeter. If there is a magnetic field in the region of the muon chambers, the muon trajectory can be used to determine the muon momenta. The momenta of the muon scan be measured independently in the tracker and combined with the measurement in the muon spectrometer to get the best precision.

The barrel region is constructed from chambers arranged in three cylindrical layers around the beam axis, whereas the chambers in the endcaps are installed vertically. Over most of the pseudorapidity range, precision tracking is provided by Monitored Drift Tubes (MDTs), except for the forward region, where Cathode Strip Chambers (CSCs) are used for the first layer due to their ability to sustain a higher rate.

The individual MDTs are cylindrical aluminum drift tubes of 30 mm diameter with a central tungsten-rhenium wire to collect ionization electrons. The average tracking resolution for a single tube is approximately 80 μm in the z-direction; this corresponds to a value of around 35 μm per chamber. There are a total of 1171 MDT chambers, corresponding to more than $3.5 \cdot 10^5$ tubes. The CSCs are multiwire proportional chambers which provide measurements with a resolution of 60 μm in the radial R-direction; there are $7 \cdot 10^4$ readout channels

The muon system is also part of the trigger system to trigger on particles within region $|\eta| < 2.4$, positioned around the middle and outer layers of the MDT chambers. The muon spectrometer is located at the very outside of the whole ATLAS detector. Muon with momenta down to

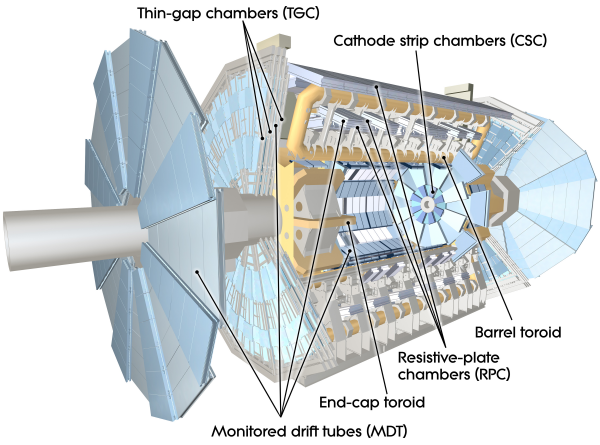

(a) A

Figure 3.8: The ATLAS Muon Spectrometer. Figure taken from [MOS23]

several GeV (3 GeV , due to energy loss in the calorimeters) could be measured alone by the muon spectrometer.

Resistive Plate Chambers (RPCs) are used in the barrel region, $|\eta| < 1.05$, and Thin Gap Chambers (TGCs) are used in the forward (endcap) region,$1.05 < |\eta| < 2.4$. The RPCs are gaseous parallel electrode-plate detectors which are positioned around the middle and outer layers of the MDTs. There are 3.8×10^5 RPC readout channels. The TGCs are arranged in four layers, three positioned around the second MDT wheel and the fourth in front of the CSC layer, with a total of 4.4×10^5 channels.

All the muon detention in this analysis is for the used information and technology used in the Run 2, which it is not longer in use for the new run. In the Run 3 an upgrade was done to some component like the Cathode Strip Chambers (CSCs) that were replaced for the New Samll Whell that it is implemented and working.

3.8 ATLAS trigger system

In the ATLAS experiment, we have a the nominal bunch collision rate at the LHC is approximately 40 MHz (1 collision every $25ns$). This rate goes beyond the capability to record in terms of the necessary recording speed and the available storage space. For these reasons, a specialized trigger system has been developed to identify events that contains the physical processes that we are interest in.

In Run 2, ATLAS used a two-level trigger system: the hardware-based Level 1 (L1) trigger and the software-based High-Level Trigger (HLT), a more detail explanation of the system can be found in [gro16]. A schematic of the ATLAS Trigger and Data Acquisition system is shown in Figure 3.9. An event is saved only if it passes both the L1 and HLT selection requirements [†].

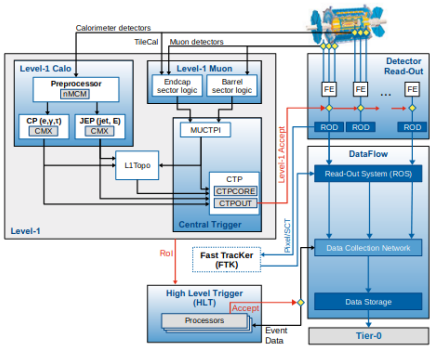

Figure 3.9: This is a schematic view of the ATLAS Trigger and Data Acquisition system in Run 2

The accepted events are processed by the HLT with a more accurate estimation of position and energy. The first step in the HLT tau reconstruction chain, the calorimeter-only preselection, is based on clustering the calorimeter energy deposits assigned to the L1 tau candidate. Afterwards, a cut in its energy, as described later in this report. Using a fast-track reconstruction algorithm, the tau candidate is assigned tracks in a core and an isolation region surrounding it. The tau-lepton candidate is required to have 1 to 3 core tracks and less than 2 isolation tracks. The latest tau-triggers additionally accept tau candidates without any core tracks. Afterwards, the track reconstruction is improved with a more efficient algorithm based on the one used offline, and the track multiplicity cuts are re-applied. Finally, the tau identification detail is later used to select the accepted tau-lepton candidate events [EC21b].

[†] [gro16]

Chapter 4

Object Reconstruction and Identification

When particles go through different sub-detectors in the ATLAS detector, the trigger and data processing system of ATLAS will process and record these signals. The data is saved in different pieces, categorized by different sub-detectors. Physicist can not use the data at this stage for data analysis as it has to go through further processing. The data used for physics analysis has to be object-based which means physicists have to transform and combine the information from different sub-detectors to the information (information of vertex, track, momentum or energy, etc) of different types of particles. This process is called **object reconstruction** and **identification**. Tracks are reconstructed in the inner detector and the muon spectrometer, while clusters of energy deposits are identified in the calorimeter systems.

Reconstruction is the process, which combines all the data in different sub-detector of ATLAS to get information about the vertex, track, momentum and energy information associated to certain particles. Only object reconstruction is not enough. Furthermore, we also need to identify what kind of particles are associated with the reconstructed information. This process is called **object identification**. **Object reconstruction** and **identification** play important role in physics data analysis because they are the step of converting the electric signals and data to physical objects which could be directly used by physicists. On the other hand, the **reconstruction** and **identification** are usually associated with significant systematic uncertainties, which will affect the sensitivity of data analysis. So getting an idea about how the reconstruction and identification work are quite critical.

In the $b\bar{b}\tau^+\tau^-$ analysis, with the process said before, this information is then combined to reconstruct and identify particles like electrons, muons, photons, jets and τ-leptons, and to measure properties of the event such as the missing transverse energy. Discussion on the procedures of reconstructing and identifying these specific types of objects. As we further require some of the jets to be b-tagged, the b-tagging and overlap removal algorithms are also discussed within this chapters as well.

The signatures of different particles in the ATLAS detector are shown in Figure 4.1. The algorithms used in ATLAS to reconstruct and identify particles which are relevant for this thesis are described in this chapter.

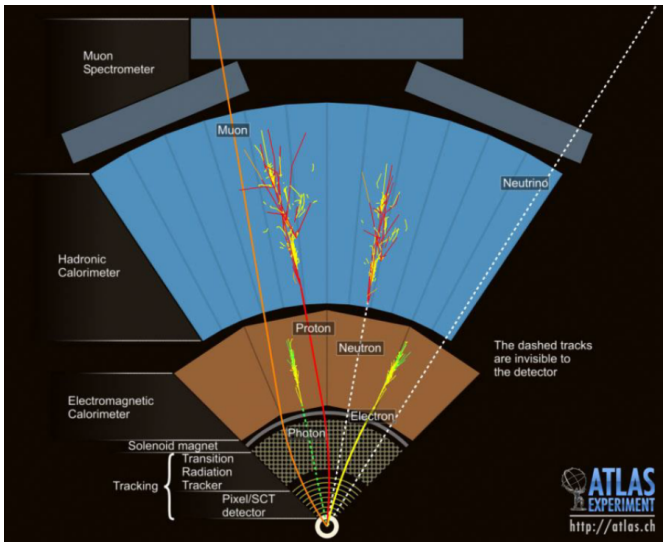

Figure 4.1: Overview of the signatures of different particles in the ATLAS detector [Peq08]

4.1 Track and vertex reconstruction

The reconstruction of charged particle tracks starts from hits in the inner detector. When traversing the inner detector, particles describe an approximately helical path, due to the influence of the homogeneous magnetic field, and leave hits by interacting with the various detector components that they traverse. The particle tracks are reconstructed from these hits using dedicated algorithms known as tracking algorithms. The track reconstruction process consists of two steps: pattern recognition and track finding, followed by track fitting. A detailed description of the ATLAS tracking is given in Reference [Col17b].

The main tracking algorithm is called "inside-out" tracking and begins in the first layers of the inner detector. The reconstruction starts from assembling clusters of hits in the pixel and SCT detectors. From these clusters, three-dimensional measurements referred to as space-points are created. They represent the point where the charged particle traversed the active material of the ID. Track seeds are formed from sets of three space-points and then a combinatorial Kalman filter is used to build track candidates from the seeds, by including additional space-points from the remaining layers of the pixel and SCT detectors and updating the track parameters. As next step, ambiguity needs to be resolved, since several track candidates could share the same hits. In order to do this, the track is refitted with a χ^2 fit and a score is assigned to each track, based on the fit quality, the number of hits of the track, the presence of overlapping hits or "holes" (missing hits) and the track pT. Then, ambiguities are solved by choosing the track with the largest score. The tracks are then extended into the TRT and, by using the full information of the three detectors, they are fitted once again with a high-resolution fit to extract the final track parameters.

A complementary tracking procedure, the "outside-in" tracking, is used to reconstruct the tracks that do not produce hits in the first layers of the inner detector, such as tracks coming from photon conversion or from the decays of long-lived particles. This tracking algorithm follows an analogous procedure to the "inside-out" tracking but starting from the TRT hits and working inwards.

After tracks are reconstructed, interaction vertices can be reconstructed [87]. The reconstruction of primary vertices is organised in two steps: the primary vertex finding algorithm, dedicated to associate reconstructed tracks to the vertex candidates, and the vertex fitting algorithm, dedicated to reconstruct the vertex position. The reconstrucred tracks are used to find a vertex seed from their crossing point and the vertex position is determined using an adaptive vertex fitting algorithm [88], which takes as input the seed position and the tracks around it. Tracks incompatible with the vertex are used to seed a new vertex and the procedure is repeated until no unassociated tracks are left in the event or no additional vertex can be found. The primary vertex for each event is selected as the vertex with the highest $\sum_{tacks}(p_T^{track})^2$

4.2 Electron reconstruction and identification

Electrons in the central region of the detector ($|\eta| < 2.47$) are reconstructed and selected from tracks in the ID (inner detector) which are matched with energy deposits in the the EM calorimeter , track-to-cluster matching information and the quality of the track. Electron candidates are identified using a likelihood technique

The electron reconstruction procedure consists fitting a track using Inner Detector information and matching it to an energy cluster in the EM calorimeter [lis16]. Not all of the objects built by the electron reconstruction algorithms are prompt electrons which are considered signal objects. The algorithm divides the $\eta - \phi$ space into a grid of$N_\phi \times N_\eta = 200 \times 256$ elements (of size $\Delta\phi \times \Delta\eta = 0.025 \times 0.025$) and electron cluster seeds are searched as towers of$N_\phi \times N_\eta = 3 \times 5$ cells with total cluster transverse energy above 2.5 GeV. Finally, clusters are formed around the seeds using a clustering algorithm, as described in [LLL$^+$08]. that allows for duplicates to be removed. A track-matched cluster is identified as an electron candidate, to distinguish between electrons that leave a track in the inner detector and photons that do not.

Electron identification(ID) algorithms are then applied after the reconstruction in order to discriminate between prompt, isolated electron candidates(signal) from background-like objects.

Discriminating variables include the shape of the electromagnetic shower, the quality and length of the inner detector track and the track-calorimeter matching. Three levels of identification are provided for the electrons by cuts applied on the likelihood discriminator. The background-like objects could possibly come from photon conversions, hadron mis-identification and heavy flavor decays. Figure 4.2 shows how one electron is reconstructed and identified, as well as, the sub-detectors involved in the procedure. There are three levels of electron identification operating points typically provided for electron ID. These are referred as **Loose, Medium**, and **Tight**.

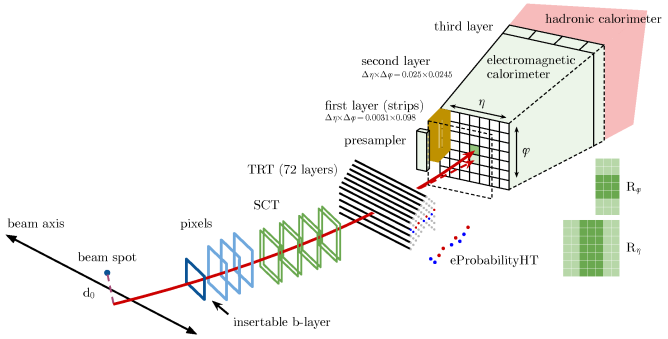

Figure 4.2: Schematic view of the electron reconstruction and identification procedure and the sub-detectors involved [lis16]

Tight operating point has the highest background rejection efficiency, while Loose working point has the lowest. The operating points are defined such that the set of electron candidates with higher background rejection is a subset of the electron candidates with lower background rejection ($Tight \subset Medium \subset Loose$). In other words, electrons passing Tight operating point will also pass Medium and Loose operating point, for instance.

For the analyses $HH \rightarrow b\bar{b}\tau^+\tau^-$ in this thesis, Loose working point is required for electrons to be passed in this analysis. The Loose working point with additional track hit requirement will provide an electron identification efficiency of 95%. Additionally, they are required to have $p_T = 7\ GeV$ and the four-momentum of the central electrons ($|\eta| \leq 2.47$) is computed using both the information in the final cluster and the track from inner detector best matched to the original seed cluster. Electron candidates in the barrel-endcap transition region of the Electromagnetic Calorimeter ($1.37 < |\eta| < 1.52$) are vetoed.

In order to further reject hadronic jets misidentified as electrons, the electrons are requaire to have a certain level of isolated from other particles in order to further reject background objects (including light hadrons misidentified as electrons, converted photons and electrons from hadron decays) by imposing the Loose isolation working point requirement. Two of the main isolation variables used are calorimeter-based isolation and track-based isolation. The isolation requires no near-by tracks or calorimeter energy deposits with in a variable size(p_T dependent). This isolation requirement could be inverted to provide control region for estimating background in the signal region.

When applying the electron tau triggers, the electron isolation working point is changed to 'tight' since the single electron trigger Scale Factors are not available for loose iso electrons.

4.3 Muons

Information primarily from the inner detector(ID) and muon spectrometer(MS), supplemented by information from the calorimeters, is used to identify and precisely reconstruct muons in ATLAS detector . Muon reconstruction is first performed independently in the inner detector and muon spectrometer. Then the information from individual sub-detectors is combined to form the muon tracks which will be used in physics analysis.

The muon spectrometer(MS) is the outermost sub-detectors on ATLAS. The goal of MS is to detect charged particles in the pseudorapidity region $|\eta| \leq 2.7$, and provide high momentum

resolution. The Resistive Plate chambers(RPC, three doublet layers for$|\eta| \leq 1.05$) together with the Thin Gap Chambers(TGC, three triplet and doublet layers for$1.0 \leq |\eta| \leq 2.4$) provide triggering and η, ϕ position measurements of muons. Precise muon momentum measurement is possible up to region $|\eta| = 2.7$ by three layers of Monitored Drift Tube Chambers(MDT). Each of the MDT chamber provide 6 to 8 η measurements along the muon track. The Cathode Strip Chambers(CSC) is installed in the inner layer instead of MDTs for region with $|\eta| \geq 2.0$ in the end cap region for muon momentum measurement. The single hit resolution in the bending plane for the MDT and the CSC is about 80 μm and 60 μm, respectively. Muon reconstruction in the MS starts with a search for hit pattern inside each muon chamber to form segments. The MDT segments are then reconstructed by performing a straight-line fit to the hits found in each layer. The coordinate orthogonal to the bending plane will be provided by the RPC or TGC hits. Segments in the CSC detectors are built using a separate combinational search in the η and ϕ detector plane. The muon track candidates are then built by fitting together hits from segments in different layers. The algorithm used a segment-seeded combinational search starting with the segments generated in the middle layers of the detector where more trigger hits are available. Four categories of reconstructed muons are defined, depending on the available information in the detector subsystems:

- Combined muons are formed using a re-fit of the hits from tracks in the MS and ID in the region $|\eta| \leq 2.5$. This category gives the best rejection of fake muons and has the best momentum resolution.
- Segment-tagged muons are tracks in the ID that are tagged as muons if, when extrapolated to the MS, they are matched with at least one track segment. Segmenttagged muons are reconstructed in the $|\eta| < 2.5$ region.
- Calorimeter-tagged muons are used in the region $|\eta| < 0.1$ which is only partially covered by the MS. A calorimeter-tagged muon is formed when a track in the ID matches with an appropriate energy deposit in the ECAL.
- Extrapolated muons are reconstructed based on tracks from the MS only, with a loose requirement that they originate from the IP. Extrapolated muons are used to extend the muon reconstruction range into the region $2.5 < |\eta| < 2.7$, which is not covered by the ID.

Muon identification is necessary to suppress background, of which the majority originates from charged hadron decays. These muons are often identifiable by a 'kink' in the reconstructed track, resulting in a poor fit quality of the track; there are several variables that provide good discrimination between signal and background muons and are used in the identification procedure, as detailed in . Four muon selection categories are provided: Loose, Medium, Tight and$High - p_T$. As well as requirements on variables associated with the muon tracks, these categories use different combinations of the muon types.

In the $HH \to b\bar{b}\tau^+\tau^-$ analysis presented in this thesis muons are required to have $pT < 7$ GeV and $|\eta| < 2.7$ and pass the Loose identification working point. The isolation cut is inverted in order to create background control regions. This criteria uses all four muon types. Further selection cuts are applied to signal muons based on the trigger used and a higher muon quality is required.. An isolation selection criterion, based on tracks reconstructed in the inner tracker, to select muon candidates is defined in the same way as for electrons. In the analysis presented in this thesis a loose track isolation is chosen also for muons, which has a 99% muon efficiency. In this analysis, muons reconstructed according to this definition are used in the $b\bar{b}\tau_{lep}\tau_{had}$ channel, where one τ-lepton decays leptonically into a muon and the other decays hadronically.

4.4 Jets

Quarks and gluons produced in particle interactions undergo parton shower, by the mechanisms of gluon radiation and gluon splitting into quark-antiquark pairs, and hadronisation, producing a collimated group of particles known as jets. The goal of the jet reconstruction is to combine those particles in a physics object describing the characteristics of the initial parton.

The jet reconstruction starts by forming clusters of energy deposit in the calorimeters performing

a three-dimensional topological clustering of individual calorimeter cell signals . The algorithm clusters the energy deposits into so called "topo-clusters" and combines their four-momenta. Then, jets are reconstructed in ATLAS using the anti-kt [CSS08a] clustering algorithm that sequentially combines topo-clusters into larger objects based on the momentum-weighted distance between clusters. the anti-kt algorithm is one of a number of jet-finding algorithms [Atk15], which uses topological clusters of energy deposits in calorimeter cells (known as topo-clusters) as input. These jets are known as calorimeter jets. Jets may also be reconstructed from tracks; these are known as track jets. Track jets are less ikely to originate from pile-up activity as only tracks originating from the primary vertex are used.

The jet clustering algorithms are among the main tools for analyzing data from hadronic collisions. We introduce distances d_{ij} between entities (particles, pseudojets) i and j and d_{iB} between the entity i and the beam (B) as showed in Eq. 4.1. Inside the equation, $\Delta R^2_{i,j} = (y_i - y_j)2 + (\phi_i - \phi_j)^2$, p_{tj} is the transverse momentum of the entity, y_i is the rapidity and ϕ_i is the azimuth of particle i. R is the usual radius parameter as 0.4 or 0.6. The parameter p is to govern the relative power of the energy versus geometrical scale. When $p = -1$, we refer it as the "anti-kt " jet-clustering algorithm.

$$d_{ij} = min(\vec{p}^2_{T,i}, \vec{p}^2_{T,j}) \cdot \frac{\Delta R^2_{i,j}}{\Delta R^2} \tag{4.1}$$

and

$$d_{i,beam} = \vec{p}^2_T \tag{4.2}$$

The sequential algorithms follow an iterative process:

- The two clusters with the minimum d_{ij} are combined into a single proto-jet.
- If the minimum value of d_{ij} is $d_{i,Beam}$, i.e. it is between a cluster and the beam line, the cluster is labelled as a jet and is removed from the list.
- The process continues until the separation between all clusters and proto-jets is $> R$, where R is the required jet radius.

After the jets are formed, the four-momentum of the jet, firstly computed simply from the sum of the four-momenta of the constituent objects, is corrected with the jet energy scale (JES) calibration [Col17a]. The jet energy scale (JES) calibration is a p_T- and $\eta-$dependent correction which ensures that the reconstructed jet energy matches that of simulated truth jets. The JES calibration accounts for: the differences in response of the hadronic and electromagnetic calorimeters; out-of-cone effects, i.e. the particles that were not reconstructed in the jet; leakage of particles outside the calorimeter; and energy loss in dead material. Also we have another algorthm the jet energy resolution (JER) [Col13b], is limited by the intrinsic resolution of the calorimeters and it ha to do with the residual spread along the corrections doing at this stage for jets. Systematic uncertainties related to the JES and JER are important sources of uncertainties in analyses with jets in the final state.

4.4.1 Bottom quarks

Bottom quarks, with a mass of approximately 4.18 GeV [18], form B-hadrons that have sufficiently long lifetime to travel some distance before decaying. This lifetime on the other hand is short enough so that they decay before reaching the inner detector.

b-jets

The identification of jets coming from b-quark hadronisation, the so-called b-tagging, is crucial for analyses looking for processes with one or more b-quarks in the final state, as the $HH \rightarrow b\bar{b}\tau^+\tau^-$ analysis presented in this thesis. Several algorithms to identify jets coming from b-hadrons decays have been developed, exploiting the lifetime, high mass and decay multiplicity of b-hadronsand the hard b-quark fragmentation function.

Due to sufficiently long lifetime of B-hadrons, there is a displacement of their decay (secondary) vertex with respect to the primary vertex (interaction point), which can be reconstructed through the extrapolation of charged particle tracks. The decay products of the B-meson further form jets. Then, the presence of a secondary vertex within these jets indicates a presence of a B hadron and they are referred to as b-jets. The identification of heavy-flavor jets is also based on some impact parameter information. As can be seen in Figure 4.6 (c), the transverse impact parameter, d_0 , of a track is the closest distance between the track and the primary vertex in the plane perpendicular to the direction of collision. The longitudinal impact parameter, L_0 , is the aforementioned closest distance in longitudinal direction. Similarly to hadronically decaying τ -leptons, b-jets are reconstructed using the anti-kt algorithm with a radius parameter R = 0.4. Then, they are identified using the MV2c10 multivariate discriminant, also based on BDTs [Col16b, ATL16]

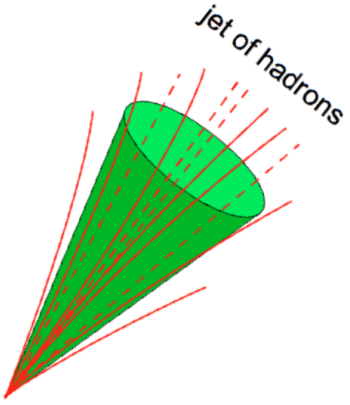

Figure 4.3: Typical signature of a QCD jet

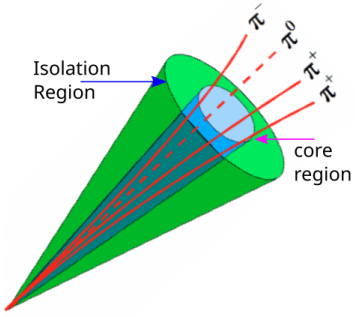

Figure 4.4: Typical signature of a hadronic tau decay.

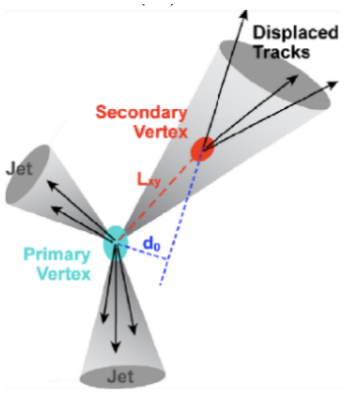

Figure 4.5: Diagram showing the principle of identification of jets initiated by b-hadron decays

Figure 4.6: Comparison of τ -jets and b-jets with regular jets

The identification of b-quark jets in ATLAS is based on distinct strategies used in three basic b-tagging algorithms: impact parameter-based algorithms, an inclusive secondary vertex reconstruction algorithm and a decay chain multi-vertex reconstruction algorithm. The input variables of these b-tagging algorithms are combined in a multivariate discriminant (called MV2) that is the final default algorithm used by ATLAS [ATL16, Col16a]. The ATLAS MV2 (multivariate tagger) is an algorithm based on a Boosted Decision Tree (BDT) which is trained on jets from simulated $t\bar{t}$events, with b-jets being considered as signal and c- and light-flavour jets being considered as background.

4.4.2 Missing transverse energy

The initial state of LHC collisions is well defined only in the transverse plane. Since the proton beams are aligned with the longitudinal axis and the transverse momenta that partons acquire inside the proton are negligible compared to the momentum of the proton, the transverse momentum in the initial state is zero. While the transverse momentum is known to be zero, the longitudinal momentum in a collision is unknown as it is $(x_1 - x_2) \times E_{beam}$, where the proton momentum fractions carried by the interacting partons, x_1 and x_2 , cannot be predicted neither measured. For this reason, momentum conservation can only be imposed in the transverse plane where the initial state is known and the final state can be measured. If neutrinos, or other unknown weekly interacting particles, leave the detector with non-zero transverse momenta, the missing transverse momentum can be reconstructed using the conservation of the momentum in the transverse plane. The "missing transverse momentum" is defined as:

$$\vec{p}_T^{miss} = \vec{p}_T^{final} - \vec{p}_T^{final} = -\vec{p}_T^{final} \tag{4.3}$$

so it is equal to the negative reconstructed or visible momentum vector in the final state. A good knowledge of all objects considered for the vectorial sum is required for its reconstruction. The quantity used in ATLAS is called E_T^{miss} is called the missing transverse energy, and this quantity account for the momentum imbalance in the plane transverse to the beam axis. Its measurement can allow the indirect detection of neutrinos. In this analysis, E_T^{miss} is defined as the magnitude of the negative vector sum of all reconstructed 4.4, calibrated objects for all particles except muons whose transverse momentum is directly measured in the muon spectrometer together with a track-based "soft" term (TST), which is reconstructed from the transverse momentum deposited in the detector, but not associated with any of the aforementioned identified objects [Lee15]

$$E_T^{miss} = -\sum_{jets} E_T - \sum_{photons} E_T^{\gamma} - \sum_{taus} E_T^{\tau} - \sum_{electrons} E_T^{e} - \sum_{muons} E_T^{\mu} - \sum_{soft} E_T^{soft} \tag{4.4}$$

The jet, charged lepton, photon terms are negative sum of the momenta for the respective calibrated objects. Calorimeter deposits are associated with reconstructed objects in the following order: electrons(e), photons(γ),hadronically decayed τ , jets and muons(μ). The soft term in the equation is reconstructed from the transverse momentum deposited in the detector without being associated with any reconstructed hard objects(The objects mentioned before.) This term could either be reconstructed using calorimeter-based methods or track-based methods.

4.4.3 Tau leptons

In this study we would be focusing our attention to the lepton-tau decay, becuase it's a final state of the $hh \to bb\tau_{lep}\tau_{had}$. We will investigate the $\tau_{lep}\tau_{had}$ channel. So in order to understand this we need to know a little bit of the τ lepton. The τ lepton is the heaviest lepton with a mass of 1.777 GeV. In 35% of the cases it decays leptonically into a lighter lepton, either an electron (e) or a muon (μ), and neutrinos (ν), while it decays to hadrons and a neutrino in the remaining 65%: 11.5% to one charge hadron, 35.5% to one charge hadron and neutral hadrons and 15% to three charged hadrons and any number of neutral hadrons as e an see in the Figure 4.7. The mean life time of a τ lepton is $2.9 \cdot 10^{-13}$ s, thus, for a momentum of few tens of GeV, it can travel few millimeters before decaying. Most of the times, it decays before reaching the innermost sensitive detector layer, therefore only its decay products are observed. These neutral and charged hadrons from τ decays are the visible decay products of the τ leptons and will be referred as $uptau_{had-vis}$.

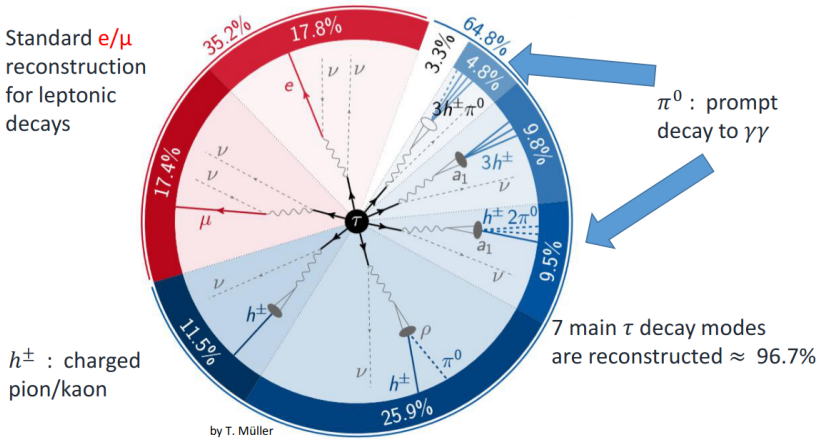

Figure 4.7: Tau decays: In red we have the leptonic decays and in blue we have the hadronic decays

The τ lepstons are the only leptons heavy enough to decay both in lighter leptons and hadrons. As can be seen in the Feynman diagram of Figure 4.8, the $\tau-$lepton decays into a neutrino ν_τ and an off-shell W boson, where the W boson further decays into either $l\nu_l$, where l is electron

or muon, or two quarks. The former case is referred to as the leptonic decay mode and the latter as hadronic. The leptonic decay mode has a branching fraction of around 35% (red arc in Figure 4.7), while the hadronic decay mode is more common with a branching fraction of around 65% (blue band in Figure 4.7). As for leptonically decayed τs, we identify their direct decay product, electrons or muons, and process together with the reconstructed hadronic τs when reconstructing the $di-\tau$ invariant mass using MMC

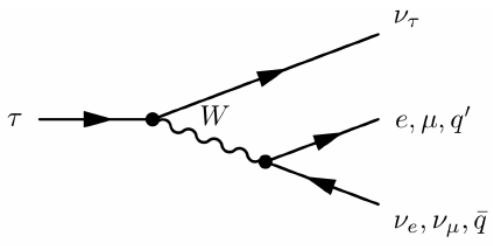

Figure 4.8: Feynman diagram of $\tau-$lepton decays by an emission of an off-shell W boson.

Hadronic $\tau-$leptons

Hadronically decaying $\tau-$leptons, τ_{had} , usually create final states of one or three charged pions $\pi^{\pm}$ and some number of π^0. Depending on the number of charged tracks left in the inner detector, the hadronically decaying $\tau-$leptons are referred to as 1-prong or 3-prong if they decay in one or three charged pions respectively as we can see in figure 4.1. Among the hadronic τ decay, one or three charged pions are presented with branching ratio equal to 72% and 22% respectively. The rest 6% of hadronic τ decays are with charged kaons presented mostly. The most common 1-prong final state is $\tau \to \pi^-\pi^0\nu_\tau$ as we can aprociate in the following table.

Decay Mode	Branching Fraction (%)
1-prong	
$\tau^{\pm} \to \pi^{\pm}\nu_\tau$	10.82
$\tau^{\pm} \to \pi^{\pm}\pi^0\nu_\tau$	25.49
$\tau^{\pm} \to \pi^{\pm}2\pi^0\nu_\tau$	9.26
$\tau^{\pm} \to \pi^{\pm}3\pi^0\nu_\tau$	1.04
3-prong	
$\tau^{\pm} \to 2\pi^{\pm}\pi^{\mp}\nu_\tau$	8.99
$\tau^{\pm} \to 2\pi^{\pm}\pi^{\mp}\pi^0\nu_\tau$	2.74
$\tau^{\pm} \to K^{\pm}\pi^{\pm}\pi^{\mp}\nu_\tau$ + *neutral particles*	0.33

Table 4.1: The predominant hadronic tau decay modes and their branching fractions, taken from [Pat16]

The τ_{had} form jets as well as the main background which is from jets of energetic hadrons produced via fragmentation of quarks and gluons. The most essential difference is that τ_{had} has a more narrow, collimated shape and lower charged track multiplicity (one or three tracks) in the inner detector. QCD-induced jets, in general, have a wider shape with more particles, which among other characteristics, is used to discriminate τ decays from other jets, as shown in Figure 4.6. This kind of background is already presented at the trigger level, which we also refer as online level. An electron or a muon could also be misidentified as hadronically decayed τ with leptons misidentified as the charged hadron from τ decay. Information from the narrow shower shape, the distinct number of charged particle tracks and the displaced τ lepton decay vertex are used for both online and offline event reconstruction. The $\tau_{had-vis}$ reconstruction is seeded by the energy deposits which have been constructed as individual jet in the calorimeter. The jets are formed using the anti-kT algorithm which was presented in the jets reconstruction section with distance parameter$R = 0.4$ and calibrated using a local hadronic calibration(LC). These jets are used as seeds for the reconstruction of visible products of hadronically decaying $\tau-$leptons, $\tau_{had-vis}$, which are required to have one or three tracks. Boosted decision trees (BDTs)5 [H$^+$07] are trained in order to distinguish $\tau_{had-vis}$ candidates from QCD-induced jets.

4.5 Qualification Task

4.5.1 The Tag-and-Probe Method for Tau Lepton Efficiency Measurements

In this section, the performance of the ATLAS tau trigger is evaluated by employing a tag-and-probe analysis using a sample enriched in $Z \to \tau\tau \to\to \mu\tau_{had-vis}3\nu$ events for one signal region (Other region later consider is is one enriched in $t\bar{t} \to [b\mu\nu][b\tau_{had-vis}2\nu]$ events, but this space from the scope pf this analysis). In the first case (Z signal region) one tau decays leptonically into a muon and the second tau decays hadronically. In both signal region. The tag-and-probe analysis is done by selecting events triggered by the presence of a muon (the tag), and a hadronically decaying tau lepton candidate (the probe) in the final state, which is reconstructed offline. Preselection requirements are placed on both the muon tag and the hadronically tau decays as the probe, as the Table 4.3 shows.

The signal region is explained, along with the control regions used to model the background contributions.

where

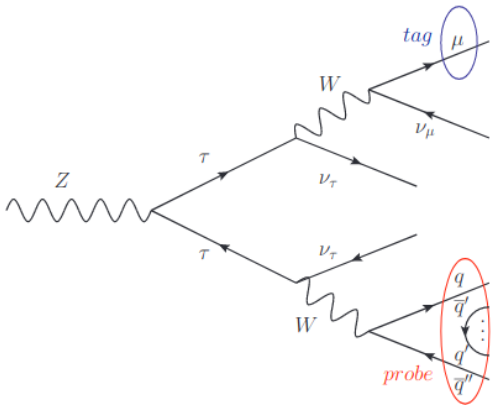

Figure 4.9: The $Z \to \tau\tau \to \mu\tau_{had-vis}3\nu$ decay

4.6 Data and simulation samples

In order to calculate the efficiency of the Trigger, we studied the analysis developed for the $Z \to \tau_{lep}\tau_{had}$ process. The data used to compute the efficiencies was taken between years 2015 and 2018, with $\sqrt{s} = 13$ [TeV]. Signal and background processes relevant for the tag and probe method can be seen in the following Table. 4.2

background contribution	generators	PDF set	Non pert.
$W/Z + jets$ (MC)	POWHEG-BOX v2	CT10	Pythia8+AZNLO+CTEQ6L1 [26–28]
$t\bar{t}$, single top W t-and s-channel (MC)	POWHEG-BOX v2	CT10	Pythia6+P2012+CTEQ6L1 [33, 34]
single top t-channel (MC)	POWHEG-BOX v1	CT10f4	Pythia6+P2012+CTEQ6L1
multi-jets (data-driven)	-	-	-

Table 4.2: These are the software used for the simulation of the samples, also the corresponding PDF set used for the specific process. And the modelling of non-perturbative effects (Non pert.) such as the parton shower with the corresponding MC tune and PDF used.

4.6.1 Tag and Probe Preselection

The requirement for the tag muon is $|\eta| < 2.5$ and to pass calorimeter and track isolation requirements. The muon transverse momentum must be at least 2 GeV higher than that

required by the muon trigger; which means will depend on the period in which it was selected , so the momentum can be 26 GeV in the first 6.1 fb^{-1} and 28 GeV in the remaining 27.1 fb^{-1}

The $\tau_{had-vis}$ probe is require to have $p_T > 25GeV$, $|\eta| < 2.5$ (excluding the region $1.37 < |\eta| < 1.52$), and one or three core tracks, we can see this in the schematic Figure: 4.10

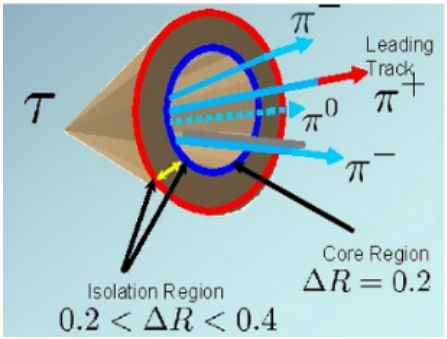

Figure 4.10: Representation Isolation Criteria.

and electric charge opposite to the charge of the muon. The tau probe also required to satisfy the medium identification criterion of the RNN discriminant against jets.

4.7 Object and Event Selection

The object reconstruction include muons, electrons, jets and tau candidates. For muons these are reconstructed in the ID and MS, independently, then the information from the sub-detectors is combined and used in physic analysis. A specific explanation about the muon reconstruction and the algorithms used can be found at [AAA+16].

Electron samples from $Z \to ee$ are required to have $p_T > 10$ GeV and electron leptons are reconstructed by matching clustered energy in the EM calorimeter with ID reconstructed tracks which have to satisfy a transverse momentum $p_T > 15$ GeV and $|\eta| < 2.47$. Electrons are identified using signal and background probability density functions detailed in [lis16] with a likelihood function (LLH) as described in [hue17].

For both, electrons and muons, the sum of transverse momentum in a variable size cone $\Delta R < min[10GeV/p_T, 0.3]$ centred on the lepton candidate, but excluding the lepton track itself which needs to be less than a fraction of the lepton transverse momentum. Additionally the sum of the cluster energy in the calorimeter within a cone of size $\Delta R < 0.2$ around the lepton, must be less than a fraction of lepton energy mentioned before. Both conditions are dependant of the lepton transverse momentum.

In the case of jets these are reconstructed using the anti-k_t [CSS08b], which use as inputs the information of *TopoCluster* and a distance parameter o $R = 0.4$. Also the pseudo-rapidity requirement for jets requires to be $|\eta| < 4.5$. The algorithm used to identified the jets from the b-quark in $|\eta| < 2.5$ is the b-tagging algorithm and is described [20116].

Event Selection

As indicated in on Table 4.3 we can see the different cuts for the signal regions and the the purity of $Z \to \tau\tau$ signal region can be enhanced with further requirements on the selected tag-probe pair. In order to reduce contamination by $W(\to \mu\nu)+$ jets events, a series of requirements are made on the transverse mass and $\Sigma cos\Delta\phi$ variables attributed to the tag and probe pair in the signal region. The transverse mass.

$$m_T(\mu, E_T^{miss}) = \sqrt{2p_T^{\mu} E_T^{miss}(1 - cos\Delta\phi\mu, E_T^{miss})} < 50 \tag{4.5}$$

Event preselection	
Muon tag:	$\tau_{had-vis}$ probes
Medium quality Trigger-matched momentum cut: $p_T > 26/28\ GeV$ pseudo-rapidity: $\|\eta\| < 2.5$ track+calo isolation	jet BDT medium Muon veto no overlapping electron $p_T > 25\ GeV$, $\|q\| = 1$ $\|\eta\| < 1.37, 1.52 < \|\eta\| < 2.47$ 1 or 3 core tracks
Tag-probe pair selection	
muon and $\tau_{had-vis}$ with opposite electric charge No other muon or electron	
$Z \to \tau\tau \to \mu\tau_{had-vis}3\nu$	
$m_T(\mu, E_T^{miss}) < 50\ GeV$ $\Sigma cos\Delta\phi > -0.5$ $45\ GeV < m_{vis}(\tau_{had-vis}, \mu) < 80\ GeV$	
$t\bar{r} \to [b\mu\nu][b\tau_{had-vis}2\nu$	
$m_T(\mu, E_T^{miss}) < 50\ GeV$ At least 2 jets At least 2 b-tagging jets	

Table 4.3: Event pres-election and selection for Muon Tag and Tau Probe. And the requirement for the Signal region of the Z and Top processes

is required to be less than 50 GeV, and the sum of the azimuthal angles of the muon and the $\tau_{had-vis}$ with the missing energy, defined as:

$$\Sigma cos\Delta\phi = cos\Delta\phi(\tau_{had-vis}, E_T^{miss}) + cos\Delta\phi(\mu, E_T^{miss}) > -0.5 \tag{4.6}$$

must be greater than -0.5. The Σ cos $\Delta\phi$ variable plays a key role in the determination of the $W(\to \mu\nu + jets)$ background.

and the visible invariant mass

$$45GeV < m_{vis}(\tau_{had-vis}, \mu) < 90GeV. \tag{4.7}$$

All the control regions have an additional cut related to the τ reconstruction. As we can see in Table 4.4, the cuts are very similar between the signal and the control regions, therefore we need to study the control regions to cross-check and corroborate that we are estimating the background correctly. In order to do that we see the selection on the p_T for the different control regions and study that corresponding control regions are enriched in their corresponding selection as we can see in Figure:4.7.

Background estimation control regions
r_{QCD} control region
Inverted muon gradient isolation $m_T(\mu, E_T^{miss}) < 50\ GeV$ $\Sigma cos\Delta\phi > -0.5$
$k_W^{OS(SS)}$ control region
Muon gradient Isolation GeV $m_T(\mu, E_T^{miss}) > 60\ GeV$ $E_T^{miss} > 30\ GeV$

Table 4.4: Table: Summary of the control region selections used in background estimation

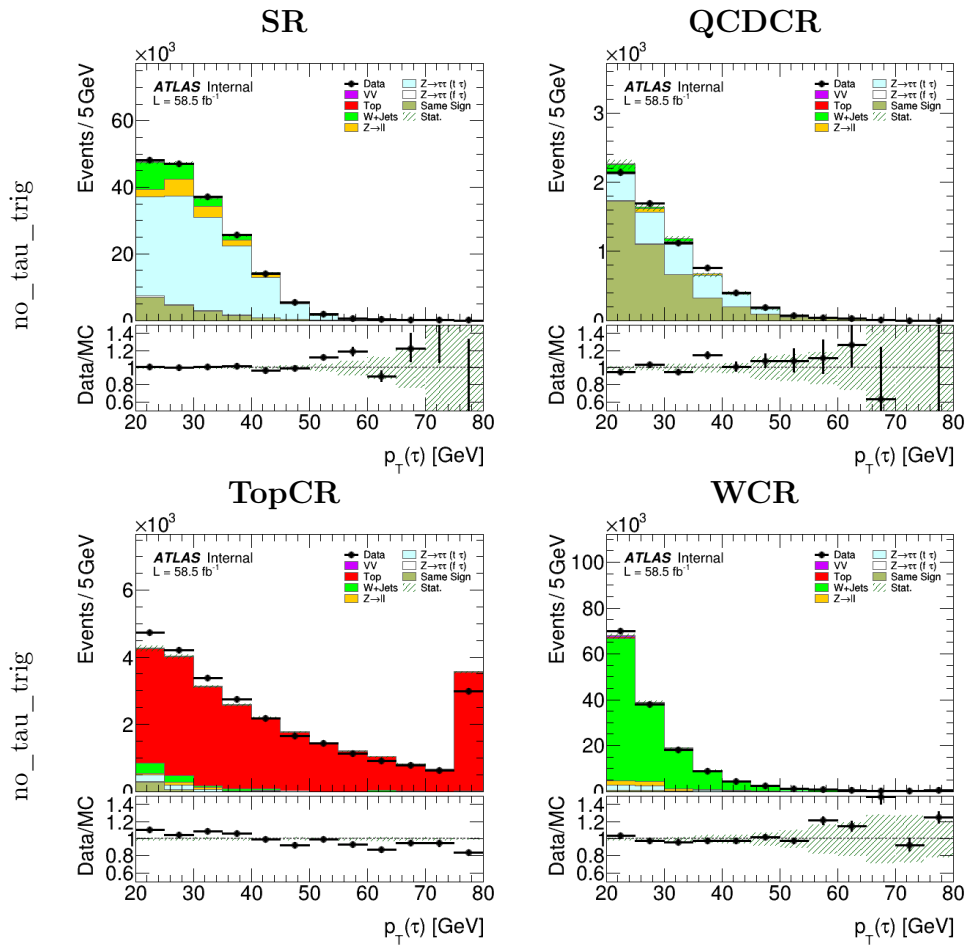

Table 4.5: Control Region Distribution Year 18. With a signal region define for $Z \to \tau\tau$

4.8 Tag and probe method

The *tag and probe method* relies on the preparation of an unbiased sample of physics objects, the probe objects, which are used to calculate efficiencies and resolutions. This method does not apply the nominal selection criteria, but asks for one triggered muon with high transverse momentum, p_T , reconstructed in the Inner Detector (ID) and Muon Spectrometer as a high quality track. This muon is selected by the lowest un-prescaled single-muon trigger available in each data period, and an offline reconstructed $\tau_{had-vis}$ candidate, as the probe.

While QCD jets contain a larger number of tracks coming from charged hadrons Figure 4.11. The τ_{had} decays mainly into one or three charged pions, some neutral pions and a neutrino Figure 4.12. Therefore a typical τ_{had} signature consists of one or three tracks (called one-prong and multi-prong) in the inner detector which form a narrow collimated jet inside the calorimeter. Compared to QCD jets almost no energy is deposited in the calorimeter cells around this inner cone. Thus an isolation requirement can be added as we can see in Figure 4.10 to distinguish the real τ_{had} signal from the QCD background.

The Reference [ATL15], [20115] explains the reconstruction and identification of $\tau_{had-vis}$ candidates.

The Trigger efficiency is the ratio of the number of triggered probe tau particles and the total number of muon (tag). Since the event is kinematically correlated we got limitations for the transverse momenta which gives a threshold on the momentum of the particle.

The amount of background from jets and hadrons contribution product of QCD confinement present in the data sample needs to be suppressed by the implementation of requirements in

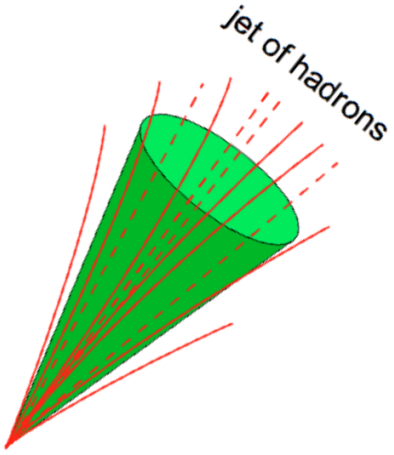

Figure 4.11: Representation of the signature of a QCD jet.

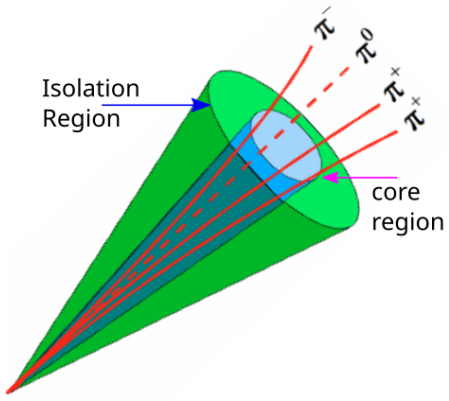

Figure 4.12: Representation of the signature of a hadronic tau decay.

the selection of tau candidates

4.9 $Z \to \tau_\mu \tau_{had}$ tag-and-probe analyses

The tag-and-probe method offers an elegant way to estimate trigger efficiencies with only minor statistical uncertainties and without a bias. Events are selected which are compatible with a well-known physics process that features two objects of the same type. The performance of the trigger in this analysis is measured with a data sample enriched in $Z \to \tau_\mu \tau_{had}$ events. To select the events the tag-and-probe approach is used, where the selection is triggered by the presence of a muon (tag) and containing a hadronically decaying tau lepton candidate (probe). The tag muon has been selected, using the trigger, and in general it has to pass tight selection criteria. The Probe that in this analysis correspond to an hadronically decaying tau lepton, should be with pass very loose selection criteria. Then the efficiency is given by the fraction of probe muons that pass a given criteria over the tag+probe sample.

$$\varepsilon = \frac{\textbf{tag muons}}{\textbf{tag+probe pairs}} \tag{4.8}$$

4.9.1 Common event selection

To select $Z \to \tau_\mu \tau_{had}$ events the following cuts are used:

- Single muon-trigger with threshold of $p_T > 27$ GeV for the Online and $p_T > 27.3 GeV$ for the offline, which needs to be geometrically matched to the online muon.
- No additional electrons or muons
- At least one $\tau_{had-vis}$ candidate with 1 or 3 tracks. If more, only the leading p_T is considered.
- Loose requirement on the tau identification.
- Muon and τ_{had} candidates require to have opposite-sign electric charge
- b-tagged jets are rejected to reduce top quark backgrounds

4.9.2 Monte Carlo Samples and Background Modeling: Methodology

The main background contributions to the $Z \to \tau\tau$ signal are QCD multi-jet events and $W(\to \mu\nu) + jets$, with the jet passing for a $\tau_{had-vis}$ candidate. Additionally, smaller contributions originate from top and Z + jets events.

The full estimate of the background in the opposite-sign signal region (SR) is written as

$$N_{OS}^{fake} = r_{QCD} Data_{SS} + W_{\mu\nu}^{OS-SS} + Z_{\mu\mu}^{OS-SS} + top^{OS-SS} \tag{4.9}$$

The method exploits charge asymmetry by determining the charge symmetric ($Q_\tau \times Q_\mu > 0$) and charge asymmetric ($Q_\tau \times Q_\mu < 0$) components of the background independently. The charge-asymmetric component of a given background is estimated in the relevant opposite-sign

The factors r_{QCD} and $k^{OS/SS}$ that goes with the background estimations, are define as follow:

Fake rate correction factor k_W

The k_W correction factors account for a possible mismodelling of the $j \to \tau$ fake rate in simulation. They are calculated separately for OS and SS events in a control region designed to be enriched in W + jets events using the cuts $mT(\mu, E_T^{miss}) > 60\ GeV$ and $E_T^{miss} > 30 GeV$. The kW factor is then the ratio of the observed to expected events in this region:

$$k_W^{OS/SS} = \frac{Data - OtherMC}{WMC} \tag{4.10}$$

correction factor r_{QCD}

The r_{QCD} correction factor is thus applied due that the OS/SS symmetry is assumed to not be perfect, as the insufficiency of anti-particles in the initial protons introduces a bias to positively charged events. $rQCD$ is estimated as the ratio between OS and SS events in a control region designed to be enriched in QCD multi-jet events by inverting the muon isolation requirement since any non-isolated muons are expected to be produced in QCD jets.

$$r_{QCD} = \frac{(Data - MC)_{OS}}{(Data - MC)_{SS}} \tag{4.11}$$

These factors help us to correct the normalization. These are derived separately for high p_T ($> 40 GeV$) and low p_T ($< 40 GeV$) tau candidates, as well as $1 - track$ and $3 - track$ tau candidates. The factors consider the difference in the number of events between the MC and the data for example. And thus one can scale the normalization correctly. The factors also help to correct the difference in normalization between the same sign multi-jet events and the opposite sign ones, the template is scaled by the ratio r_{QCD} of OS/SS multi-jet events

This equation helps us to calculate the templates for the signal and the background and it will help us to tell how the tau identification efficiency is measured. But to reduce contamination for example in the multi-jet control region, contamination that comes from $Z \to \tau\tau$ signal. One has to ask for: events with

$$45 GeV < m_{vis}(l, \tau_{had-vis}) < 80 GeV$$

So this means addition requirements need to be applied to reduce contamination in the signal and control regions.

The efficiency ϵ is defined as:

$$\epsilon = \frac{\#\text{ event with ID\&Trigger}}{\#\text{event with ID}}$$

And the efficiencies are used to calculate scale factors.

$$SF = \frac{\epsilon(\text{Data - MC})}{\epsilon(MC)}$$

4.10 Tau Trigger: Efficiency and Scale Factor Measurements

4.11 SIF software

Now we will see the distribution for different variables: Momentum p_T, visible mass $mviss - mass$ and $\eta(\tau)$. And the corresponding triggers according to the year. The Table 4.6 show us the list of triggers used for the Z and Top processes.

4.11.1 Software execution & results

The execution of the SIF repo with the respective trigger combinations, years and prongness were:

Triggers use for $Z/Top \to \tau\tau$		
Trigger	Years	Progn
`tau25_medium1_tracktwo`*	Full Run 2	1p & 3p
`tau35_medium1_tracktwo`*	Full Run 2	1p & 3p
`tau50_medium1_tracktwo`*	Full Run 2	1p & 3p
`tau25_medium1_tracktwoEF`	2018	1p & 3p
`tau35_medium1_tracktwoEF`	2018	1p & 3p
`tau60_medium1_tracktwo[EF]`†	Full Run 2 [2018]	1p & 3p
`tau80_medium1_tracktwo[EF]_L1TAU60`*	Full Run 2 [2018]	1p & 3p
`tau160_medium1_tracktwo[EF]_L1TAU100`*	Full Run 2 [2018]	1p & 3p

Table 4.6: Table: Triggers according their period

For all† of these combinations we focused on the Signal Region (SR) and used the three working points (loose, medium, tight). The plots obtained for the rest of the year can be found . Now we look into the nominal plots , which do not include the scale factor corrections, as well as the efficiencies we obtain for this.

4.11.2 Z Plots: Year 2015-2016-2017

These plots correspond to the momentum distribution for the nominal result. We have not included the corrections of the scale factors yet. With this we can see clearly that our definitions and cut select correctly the process coming from Z and Top Signal Region, but we have some miss modeling that has to be corrected and we will.

We can notice that the triggers cut are filtering the events as expected, but also we can see the efficiency and miss modeling increase with the trigger and progness. The three prong selection has a greater miss modeling.

†This trigger only works for Top process in the All years but 2018

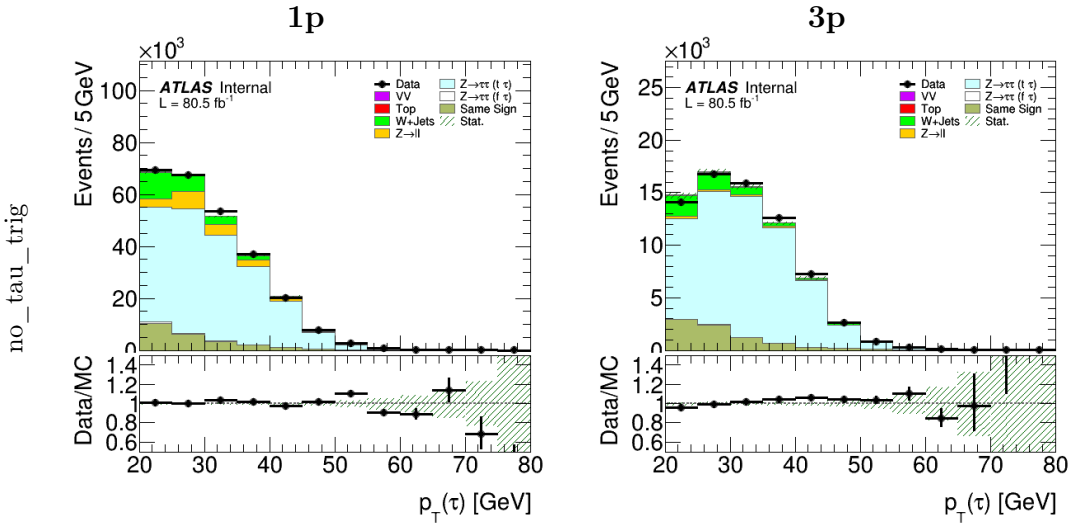

Table 4.7: $Z \to \tau\tau$ Momentum Distribution Year 17.

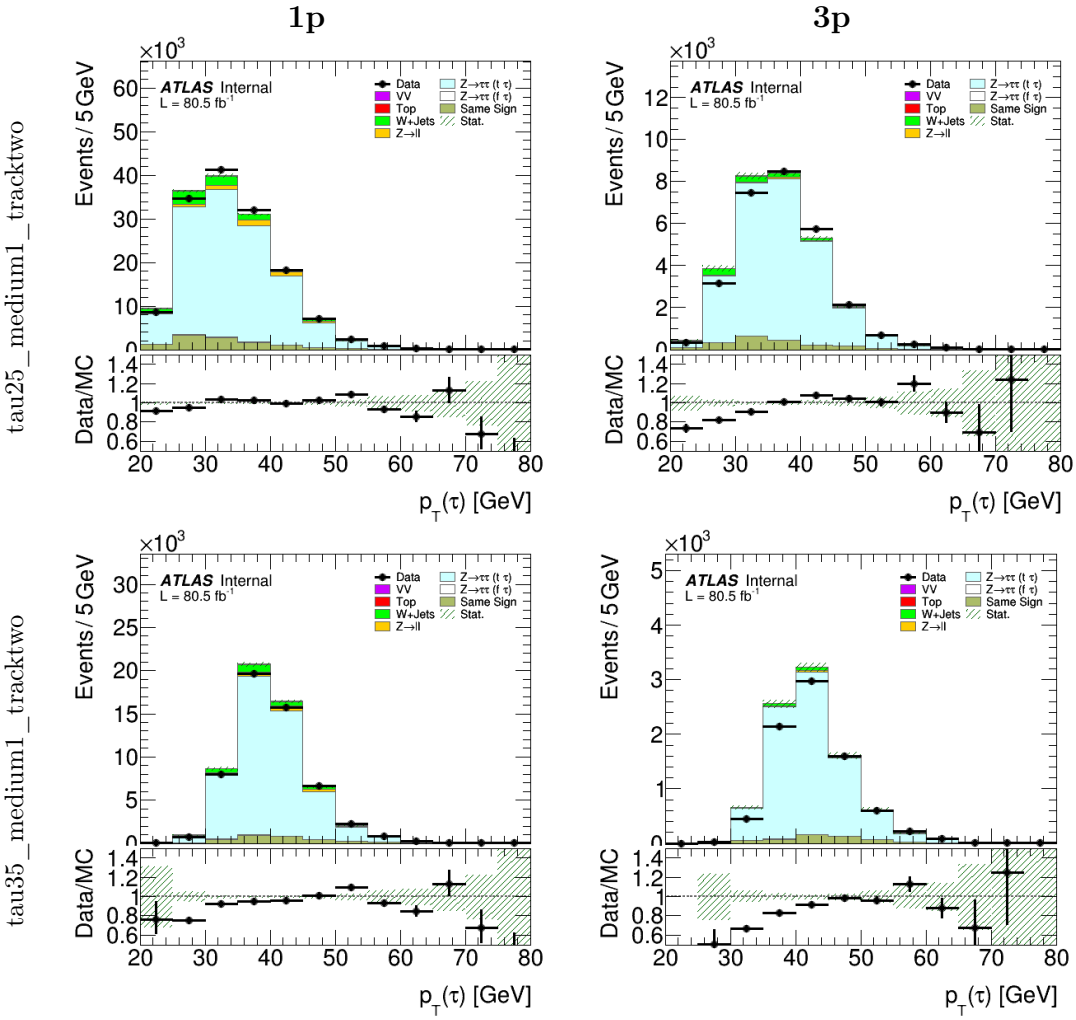

Table 4.8: $Z \to \tau\tau$ Momentum Distribution Year 17.

4.11.3 Scale Factors

This section presents the results of the tau trigger efficiency measurements. Discrepancies between the tau trigger efficiencies obtained with data and MC are accounted for using correction

factors that can then be provided along with the efficiencies themselves, in this case we are using the tau leptons. When we consider the MC processes, every event is scaled via scale factors depending on physical quantities, such as tau p_T (energy) , η (position), RNN working points, and many others.

Efficiency Plots and Scale Factor table: $Z \to \tau\tau$ SR

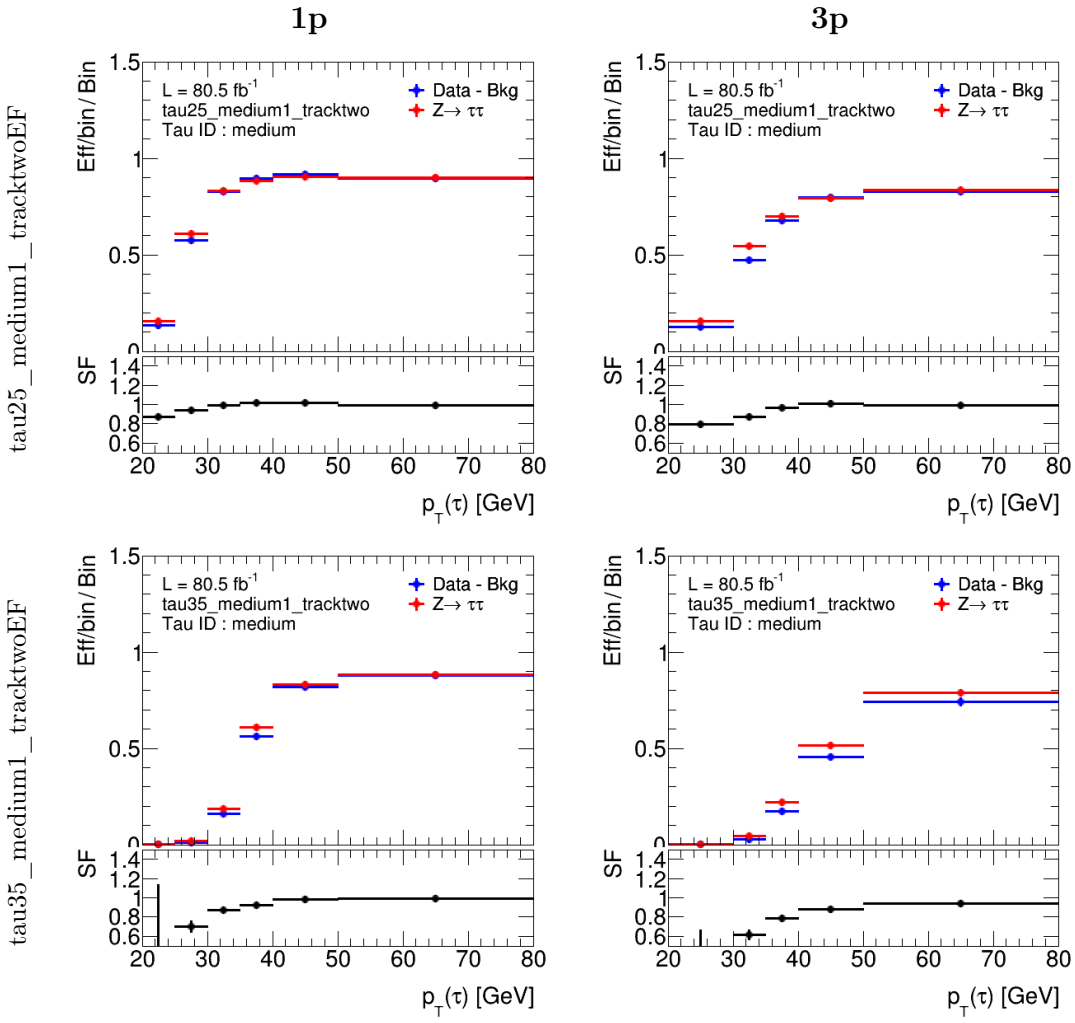

Table 4.9: These are the efficiencies plots of the tau25_medium_tracktwo trigger in the first row for 1 and 3 prongs and the tau35_medium_tracktwo in the second row. Both as a function of the p_T of the offline $\tau_{had-vis}$ probe selected in $Z \to \mu\tau_{had-vis}3\nu$ events.

4.11.4 Systematic Uncertainties

In this section, we introduce the systematic uncertainties, which affect our measurement. In general we can subdivided into three main categories: theoretical uncertainties in signal, theoretical uncertainties in background, and experimental uncertainties. But in our analysis we will be focusing on the experimental uncertainties.

The experimental uncertainties are related to the simulation of the detector response and to the measurement of background contributions from CRs. A non-negligible source of the systematic uncertainty in this measurement is the MC statistical uncertainty, as the simulated samples are of limited size.

The experimental uncertainties that are used in this analysis are the ones that recommended by combined performance groups and making use of the AnalysisBase-21.2.119. The systematics uncertainties considered for each object reconstructed will be listed below . As an example we have the b-taggin that we will explain.

4.11.5 Experimental uncertainties

The experimental uncertainties cover empirical uncertainties in object reconstruction and calibration and also the confidence to which the simulated detector response is able to reproduce experimental data for the reconstructed objects.

Z Scale Factors

Now let us see the values of these systematic's uncertainties and then the impact that this corrections factions will have .

Trig : $tau25\_medium1\_tracktwo - 1p$				
Process	Tau pt	SF	Stat	Syst
Z	20-25	0.872	± 0.028	± 0.409
Z	25-30	0.940	± 0.009	± 0.045
Z	30-35	0.996	± 0.005	± 0.047
Z	35-40	1.014	± 0.005	± 0.016
Z	40-50	1.016	± 0.005	± 0.038
Z	50-80	0.993	± 0.015	± 0.057

Trig : $tau25\_medium1\_tracktwo - 3p$				
tau pt	Tau pt	SF	Stat	Syst
Z	20-30	0.795	± 0.038	± 0.153
Z	30-35	0.868	± 0.016	± 0.049
Z	35-40	0.967	± 0.013	± 0.022
Z	40-50	1.008	± 0.010	± 0.122
Z	50-80	0.994	± 0.030	± 0.182

This Trigger study is to detail the $Z \to \tau\tau$ trigger efficiency measurements using the Tag-and-Probe method. A significant portion was dedicated to reproduce and measure already obtain in the current implementation for the analysis. Later we implemented the new idea. Define a new signal region for events from $Z \to \tau\tau$ and from which we measure the new scale factors and efficiency. We found that this new scale factors at low p_T is dominated my the Z process and at high p_T by $t\bar{t}$.Which is what we expected. This should be better than combining the SF separately because we have aligned out phase-space and background estimation with an offline Tau analysis.

This work was part of my qualification task on ATLAS in which I detailed the $Z \to \tau\tau$ trigger efficiency measurements using the Tag-and-Probe method. A significant portion was dedicated to constructing a new signal region to obtain a new scale factor for higher energies, coming from processes like $t\bar{t} \to \tau\tau$. Finally, to propose a single Scale factor that corrects the modeling at low and high energies for different process.

With this we are able applied the concepts using another trigger for the selection required to look for a Higgs pair production. This analysis uses a pair of τ's particles in the final state. In which we have one hadronic decay and one leptonic tau decay. Similarly to what we have, but with other triggers. Single Lepton trigger (SLT) and Lepton Tau triggers (LTT)

Also a similar approach will used in the calculation of the Fake Factors to correct the miss-modeling for this analysis, but using a Data Driven method that will be introduce in section 6.3.

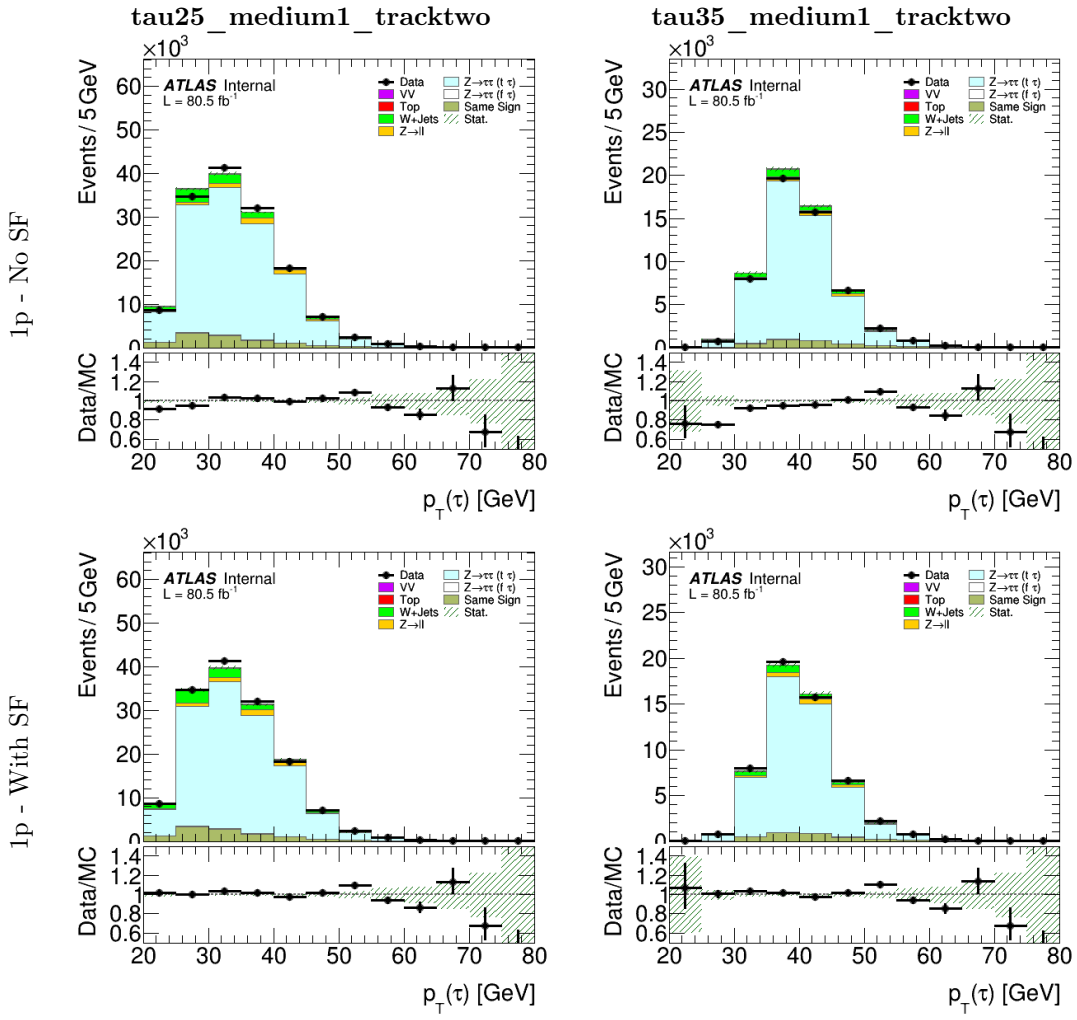

Table 4.10: Here, we compare the distribution plots of the momentum p_t on the first row versus the same plots but where the SF has been applied (second row). And we can appreciate especially in the case of 3 prong the improvement of this correction have on the modelling For $Z \to \tau\tau$.

Chapter 5

Decay of Higgs boson pair to $b\bar{b}\tau_{lep}\tau_{had}$ channel final state

This thesis is based on the analysis of searching for Higgs boson pair production in a final state with two b-quarks and two $\tau-$leptons considering two decay sub-channels, $\tau_{lep}\tau_{had}$ and $\tau_{had}\tau_{had}$. The subscripts, lep = lepton and had = hadron, denote the decay mode of the τ -lepton. The study presented in this thesis focuses on the calculation of the fake factors applied in the search in the SM pair production of Higgs bosons in the decay sub channels just mention. 4.7

The author's collaboration to the analyses presented in this chapter is as follows. Validate the migration from the MIA frame work to the CxAODReader frame work, which implies the corroboration of the yields from one framework to the other with the internal support note [ATL21] and to estimate the calculation of the fake$\tau_{had-vis}$ background for the SLT and LTT channels for the $\tau_{lep}\tau_{had}$. Also validating the calculation of the fake factors in their corresponding validations region's $(0b, 1b - tag)$

5.1 Data and simulation framework

The data samples used for the analysis have previously gone through a process chain, illustrated in the left part of Figure 5.1. First, as long as the data taking is running, the ATLAS trigger system decides which events get written to the disk. As it has already been mentioned in subsection 5.2.2, the LHC delivers events with a rate of up to 40 MHz, while ATLAS can afford to record up to 1 kHz, meaning that only one in 40.000 events can be kept. Hence, a clear-out among the events should be carried out by the two-step mechanism of the ATLAS trigger system, so that all interesting events are stored. Then, the output of the trigger, raw data, is organised into streams and used for reconstruction. The output produced by the reconstruction is AOD, which stands for analysis object data. The next step is the production of derived AOD (DAOD) files that are much smaller and contain the information specific to a targeted final state.

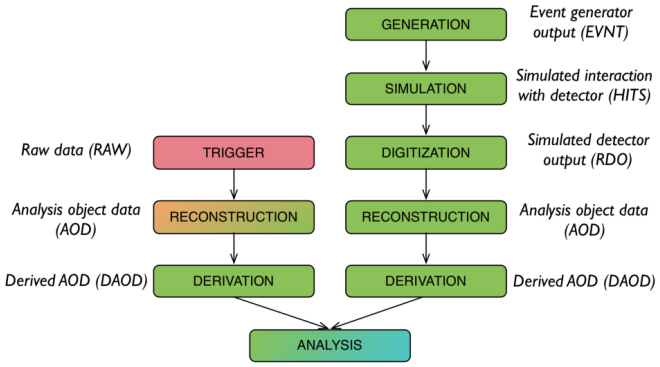

Figure 5.1: The ATLAS data (left) and MC samples (right) processing chain

Apart from the data samples, it is necessary to have Monte Carlo (MC) simulation samples for the signal and background processes. Several steps are included in the production of MC simulated samples, such as event generation, parton showering, hadronization and detector simulation. These steps are presented in the right side of the sketch in Figure 5.1. The interactions

between quarks and gluons in the proton-proton collisions are simulated during the event generation, while the interactions of outgoing particles, arising from the generator, with the detector material are computed during the detector simulation: the deposited energy in each sensitive element of the detector is determined. During the digitization, the simulated energy deposits are turned into a detector response, looking similar to the raw data from the real detector. After this step, the process is the same as for real data.

The signal and background samples used in this thesis are official ATLAS samples and have been used in the published analysis. The SM HH signal sample is simulated with MadGraph5 , while parton showers and hadronization are simulated with $Herwig++$. Table 5.1 shows how the different background MC samples are generated. All the plots presented in this thesis are edited with ROOT .

Background					
Processes	MC order	Generator	Parton shower	PDF	Tune [-2em]
$t\bar{t}$and single-top	NLO	Powheg-box	Pythia 6	CT10	Perugia 2012
$Z/W + jets$	NLO	Sherpa 2.2.1		NNPDF30NNLO	
Diboson and Drell-Yan	NLO	Sherpa 2.2.1		CT10NLO	
quark induced ZH	NLO	Pythia 8		NNPDF23LO	A14
qluon induced ZH	NLO	Powheg	Pythia 8	CT10	AZNLO
ttH	NLO	MadGraph5_aMC@NLO	Pythia 8	NNPDF23LO	A14
Signal					
$SMHH \to b\bar{b}\tau^+\tau^-$	NLO	MadGraph5_aMC@NLO	Herwig ++	CT10	UEEE5

Table 5.1: List of MC generated background samples and the signal sample used in the analysis and the event generators for the different process.

5.1.1 Data and Monte Carlo samples

The analysis uses pp collision data at a centre-of-mass energy of$\sqrt{s} = 13\ TeV$ recorded by ATLAS in 2016, 2017 and 2018, corresponding to an integrated luminosity of 139.0 fb^{-1} after the application of the Good-Run-List requirement (GRL) that ensures that all the relevant components of the ATLAS detector were fully operational during the data taking.

Monte Carlo (MC) samples used by this analysis are produced with the ATLAS simulation infrastructure [[Col10]] for both signal and background. Signal and background MC samples are described in the following sections.

Background

Where $p_T^{\tau_{had}}$ is the transverse momentum of the hadronically-decaying τ -lepton, for all of the relevant background processes, in the zero, one and two b-tag regions. In all three regions the background distribution is consistent with the data, which are shown as black points with error bars.

The background processes considered in both analyses are listed below.

- The dominant background process is the pair-production of top-quarks, referred to as $t\bar{t}$ production, which constitutes over 90% of the total background in the two b-tag signal region. Any $t\bar{t}$ processes that include a real hadronically decaying τ -lepton are modelled using MC simulation, as described in the following section , and are labelled '$t\bar{t}$'.
- Processes where a jet is misidentified as a hadronically decaying$\tau-$lepton are not well modelled in MC simulation; therefore, they are modelled using a data-driven method and are shown as a single background labelled 'fake'. These processes are $tt\bar{t}$, $W + jets$, and QCD multi-jet.
- Single top production, which includes the $s-$ and $t-$channels and Wt associated production, is labelled as 'single top'.

- $Z \to \tau\tau$ processes, where a Z boson, which is produced in association with any combination of $b-$, $c-$ and light-flavour jets, decays to a pair of $\tau-$leptons, are labelled as$Z \to \tau\tau + [bb, bc, bl, cc, cl, l]$.
- $Z \to ll$ processes where a Z boson, produced in association with jets, decays to a pair of light leptons, are labelled $Zee/\mu\mu$ in Figure . The $Z \to \mu\mu$ process is negligible because a muon is unlikely to deposit enough energy in the calorimeters to be misidentified as a τ_{had} .
- Drell-Yan processes where a pair of leptons are pair-produced, are included as $DY\tau\tau$ and $DYee/\mu\mu$.
- Di-boson processes involving combinations of two Z and W bosons, i.e. WW, ZW and WW , are referred as diboson.
- Processes involving a single SM Higgs boson, including the associated production of a Z boson or $tt\bar{t}$ pair and a Higgs (referred to as Zh or ttH production), are shown as a single background labelled SM H

5.2 Trigger and Event selection

Following the reconstruction of detector objects, an event selection is applied so that the selected final state consists of two $\tau_{had-vis}$ candidates of opposite charge satisfying the "medium" identification (ID) criteria, along with two b-tagged jets and E_T^{miss}.

This analysis uses Boosted Decision Tree(BDT) to isolate and discriminate signals from background instead of using series of cuts to do so. However, several preselection criteria have to be applied to get rid of significant amount of background before using BDT, as well as to define signal regions and control regions in both $\tau_{lep}\tau_{had}$ and $\tau_{had}\tau_{had}$ channels for the data analysis. The BDT plays a critical role in this analysis which turned out to be one of the key features we have chosen to make our final result stand out among all the di-Higgs final states analysis on ATLAS.

5.2.1 $\tau_{lep}\tau_{had}$ trigger selection

In the $\tau_{lep}\tau_{ha}d$ analysis uses events that are first checked to see if they pass one of the single lepton triggers (SLTs). In the electron channel, multiple single electron triggers are used to maximise event acceptance. The events are required to have the following cuts:

- At least one electron with $p_T > 25GeV$, passing "medium" identification criteria and "loose" isolation requirements. In the later data-taking periods, the electron p_T threshold is raised to 26 GeV , with the identification working point changed to "tight".
- Events are required to have a muon with $p_T > 24 - 26$ GeV corresponding to different data-taking periods, passing the "loose" isolation criteria
- And finally and hadronic τ with $pT > 20$ GeV

And, in the case of failing the SLTs, the the events are tested to se if they pass the lepton-plus-τ_{had} triggers (LTT). In this trigger the events are required to have the following cuts:

- The LTT triggers require either an electron with $p_T > 18$ GeV or a muon with $pT > 15$ GeV , together with a hadronic τ with $pT > 30$ GeV

The trigger requirements vary with the data-taking period; the p_T threshold and identification requirements were increased to keep the rate of data consistent whilst the instantaneous luminosity increased. The triggers and their corresponding requirements are summarised in Table

Events are analysed separately based on the type of trigger they are selected by. The contribution of this thesis focused on analysing the SLT events; therefore, only the SLTs are outlined here. We will remark on the LTT as well, but it is an ongoing research in the analysis team and they results are still not final. So we will present just some preliminary result for this. (For both $\tau_{lep}\tau_{had}$ and $\tau_{had}\tau_{had}$ channel, all triggers are run un-prescaled. The electrons, muons,

and τs reconstructed offline are required to pass the truth-matching to match the triggered objects.)

5.2.2 Event Selection

An event selection is applied to all events that pass the trigger selection in order to select a final state containing an electron or muon, l, a $\tau_{had-vis}$, at least 2 jets and missing transverse momentum. Events are subject to the following requirements (using the object definitions described in Chapter

- SLT
  - Exactly one electron passing the 'tight' identification criteria or one mu on passing the 'medium' identification criteria (this also includes a requirement that the muon must have $|\eta| < 2.5$), with p_T 1 GeV (so it goes up to 27 GeV) above the corresponding trigger threshold used in that data-taking period making sure the trigger efficiency is fully turned on.
  - exactly one hadronic$\tau-$lepton with $p_T > 20$ GeV and $|\eta| > 2.3$
  - At least two jets in the event with $p_T > 45(20)$ GeV for the leading (sub-leading) jet.
- LTT
  - Exactly one electron passing the 'tight' identification criteria and with $p_T > 18$ GeV , or one muon passing the 'medium' identification criteria with $p_T > 15$ GeV . An upper limit on the p_T corresponding to the equivalent SLT thresholds for that data-taking period is applied.
  - Exactly one hadronic τ with $p_T > 30$ GeV and $|\eta| < 2.3$
  - At least two jets in the event with $p_T > 80(20)$ GeV for the leading (sub-leading) jet. The p_T threshold for the leading jet is due to the requirement of the presence of a jet in the event for the Level-1 trigger.
- Opposite-sign eletric charge (OS) between the τ and the light lepton electron or muon (e/μ)
- the invariant mass of the $di-\tau$ system must be $m_{\tau\tau}^{MMC} < 60\ GeV$.
- The invariant mass (m_{bb}) of thee_2 b-tagged jets is required to be less than 150 GeV to reject $t\bar{t}$ background events

The full event selection for the $\tau_{lep}\tau_{had}$ analysis is summarised in Table 5.2. Following the above selection, events are categorised according to the multiplicity of b-tagged jets in the event. The signal region requires exactly two b-tagged jets, whilst events with zero or one b-tags are used for validating the background modelling (events with zero b-tags use the two jets with highest p_T and events with one b-tag consider the b-tagged jet and the highest-p_T non-tagged jet).

Table 5.2: Summary of the event pre-selections for the signal region event selection for the $bb\tau_{lep}\tau_{had}$ decay channel. Shown separately for the SLT and LTT. Thresholds on the (sub-)leading p_T object are given outside (within) parentheses.

$\tau_{lep}\tau_{had}$ categories	
SLT	**LTT**
Electron(e)/**Muon**(μ) selection	
Choosing one tight electron or medium muon	
$p_T^e < 25, 27$ **Gev**	$18 < p_T^e <$ SLT cut
$p_T^\mu < 21, 27$ **Gev**	$15 < p_T^\mu <$ LTT cut
$\lvert\eta^e\rvert < 2.47$ excluding $1.37 < \lvert\eta^e\rvert < 1.52$	
$\lvert\eta^\mu\rvert < 2.7$	
$\tau_{had-vis}$ **selection**	
We require one loose $\tau_{had-vus}$	
$\lvert\eta\rvert < 2.3$	
$p_T^\tau > 20$ **GeV**	$p_T^\tau > 30$ **GeV**
Jet Selection	
2 b jets with $\lvert\eta\rvert < 2.5$	
$p_T > 45(20)$	Depends on the trigger
Event Selection	
Pass the trigger requirements	
Vertex reconstructed	
$m_{\tau\tau}^{MMC} > 60$ **GeV**	
Opposite electric sing between e/μ and $\tau_{had-vis}$	
Exactly 2 b-tagged jets	
$m_{bb} < 150$ **GeV**	

5.3 Event categorization

The events passing all the selection criteria described above are further divided into three mutually exclusive categories, as shown in the sketch of Figure 5.2, resulting in three signal regions per sub-channel. The events forming these signal regions are then used for the fit of the MVA discriminant distributions. If an event has at least four jets, it goes through a ggF/VBF BDT classifier which aims to optimally separate events originating from ggF and VBF production modes. Then, if the event passes a certain ggF/VBF BDT working point, it is considered VBF-like and falls into the dedicated VBF signal region. On the other hand, if an event has less than four jets or fails the ggF/VBF BDT cut, it is considered ggF-like and is further categorised based on the invariant mass of the di-Higgs system, m_{HH}.

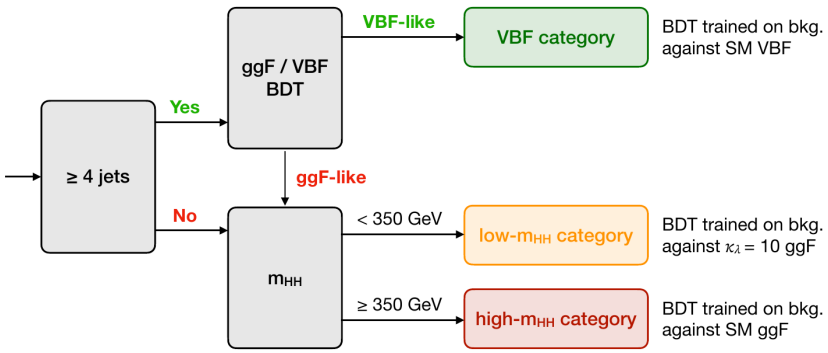

Figure 5.2: Event categorization into low-m_{HH} ggF, high-m_{HH} ggF and VBF signal regions.

At the moment of this thesis was done, the VBF categorization in the analysis was an ongoing

work, so the actual selection use in this work can bee seen Figure 5.3, also the $\tau_{lep}\tau_{had}$ LTT channel strategy it's yet to be finalized, so given its low sensitivity the strategy follow here was the one used in the previous analysis round (one inclusive SR and NN score). And for this thesis, we will present only the SLT for the $\tau_{lep}\tau_{had}$ results that are in the current internal note this analysis.

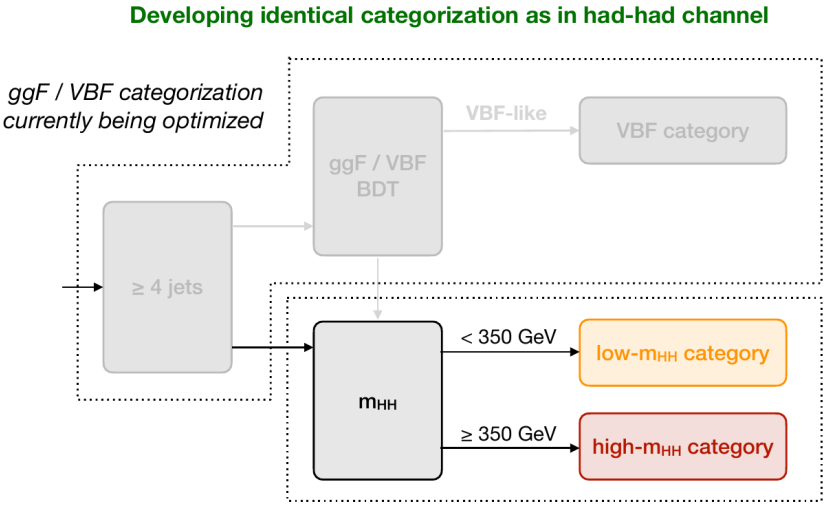

Figure 5.3: Event categorisation into low-m_{HH} ggF, high-m_{HH} ggF signal regions.

5.4 Boosted decision tree training

The multivariate analysis technique of BDTs is widely used by the ATLAS Collaboration. Boosted decision trees(BDTs) are used in this analysis to discriminate the signals from background processes instead of using different cuts on the kinematic distributions of the events.

Variables describing the kinematics of events can be used to provide varying degrees of discrimination between signal and background. Whilst some of these can be used to place cuts on the data, removing significant amounts of background, others exhibit only minor separation power. By combining these variables in a BDT, it is possible to exploit the correlations between the variables to achieve increased sensitivity to the signal process relative to using a cuts-based analysis, producing a single distribution for which signal and background are well-separated.

Since many variables can be correlated, the benefit of using multivariate techniques is that they take into account such correlations [Bha11]. Multivariate analysis (MVA) methods, based on machine learning, are widely used in particle physics, mostly for signal and background classification. For this reason, a Toolkit for Multivariate Analysis (TMVA) [H$^+$07], has been developed and integrated into the analysis framework ROOT. The TMVA includes different algorithms for multivariate classification, for instance, Boosted Decision Trees (BDTs).

The BDT score distribution is used as the discriminant in the statistical fit for hypothesis testing.

A decision tree is a kind of machine-learning algorithm that could be used for both classification and regression problems. It's a binary classifier in the shape of a tree, consisting of nodes and leaves. Decision trees (DTs) consist of recursive left/right decisions which determine the classification of data, based on sequential cuts applied to a single variable at each time. At each step in the sequence, the best cut is looked for and used to split the data until at the end a terminal criterion is fulfilled. As shown in Figure 5.4, all decisions begin from an initial, root node, and each leaf gets assigned one of two classes, like for example signal or background, consequent to a binary decision taken at each node. The splitting of data stops when impurity cannot be further reduced. A measure of impurity is the Gini index, which is given by:

$$Giani = (s+b)P(1-P) = \frac{sb}{s+b} \tag{5.1}$$

With $P = s/(s+b)$ being the signal purity and s, b referring to the signal and background events, respectively. Ultimately, all events are assigned to one of the classes and are given a score, which usually ranges between -1 and +1. Background-like events get a score near -1, while signal-like events have a score close to $+1$

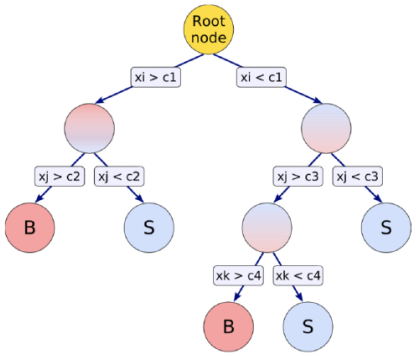

(a) CxAODReader

Figure 5.4: Illustration of a binary decision tree [33]. Each branch of the decision tree represents a sequence of cuts, which classifies an event as signal (S) or background (B).

The $\tau_{lep}\tau_{had}$ MVA strategy closely follows the $\tau_{had}\tau_{had}$ channel approach. One BDT is trained to separate ggF from VBF di-Higgs production and used to define dedicated SRs for both processes. In each of the three SRs, a dedicated BDT is used to separate the signal from the background. The score of this BDT is also used as a final discriminant in the fit.

Variables

The TMVA is used for the training and evaluation of various BDTs. Several variables that provide good discrimination between signal and background are used as inputs to the BDT, and are listed in Table 5.3 for the $\tau_{lep}\tau_{had}$ search channel [ATL21]

Table 5.3: Variables used as inputs to the MVAs in the three analysis categories. The choice of input variables is used for the non-resonant production modes [ATL21]

	$\tau_{lep}\tau_{had}$ channel	
Variables	**SLT** $\tau_{lep}\tau_{had}$	**LTT** $\tau_{lep}\tau_{had}$
m_{HH}	✓	✓
$m_{\tau\tau}^{MMC}$	✓	✓
m_{bb}	✓	✓
$\Delta R(\tau,\tau)$	✓	✓
$\Delta R(b,b)$	✓	
$\Delta p(l,\tau)$	✓	✓
Sub-leading b-tagged jet p_T	✓	
m_T^W	✓	
E_T^{miss}	✓	
p_T^{miss} ϕ centrality	✓	
$\Delta\phi(l\tau, bb)$	✓	
$\Delta\phi(l, \vec{p}_T^{miss})$		✓
$\Delta\phi(l\tau, \vec{p}_T^{miss})$		✓
S_T		✓

The variables with the best separation power between signals and backgrounds are used as the BDT input variables. Different variables are used for different sub-channels which is as expected because of different particle composition and kinematic distributions in sub-channels. These variables are selected by choosing the highest-ranked variables with the removal of the highly correlated ones. Definitions of the variables used are listed below:

- m_{HH} : The invariant mass of the di-Higgs system. Which is reconstructed from the di-tau and di-b-jet systems. Scale factors are applied to the four-momenta of the di-tau and di-b-jet systems, respectively, in order to improve the mass resolution.
- $m_{\tau\tau}^{MMC}$: is the invariant mass of the $di-\tau$ system, calculated using the Missing Mass Calculator algorithm.
- m_{bb}: The invariant mass of the di-b-jet system
- $\Delta R(\tau,\tau)\Delta R(b,b)$: These are the distance evaluated between one $\tau_{had-vis}$ decay products (the electron or muon) and τ_{lep}. And the second one is the distance between two b-tagged jets.
- $\Delta p(l,\tau)$: The difference in pT between the light lepton and the visible hadronic tau decay products.
- $p_T^{BB}, p_T^{B1}, p_T^{B2}$: The first one is the transverse momentum of the leading b-jets . The second one is the transverse momentum of the sub-leading b-jet and one leading (variable in study) . And the third one is the transverse momentum of the sub-leading b-jet (variable in study)
- $\Delta\phi(l,\vec{p}_T^{miss})$: is the azimuthal angle between the lepton and the $\vec{p}_T^{miss}$)
- $\Delta\phi(l\tau,\vec{p}_T^{miss})$: is the azimuthal angle between the electron or muon and $\tau_{had-vis}$ system and the $\vec{p}_T^{miss}$)
- $\Delta\phi(l\tau, bb$): is the azimuthal angle between the $l+\tau_{had-vis}$system and the b-tagged jet pair
- The transverse mass between the lepton and the E_T^{miss} is defined as:

$$m_T^W = \sqrt{2p_T^l E_T^{miss} - (1-\cos\Delta\phi)}$$

  where p_T^l is the transverse momentum of the lepton. Signal events tend to have a lower m_T^W than the $tt\bar{t}$ process because the transverse mass of a lepton and neutrino decaying from a W boson in a $t\bar{t}$ event tends to peak at $m_T^W \sim 80$ GeV .
- $E_T^{miss}\phi$ centrality: Is a measurement of the angular position, ϕ, of the missing transverse momentum, E_T^{miss} , with respect to the visible decay products of the two τ objects. Its definition is given by:

$$E_T^{miss}\phi\textbf{centrality} := \frac{A+B}{\sqrt{A^2}+B^2}$$

  where A and B are given by:

$$A = \frac{\sin\phi_{E_T^{miss}} - \sin\phi_{\tau_2}}{\sin\phi_{\tau_1} - \sin\phi_{\tau_2}}, B = \frac{\sin\phi_{\tau_1} - \sin\phi_{E_T^{miss}}}{\sin\phi_{\tau_1} - \sin\phi_{\tau_2}}$$

  The $E_T^{miss}\phi$ centrality should be equal to:
  - $\sqrt{2}$, when the E_T^{miss} is exactly between the two $\tau_{has-vis}$ objects
  - 1, if the E_T^{miss} lines up with either of the $\tau_{has-vis}$ objects
  - less than 1, if the E_T^{miss} lies outside of the angular region that the two $\tau_{has-vis}$ objects form

5.5 Overlap removal

After the event is reconstructed, an overlap-removal procedure is applied to resolve ambiguities when a physical object is reconstructed as multiple particles in the ATLAS detector. The angular distance ΔR is used to measure the overlap of two reconstructed objects. Overlaps between

most of the detector objects used in the analysis are resolved by using the standard overlap removal tools AssociationUtils*, with analysis-specific procedures for the reconstructedτ_{had}, $anti-\tau$ had objects and jets. The step-by-step procedure that is used to resolve ambiguities in the reconstructed objects is summarised in the following:

- e_1-e_2 : For two electrons e_1 and e_2 in an event, reject e_1 if both electrons share the track and $p_T^1 < p_T^2$
- τ_{had} $-e$: Reject τ_{had} if $\Delta R < 0.2$
- τ_{had} $-\mu$: Reject τ_{had} if $\Delta R < 0.2$:
  - Case (e_1) (τ_{had} $p_T > 50\mathbf{GeV}$): $p_T, \mu > 2\mathbf{GeV}$ and combined muon
  - Case (e_2) (τ_{had} $p_T \leq 50\mathbf{GeV}$): $p_T, \mu > 2\mathbf{GeV}$
- $\mu - e$: Reject μ if calo-muon and shared ID track
- $e - \mu$: Reject e if shared ID track
- jet-e: Reject jet if $\Delta R < 0.2$
- e–jet: Reject e if $\Delta R < 0.4$

Additionally, an analysis-specific overlap-removal procedure for τ_{had} anti-τ_{had} and jets is implemented:

- jet$-\tau_{had}$: Reject jet if $\Delta R < 0.2$
- anti$-\tau_{had}$ –jet: Reject anti$-\tau_{had}$ if jet is b-tagged and $\Delta R < 0.2$
- jet–anti$-\tau_{had}$: Reject jet if $\Delta R < 0.2$

*We can find this tool in: Toolkit-repository

Chapter 6

The Fake Factor Method: Background estimation

Misidentification is an essential source of background for physics analysis using particle-level identification criteria. In the case of the di-lepton analysis presented in this thesis, this background arises from $t\bar{t}, Z + HF$ events; for example, this occurs when a jet is misidentified as a lepton. It is important to measure this type of background from the data as the rate of misidentification, because it may not be accurately modeled in the MC. The "fake factor" method is a data-driven procedure for modeling background from particle misidentification.

6.1 Background estimation methods in the HH analysis

This section describes the background estimation methods used in the Di-Higgs analysis for the $\tau_{lep}\tau_{had}$ channel.

The simulated event samples summarized in Table 5.1 are used to model all background processes, except for processes with $fake-\tau_{had}$, which are estimated using data-driven techniques, as discussed below. In the $\tau_{lep}\tau_{had}$ channel, all $fake-\tau_{had}$ backgrounds from $t\bar{t}$ and multi-jet processes are estimated using an inclusive fake-factor method, described in following Section.

The $t\bar{t}$ with $true-\tau_{had}$ and $Z + HF$ templates are taken from the MC prediction, but their normalization are derived from data as included as freely floating parameters in the final fit. Events with electrons or muons that are misidentified as τ_{had} objects, dominantly coming from the $t\bar{t}$ production, represent a minor background in the analysis and they are estimated from simulation. This background is treated together with the $t\bar{t}$ events containing $true-\tau_{had}$ objects.

During the work on this analysis, there was a task of migrating the software, which was used to calculate this. The old software MIA* was used in the $\tau_{lep}\tau_{had}$ channel, and the CxAODReader† was used in the $\tau_{had}\tau_{had}$. A way to unify everything and have only one software to work in both channel a migration task work was done. The first step in this migration was to have consistencies in the yield for the different processes. In this was we can corroborate that the cuts and trigger were correctly implemented. In order to corroborate this, we compare these yields and reproduce with the one in the internal note [BBB+20]. And as we can see on Table 6.1 we have a 99% agreement overall in most of the samples. After this, we could more forward in the comparison of the fakes factors of one framework to the other.

*This can be found in: MIA-Reposository
†This can be found in: Reader-Reposository

Internal note 2018		
Sample Name	entries	Integral
Fake	2089776	33915.8
ttbar	490058	61622.2
stopWt	25910	3053.72
stopt	5798	596.49
stops	1450	38.80
Zbb	17645	795.54
Zbc	1467	74.58
Zbl	1006	39.16
Zcc	278	78.68
Zcl	135	21.92
Zl	30	4.13
Zttbb	21473	1426.16
Zttbc	1746	132.24
Zttbl	1184	62.98
Zttcc	608	133.72
Zttcl	216	12.52
Zttl	122	15.51
Wtt	76	5.36
WW	110	13.30
WZ	1992	58.53
ZZ	6754	82.81
W	747	75.35
DY	68	14.82
DYtt	9	2.72
VBFHtautau	933	1.41
ggFHtautau	2159	17.06
ggZHtautau	838	2.87
ZHtautau	1923	8.48
WHtautau	92	0.70
ggZHbb	17317	5.80
qqZHbb	71572	17.68
WHbb	6054	6.94
ttH	133199	92.99
total bkg	2.902745E+06	102431.00
data	98456	98456

Table 6.1: a

MIA frame work		
Sample Name	entries	Integral
Fake	2208091	29742.6
ttbar	490058	61707.3
stopWt	25910	3068.72
stopt	5798	597.845
stops	1450	38.0951
Zbc	1467	80.0456
Zbl	1006	39.466
Zcc	278	88.7066
Zcl	135	23.1748
Zl	30	21.0477
Zttbb	21473	1448.64
Zttbc	1746	141.349
Zttbl	1184	62.7492
Zttcc	608	165.596
Zttcl	216	12.6376
Zttl	122	15.5227
Wtt	76	5.51685
WW	110	13.7836
WZ	1992	60.1072
ZZ	6754	84.6051
W	75.3549	211.31
DY	68	14.7176
WHbb	6054	6.94652
VBFHtautau	933	1.4224
ggFHtautau	2159	17.1723
ggZHtautau	838	2.87863
ZHtautau	1923	8.49719
WHtautau	92	0.714224
ZHbb	88889	23.4744
WHbb	6054	6.94652
ttH	37692	58.0918
bkg:	2.97E+06	98317.6
data	98456	98456

Table 6.2: b

CxAODReader frame work		
Fake	2208091	29742.6
ttbar	490058	61707.3
stopWt	25910	3068.72
stopt	5798	597.845
stops	1450	38.0951
Zbc	1467	80.0456
Zbl	1006	39.466
Zcc	278	88.7066
Zcl	135	23.1748
Zl	30	21.0477
Zttbb	21473	1448.64
Zttbc	1746	141.349
Zttbl	1184	62.7492
Zttcc	608	165.596
Zttcl	216	12.6376
Zttl	122	15.5227
Wtt	76	5.51685
WW	110	13.7836
WZ	1992	60.1072
ZZ	6754	84.6051
W	75.3549	211.31
DY	68	14.7176
WHbb	6054	6.94652
VBFHtautau	933	1.4224
ggFHtautau	2159	17.1723
ggZHtautau	838	2.87863
ZHtautau	1923	8.49719
WHtautau	92	0.714224
ZHbb	88889	23.4744
WHbb	6054	6.94652
ttH	37692	58.0918
bkg:	2.97E+06	98317.6
data	98456	98456

Table 6.3: c

Table 6.4: We compare the yields from the Support Note in Table 6.1 for the SLT channel, this was taken from [BBB+20] with the Yield of the two frameworks MIA Table 6.2 and CxAODReader 6.3

The yields of the fakes estimated using Reader framework and MIA differ by .1%. The next step in this work was to compare the fake factors we obtained from both software's (MIA and CxAODReader). In Figure 6.1, we can observe that we have almost a perfect agreement between the two factors from both frameworks in one prong and in Figure 6.2 for 3 prong.

The calculation of these factors will be detail in the following section. But now we have achieved our first task. We can beging to work on getting the factors with the new framework (Reader) and apply them to the signal and validations regions and investigate the impact in the signal region. What we will see is that a clear miss-modeling will be appreciated in the plots before the factors, and once these are applied we will see how the miss-modeling improves.

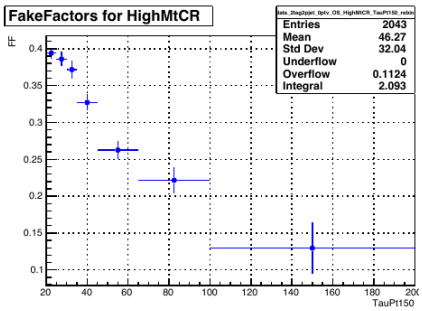

(a) CxAODReader

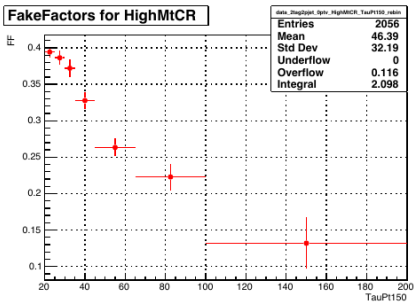

(b) MIA

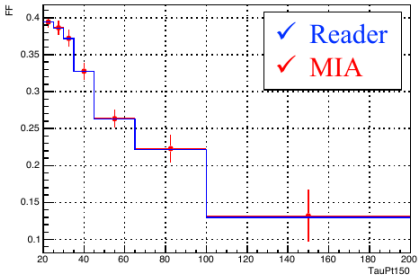

(c) Comparison between two framework

Figure 6.1: Comparison of the Fake Factor calculations between MIA and Reader for validating the migration for 1 prong LTT channel.

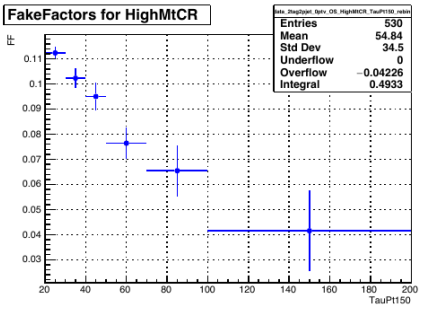

(a) CxAODReader

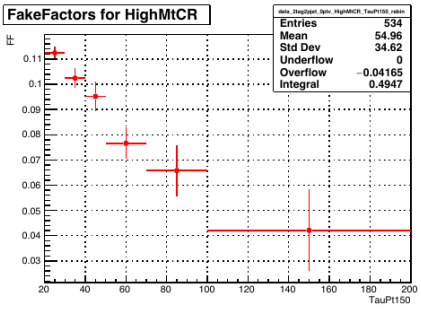

(b) MIA

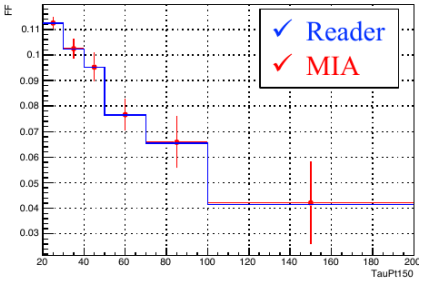

(c) Comparison between two framework

Figure 6.2: Comparison of the Fake Factor calculations between MIA and Reader for 3 prong SLT channel.

6.2 Fake-τ backgrounds in the $\tau_{lep}\tau_{had}$ channel

6.2.1 Anti$^{\smile}\tau_{had}$ selection

In order to provide fake $-\tau_{had}$enriched regions used for background estimation, an $anti-\tau_{had}$ selection is defined as:

Those τ_{had} objects that fail the RNN Loose τ_{had} –ID and have an RNN score greater than 0.01 are labeled as $anti-\tau_{had}$ candidates. The RNN cut is used and recommended by the Fake-Tau-Task-Force . The minimum RNN score cut ensures that the jet has features somewhat similar to a true τ_{had} and hence that the composition of the jet (either quark- or gluon-initiated) would be more similar to that in the SR.

Exactly one $anti-\tau_{had}$ object is selected when there is no τ_{had} passing the offline τ_{had} -ID requirement. This is to ensure only one τ_{had} object (either true τ_{had} or $anti-\tau_{had}$) is selected. For the LTT channel where τ_{had} –ID is applied at trigger level, only the $anti-\tau_{had}$ object that is matched to the trigger τ_{had} is considered, and thus there are no multiple selection possibilities. However, for the SLT channel where a τ had trigger is not used, an $anti-\tau_{had}$ candidate is chosen randomly when there are more reconstructed τ had satisfying the anti-τ_{had} definition. Any anti-τ had objects that are not selected in this process are also not considered when performing the overlap removal of detector objects. Derived variables used in the analysis, such as the $E_T^{miss}, m_{\tau\tau}^{MMC}$ and E_T^{miss} ϕ centrality (more details in the following section) are calculated in the same way as for signal events, but with the anti-τ_{had} taking the place of the loose τ_{had} candidate.

6.2.2 Z + HF control region event selection

The Z boson production in association with heavy flavor jets, i.e. $b-, c-jets$ (Z + HF background) is known to be not well modeled by the Sherpa generator. Therefore, a dedicated control region event selection is defined to select $Z \to \mu\mu/ee+$ heavy flavor jets events. Since the production of jets is independent of the decay mode of the Z boson, this selection provides an orthogonal region with high purity to the SR, which requires two τ leptons in the final state. The normalization is extracted from this region, and it also provides constraints on the normalization of the $t\bar{t}$background. The event selection is defined as follows:

- Events are selected using the single-lepton and di-lepton triggers.
- Exactly two leptons (e/μ) with opposite-sign charges and p $T > 9$ GeV are required, these leptons are also required to be compatible with the primary vertex. In addition, they are required to pass the medium and loose isolation requirements.
- Exactly two b-tagged jets.
- The reconstructed mass of the two leptons is required to be between 75 GeV and 110 GeV, to be consistent with the Z boson mass.
- $m_{bb} < 40$ GeV or $m_{bb} > 210$ GeV to veto Higgs mass peak.

6.2.3 Background estimation

This section describes the background estimation methods used in the di-Higgs analysis. The dominant background is the $t\bar{t}$background, followed by the single top and the $Z + HF$ backgrounds. The simulated event samples summarised in Section 5.1.1 are used to model all background processes, except for the $fake-\tau_{had}$ background where a jet fakes a τ_{had}. It is estimated using data-driven techniques as discussed below. In particular, the lepton faking τ_{had} background is modeled by simulation, as its contribution is found to be very small compared to the jet faking τ_{had} background. The $t\bar{t}$ with true-τ_{had} and Z + HF templates are taken from the MC prediction, but their normalization's are derived from data as included as freely floating parameters in the final fit.

Background with a jet misidentified as a τ_{had}

The $fake - \tau_{had}$ background can have different origins. In Figure 6.3, two Feynman diagrams are shown for the two dominant processes contributing to the fake$-\tau_{had}$ background, which are the $t\bar{t}$and multi-jet (referred to as QCD) processes.

In the $t\bar{t}$ events, the fake$-\tau_{had}$ background typically originates from quark-initiated jets from top quark decay; in multi-jet events, jets initiated from both quarks and gluons can be misidentified as τ_{had}. In the following text, the fake background initiated by the $t\bar{t}$ (multi-jet) events is referred to as $t\bar{t}$(multi-jet) fakes.

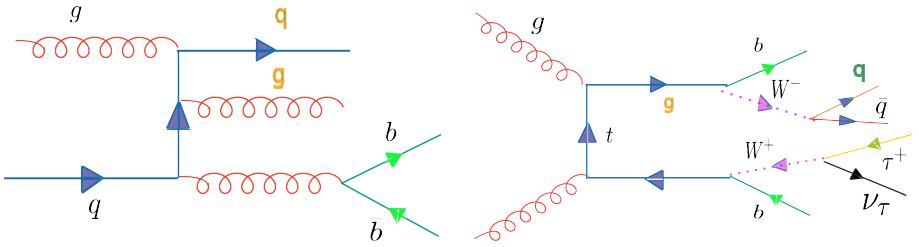

(a) Multi-Jets diagram (b) $t\bar{t}$ Process

Figure 6.3: Feynman diagrams with fake taus. On the left for the multi-jet 6.3a originated $fake - \tau_{had}$ background. The gluon and quark in orange in the left diagram fake a τ_{had} and a lepton, respectively. The diagram on the left 6.3b that corresponds to the $t\bar{t}$ has a quark on green that fakes a τ_{had}.

6.3 Fake Factor Method

The fundamental idea of the fake factor method is to select a control sample of events enriched in the background being estimated, and then use an extrapolation factor to relate these events to the background in the signal region. The method is data-driven. Provided the control sample is selected in data, and the extrapolation factor is measured with data. For background arising from particle misidentification, the extrapolation is done in particle identification space. The control sample is defined using alternative particle selection criteria that are chosen such that the rate of misidentification is increased. The extrapolation factor relates background misidentified with this criteria, to background misidentified as passing the full particle selection of the signal region. The extrapolation factor is referred to as the "fake factor". The fake factor is measured and applied under the assumption that it is a local property of the particles being misidentified and is independent of the event-level quantities. The fact that the extrapolation is done in an abstract particle identification space can be conceptually challenging, but the underlying procedure is straightforward. The control region is defined in order to select the background being estimated. The type of background considered with the fake factor method arises from particle misidentification. To collect this type of background more efficiently, the particle selection in the signal region is replaced with a particle selection for which the misidentification rate is higher. This alternative particle selection criteria is referred to as the "denominator selection" or the "denominator definition"; particles passing this criteria are referred to as "denominator objects" or simply "denominators". The control region is then defined to be the same as the signal region, except a denominator object is required in place of the full particle selection in the signal region.

In the $\tau_{lep}\tau_{had}$ channel, the major source of the backgrounds where reconstructed hadronic τs are faked by jets(fake τ background) are$t\bar{t}$, $W + jets$ and multi-jet background. The $fake - \tau_{had}$ background events are estimated using a data-driven method, the **fake factor (FF)** method, here we calculate a "combined fake factor" method to estimate the fake τ background all at once in the $\tau_{lep}\tau_{had}$ channel, due to the imperfect simulation of these processes. In short, the fake factor is the ratio of the number of events with $fake - \tau_{had}$ in one region to another region. The τ "fake-factor" is used to weight the fake-τ events in the control region to get the right modeling of the corresponding background in the signal region(SR).

The fake factor for a given background source is defined as:

$$FF = \frac{\textbf{N (ID selection)}}{\textbf{(anti-ID selection)}} \tag{6.1}$$

Where the numerator is the number of $fake - \tau_{had}$ background events passing the nominal signal region τ_{had}-ID selection (referred to as ID selection in the following), and the denominator is the number of $fake - \tau_{had}$ background events passing the $anti - \tau_{had}$ selection (referred to as anti-ID selection, as defined in Section 6.2.1).To obtain a correct estimation of the $N((anti-)ID/selection)$, events with a true τ_{had} are subtracted from the data events, i.e, $N = N(data) - N$ (true τ_{had} , MC). The fake factor for a given source is calculated in its dedicated background-enriched control regions, and then fake factors calculated in different regions are combined and used to normalize the fake-τ_{had} background events distributions from the anti-ID selection to the ID selection.

The fake factors are derived separately for the SLT and LTT channels. Due to the different origins of the $fake - \tau_{had}$, the FFs are calculated separately for the $t\bar{t}$ and multi-jet, and also separately for 1 and 3-prong τ_{had} candidates as we can see in Figure 4.7. The fake factor is parameterized in bins of p_T of the τ_{had} , while the dependence on η is also checked, but no obvious trend is observed.

The dedicated control region for each source is referred to as FF-CR. The FF-CR for each process is defined as follows:

- $t\bar{t}$ FF-CR: same selection as the ID/anti-ID selection but with m_{bb} cut reversed: $m_{bb} > 150$ GeV.
- Multi-jet FF-CR: same selection as the ID/anti-ID selection but with lepton isolation requirements reversed: tight electrons and 'medium' muons are required to fail their respective loose isolation working points.

The combined fake factor is determined using the fake factors calculated in the individual FF-CRs, defined as:

$$FF_{comb} = FF_{QCD} \times r_{QCD} + FF_{multi-jet} \times (1 - r_{QCD}) \tag{6.2}$$

where the $FF(multi - jet)$ (FF($t\bar{t}$)) is the fake factor calculated in the multi-jet ($t\bar{t}$) FF-CR. The value of r_{QCD} is defined as the fraction of multi-jet fakes in the total number of fake-τ_{had} background. It is measured as a function of the τ_{had} p_T , split into 1-prong and 3-prong, and into the type of light lepton (e or μ) since an electron is more easily mis-indentified as a jet than a muon. r_{QCD} is measured for events passing the anti-ID selection as:

$$r_{QCD} = \frac{\textbf{N (multi-jet, data)}}{\textbf{N (data) - N(true}\tau_{had}\textbf{, MC)}} \tag{6.3}$$

where the $N(multi-jet, data)$ is calculated by subtracting all backgrounds contributions apart from multi-jet, regardless of whether they contain fake or $true - \tau_{had}$ candidates, from the data in the $anti - \tau_{had}$ selection:

$$\textbf{N (multi-jet, data)} = \textbf{N (data) - N (true}\tau_{had}, MC) - \textbf{N (fake}\tau_{had}, MC) \tag{6.4}$$

The subtracted backgrounds are taken from the MC predictions, and the MC simulated fake background has solely the contribution from the $t\bar{t}$ fakes. In graphical form, the various FF-CRs where the fake factors are measured and applied can be seen in Figure 6.4

6.3.1 $t\bar{t}$ background

The determination of the combined fake factor is sensitive to the modeling of simulated $t\bar{t}$ events with true$-\tau_{had}$ given that this is the dominant background that is subtracted from data in the derivation of the fake factors and r_{QCD}. The $t\bar{t}$ modeling also affects the fake background estimation in the SR, since the fake factor is applied to the anti-ID events where

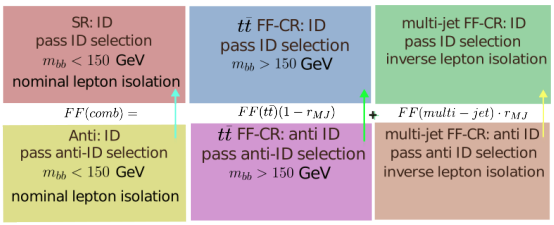

Figure 6.4: Graphical representation of the fake factor method. The fake factors are calculated independently for the $t\bar{t}$ FF-CR and the multi-jet FF-CR, and the combined fake factor is calculated using these fake factors and the value of r_{QCD} . The direction of the arrow indicates the direction of extrapolation, that the fake factor is applied on the bottom regions to extrapolate to the top regions.

the true−τ_{had} $t\bar{t}$ background is subtracted from. It was observed that mis-modeling in the true $t\bar{t}$ background, especially in the high jet multiplicity and high top-quark p_T regions can cause issues in the calculation of the fake factors, giving non-physical negative values in the high τ_{had} p_T region. To solve this problem, simulated events from $t\bar{t}$ production are differently re-weighted depending on the jet multiplicity and the scalar sum of the transverse momentum of all visible final state objects (HT) in the event. These re-weighting factors are determined bin-by-bin in distribution of jet multiplicity and HT , from another $t\bar{t}$ FF-CR, $t\bar{t}$ FF-CR2, which is defined using a selection identical to the SR selection, but with the $t\bar{t}$ FF-CR m_{bb} requirements ($m_{bb} > 150$ GeV). and an additional $m_T^W > 40$ GeV requirement.

6.3.2 Control region purity

The fake background is simulated by MC, and it only includes the contributions from the $t\bar{t}$ initiated fakes. A clear miss-modeling can be seen in the study before the fakes factors are applied, and it is much mitigated after what we can appreciate in the ratio plot of 7.1 and 7.2. At this stage, data and MC are not expected to agree well due to the $t\bar{t}$ fake is known to be poorly modeled by the MC, which is also the main reason for using the data-driven fake factor method. Nevertheless, a large number of $t\bar{t}$ fakes is observed, suggesting the high purity of $t\bar{t}$ fakes in this region. With true τ_{had} contributions subtracted from the data (and with true τ_{had} $t\bar{t}$ re-weighted), events in this region are used in $t\bar{t}$ FF-CR fake factor calculation (as the denominator).

The multi-jet control regions (MJ CRs) and $t\bar{t}$ control regions ($t\bar{t}$ CRs) are defined separately for the ID and the anti-ID regions, depending on whether they contain one identified $\tau_{had-vis}$ or one anti-$\tau_{had-vis}$ candidate, respectively. Besides the $\tau_{had-vis}$ selection, the MJ CRs are defined using the SR selection with an inverted electron or muon isolation requirement (anti-Iso) and without the $m_{bb} < 150GeV$ requirement 6.2.2. The MJ CR's purity in multi-jet production events varies depending on the trigger category type (SLT or LTT) and whether the MJ CR is in the ID or anti-ID region. Similarly, the $t\bar{t}$ CRs are defined using the SR selection with an inverted m_{bb} requirement ($m_{bb} > 150$ GeV) 6.3.1.

To demonstrate the purity of the desired backgrounds in the $t\bar{t}$ CR and MJ CR, distributions of the τ p_T for the control regions with the τ_{had} and anti-τ_{had} requirements, separately for 1-prong and 3-prong τ_{had} are included. These distributions can be seen in Figure 6.3.2 and Figure 6.3.2

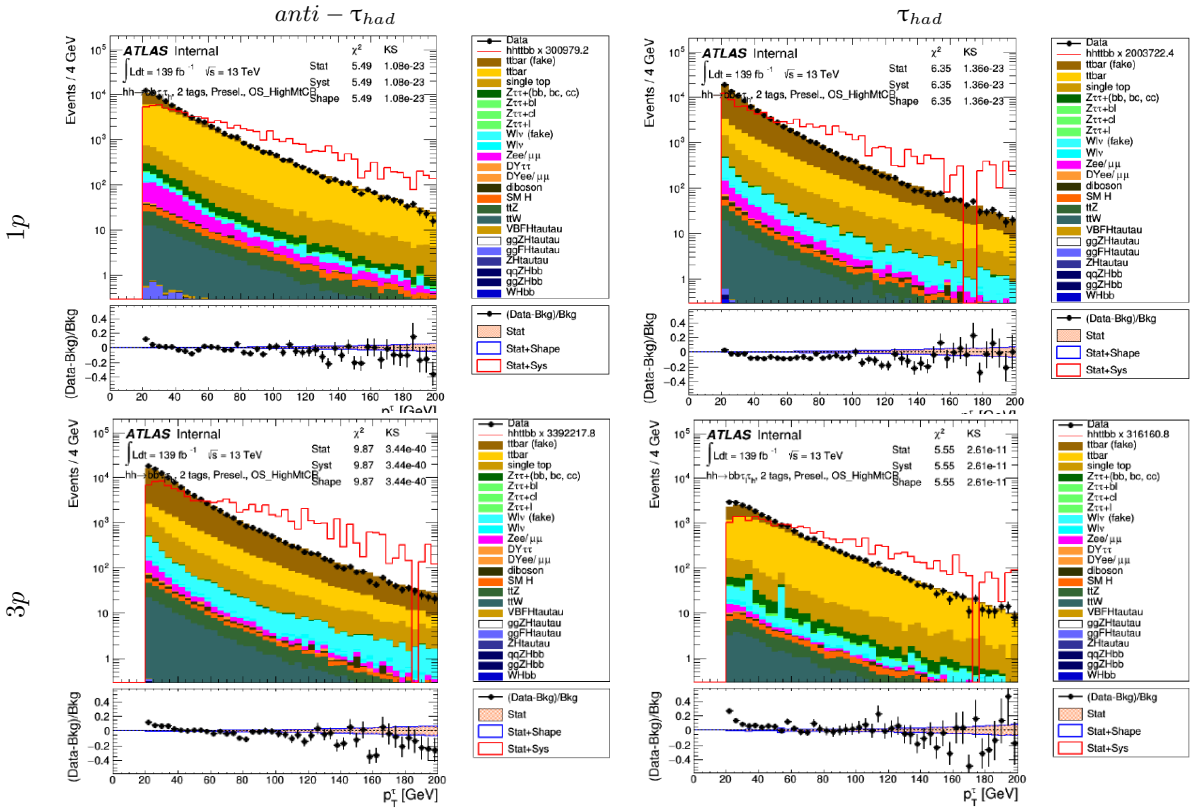

Table 6.5: Plots of the τ_{had} p_T distributions for the anti-τ_{had} and τ_{had} selection (first and second column) for the SLT and in the $t\bar{t}$ control region with 1-prong and 3-prong .

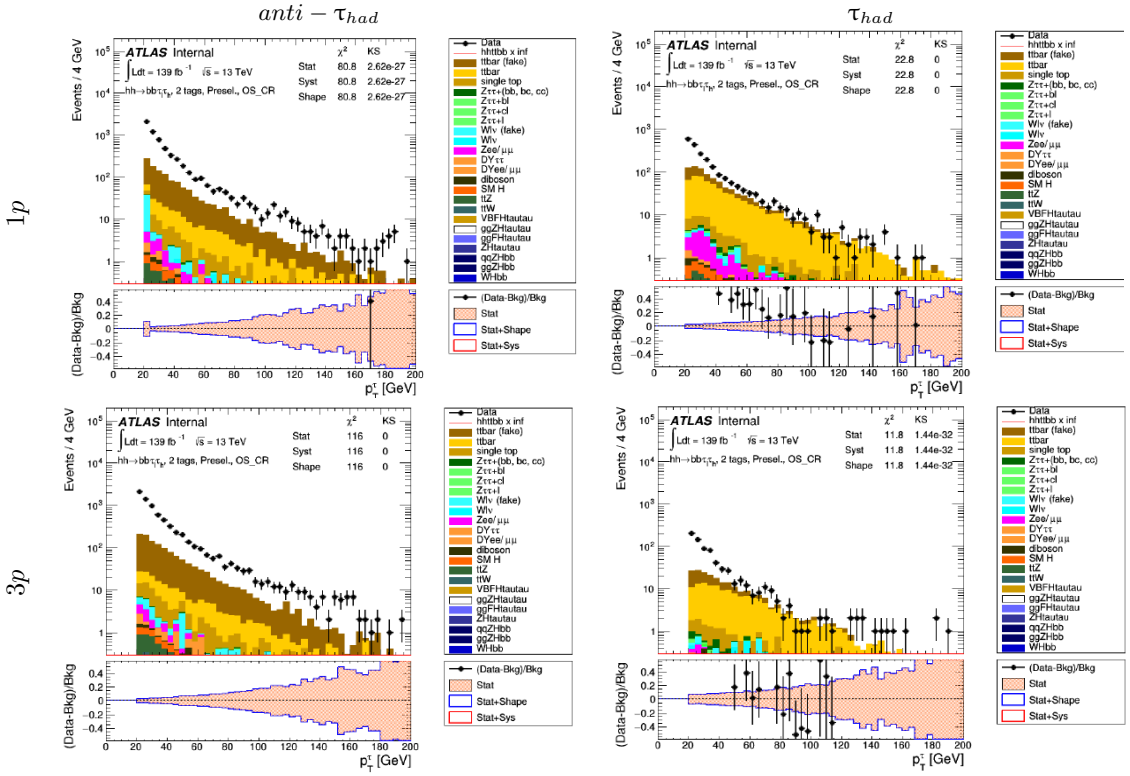

Table 6.6: Plots of the τ_{had} p_T distributions for the anti-τ_{had} and τ_{had} selection (first and second column) for the SLT and in the multi-jet control region with 1-prong and 3-prong .

6.3.3 Fake factor method validation

The combined FF method is validated in two regions 0b-tag in Figure 6.5a and 1b-tag in Figure 6.5b, these regions have the same event selection as the SR is applied, however, the number of b-tagged jets required it is different. The fakes factors use in the validation regions name before (0b and 1b-tag) are estimated with FF calculated in each validation region with the same method used in the signal regions (2b-tagged). These two validation regions are chosen as the signal contamination in the 0b-tagged and 1b-tagged regions is negligible, and the 0b-tagged region can benefit from its rich statistics, and the 1b-tagged region from being closer to the SR. The estimated background distributions agree well with the observed distributions in all validation regions.

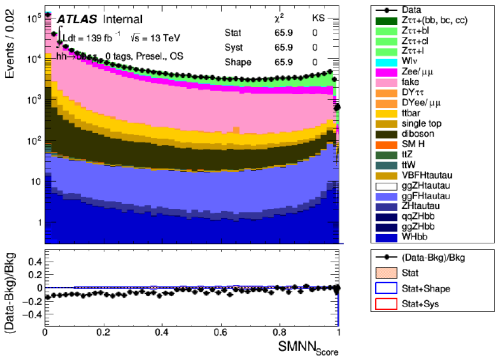

(a) 0b-tag validation region

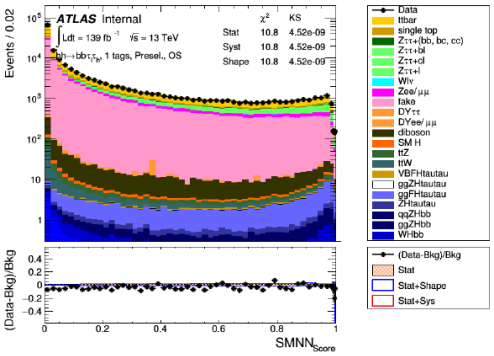

(b) 1b-tag validation region

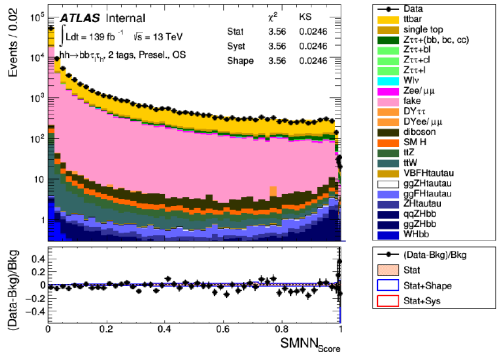

(c) Closure test

Figure 6.5: The upper plots show the non-resonant NN distribution in the 0b-tag and 1b-tag validation region of the SLT category. At the bottom we have the non-resonant NN distribution in the signal-depleted $t\bar{t}$ CR where the $t\bar{t}$ FF are measured. This is the closure test.

Now let us compare the Fake Factors calculated from two different sources. From Monte Carlo and using the Data-Driven method in the validation region for the different criteria used to separate the Signal region.

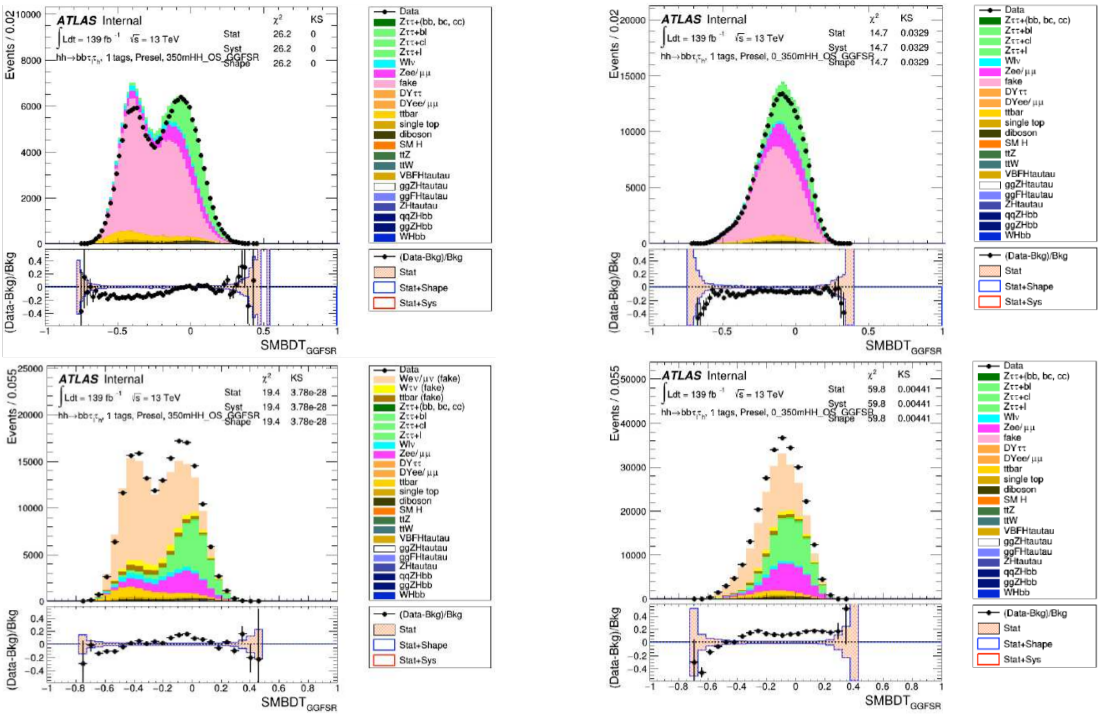

Figure 6.6: Fake Tau Estimation in Validation region comparison for BDT in low and High ggF region. The DATA/MC comparison looks better in the case where the Fakes Factor were calculated using the Data-Driven method compared to case the where they are only estimated using the Monte Carlo simulations. And we can see the ratio plot has better result with the method used in this analysis. This is result of using the data to estimate the modeling correction factors. The MC fakes are not well model from W+jets background, which accounts for the discrepancies between the simulation and data.

Chapter 7

Results

7.1 Final Results: Applying the Fakes to the Preselection_lowMbb150

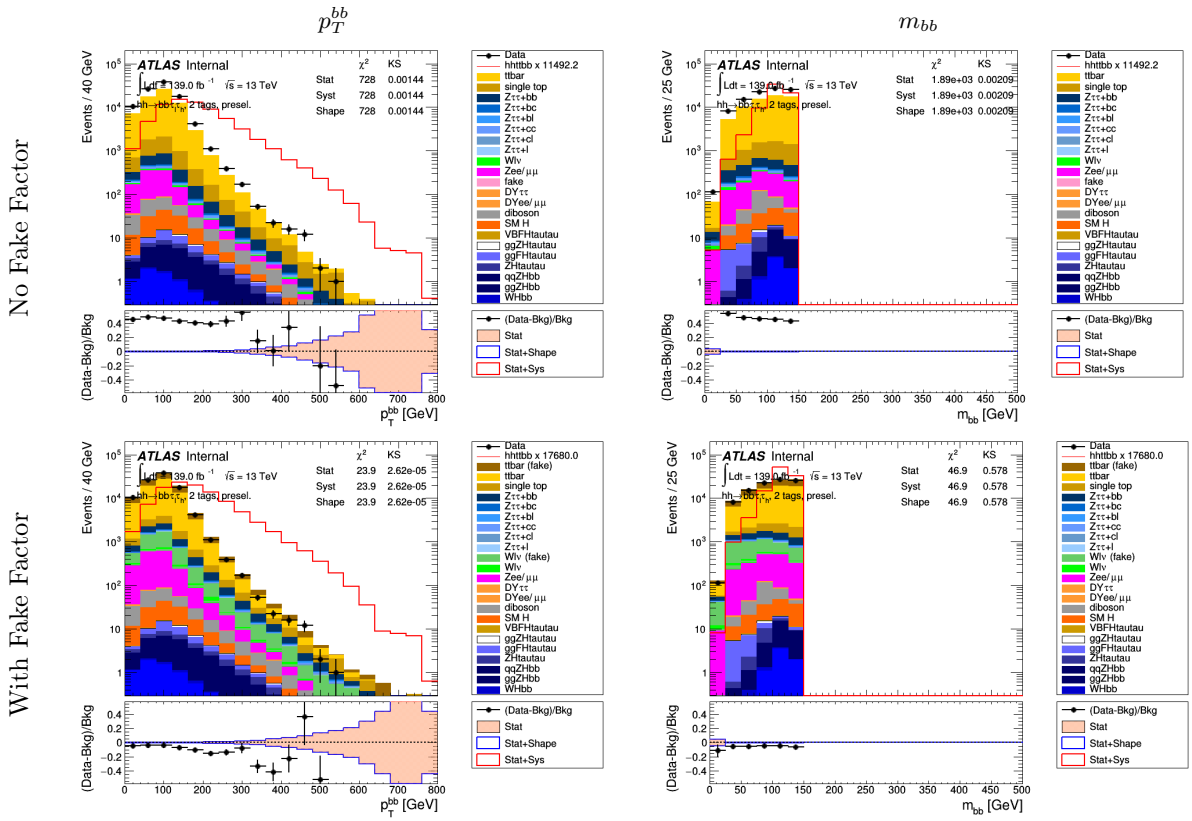

7.2 Final Results: Applying the Fakes to the Preselection_HighMbb150

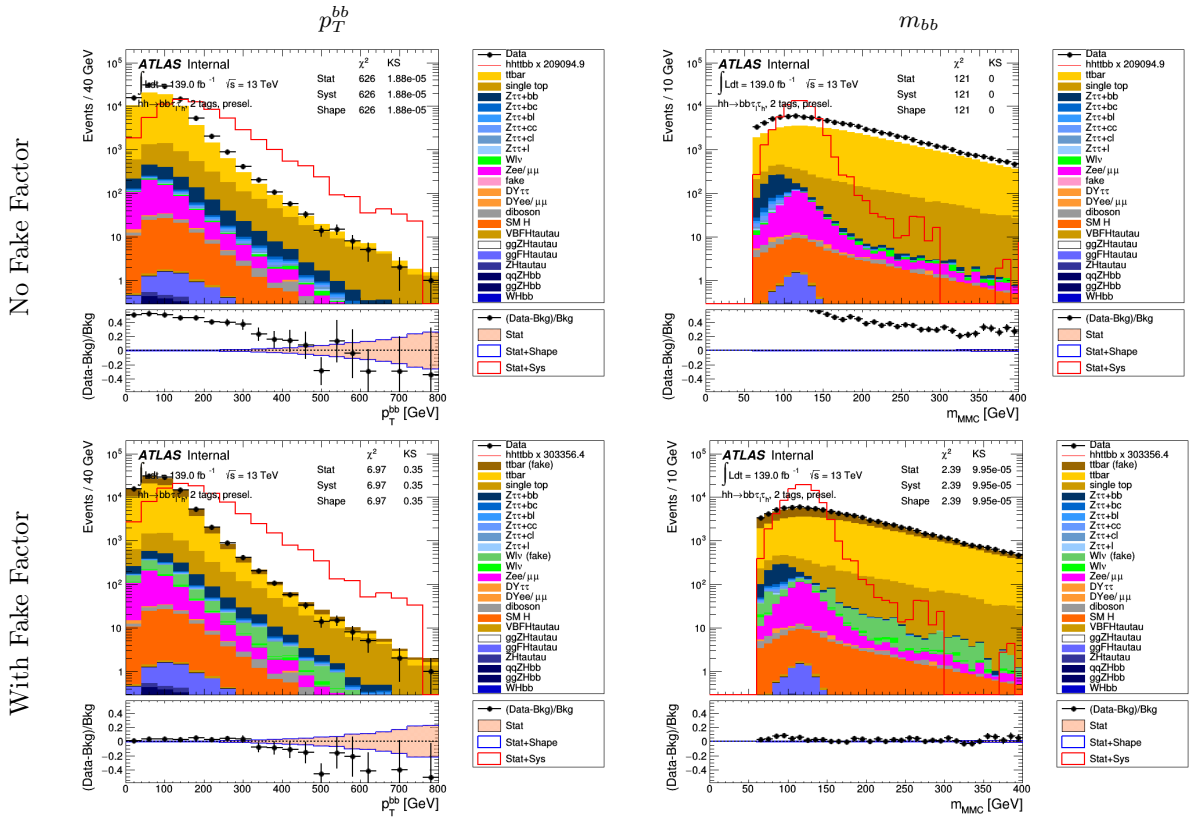

We have applied the Fake Factors Derived from the Data Driven method. And applied them to the two Signal regions for Low and High M_{bb} like was discuss in the 5.3. As we can see the ratio plot and the background adjust better after we applied them. In order to know this shows a better results we compare the DATA/MC has a better agreement that with the Fake Factor derived from Monte Carlo only as we can see in Figure 6.6 were the Stander Model BDT was plotted. And the Fake Factors were calculate from two different ways using the current Data Driven method and calculating these factors from the Monte Carlos simulation only. The MC fakes are from show large miss-modeling due to W+jets events are and the fakes taus which are not well model by the simulations. This give us a an other reason to use the Data Driven method in the derivation of these factors instead of calculating them just from simulation. For this the data-driven technique show better results as we can see on the figures on Tables 7.1 and 7.2.

7.3 Conclusion

In this thesis, two main tasks were conducted. One was the migration of the frameworks to validate the calculation of the fakes factors with the new frameworks against the old framework (MIA). And to calculate and apply new Fakes Factors with a Data-Driven method to different signals regions define in this analysis diveded by trigger selection and channel decay.

In regard to the first aspect the implementation of the migration of the two frameworks is fine as the results were verify to match the result obtain from our former framework (MIA).

The second task was to calculate the fakes from this new Method applied them to the signal region and validation of this result shows a good match in the Data and Monte ratio plots. The Backgrounds in this search are estimated using a combination of simulation-based and data-driven techniques. The main sources of background are top-quark, W+jets, Z+jets, diboson, single Higgs boson, and multi-jet production. A reconstructed $\tau_{had-vis}$, in these background

events, can originate either from a τ_{had} decay (true-$\tau_{had-vis}$), or from a misidentified quark- or gluon-initiated jet (fake-$\tau_{had-vis}$). Events in which an electron or a muon is misidentified as a $\tau_{had-vis}$ represent a small additional background.

Data and Monte Carlo are not expected to agree well due to the $t\bar{t}$ fake is known to be poorly modelled by the MC, and $t\bar{t}$ constitute the larger background in this analysis, which is also one of the big motivators to use the data-driven fake factor method. As we could see the plots in the ID and Anti-ID in our control regions.

For the closure test distributions the DATA/MC comparison has a better agreement than the Monte Carlo fakes. For the 0b-tag validation region the backgrounds is slightly overestimated because this region is far distinct from our signal region, which has 2b-tagged jets. Therefore for the closer Test we are only taking 1b-tagged region as Validation region.

Finally, estimating fake factors using data-driven methods can be more accurate than calculating this factors from Monte Carlo simulations for several reasons:

- The Data-driven method relies on actual measurements, rather than simulated models. This implies that the factors calculated from the data-driven method are less prone to biases and systematic errors that may be present in Monte Carlo simulations.
- Data-driven methods can account for correlations between different sources of fake contributions in a more realistic way. For example, they can take into account the fact that two different variables or processes, like the control regions may both contribute to fakes, but that their correlation may affect the overall level of the fake background.
- Data-driven methods can often provide more accurate estimates of uncertainties. Monte Carlo simulations can suffer from limited statistics and uncertainties associated with theoretical models used to simulate the background events. In contrast, data-driven methods can often use large data sets to precisely estimate the uncertainty on the fake factors.

In conclusion, while Monte Carlo simulations can be a useful tool for estimating fake backgrounds, data-driven methods can often provide more reliable estimates that are less prone to biases and systematic errors.

Chapter 8

Appendix: BDT Variables: Comparison between Fakes Factors and no Fakes applied

8.1 Preselection_LowMbb150

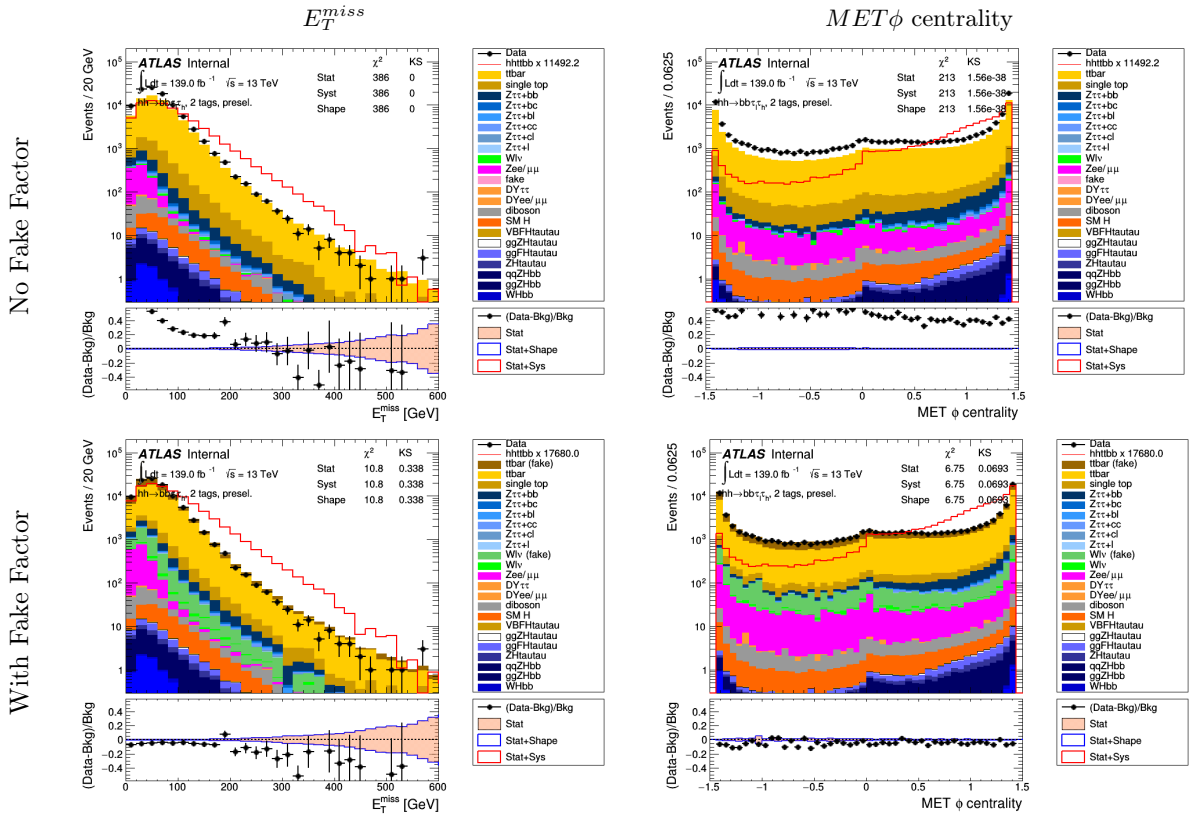

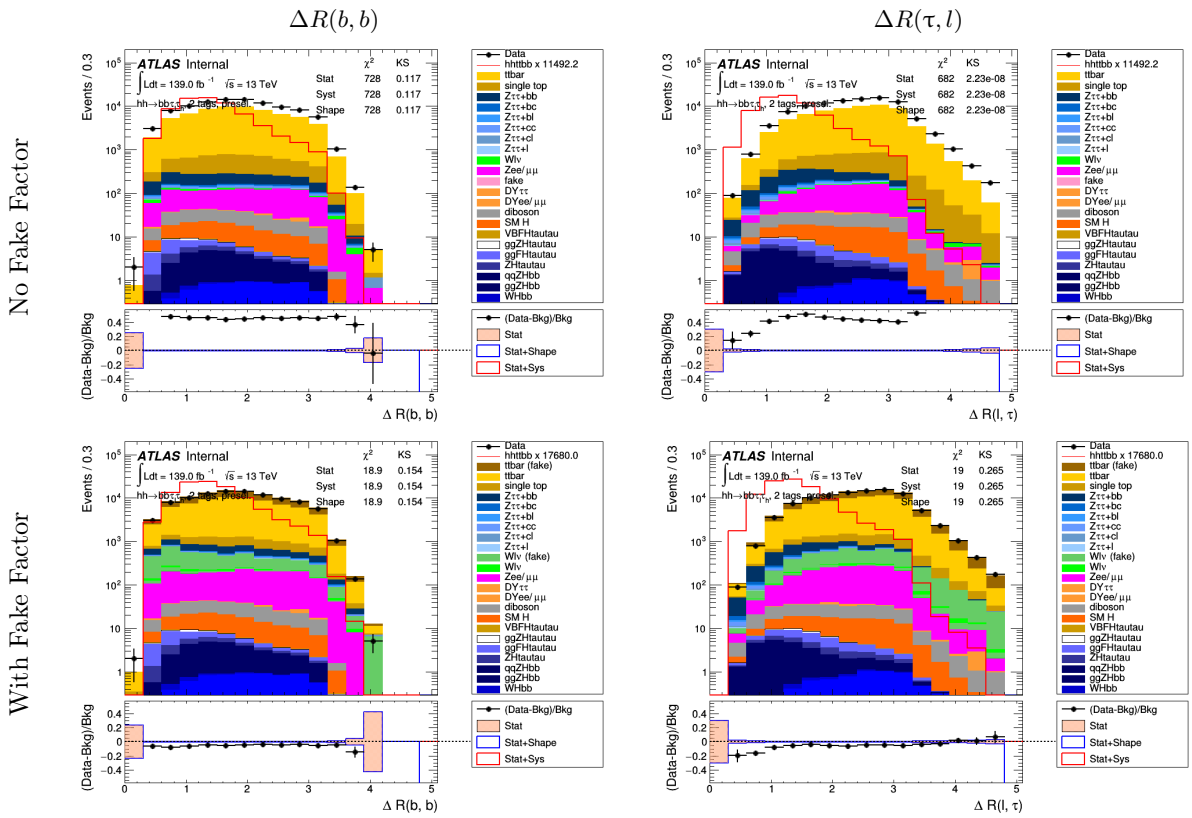

8.2 Preselection_HighMbb150

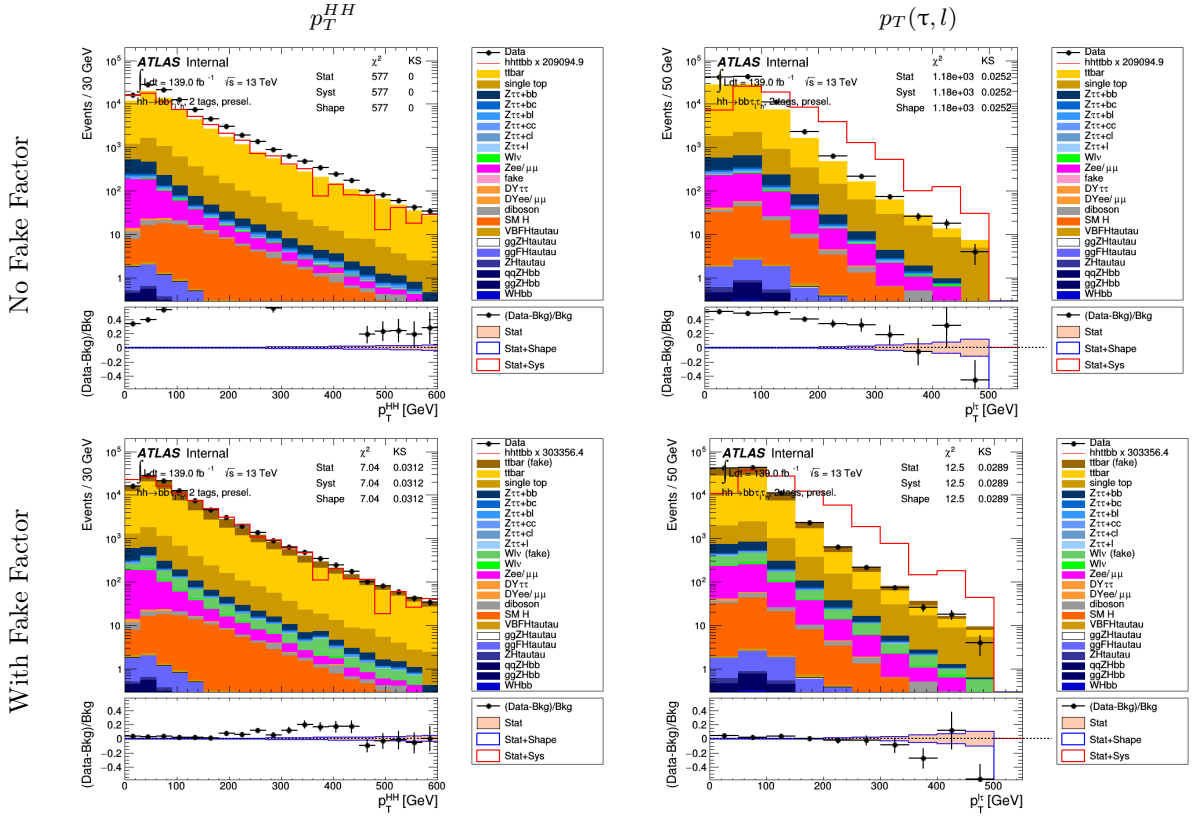

$\Delta R(b,b)$ $\Delta R(\tau,l)$

No Fake Factor

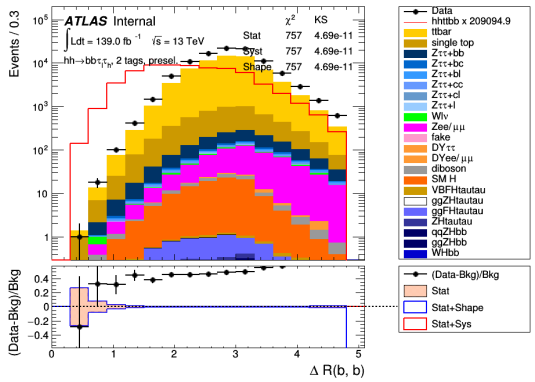

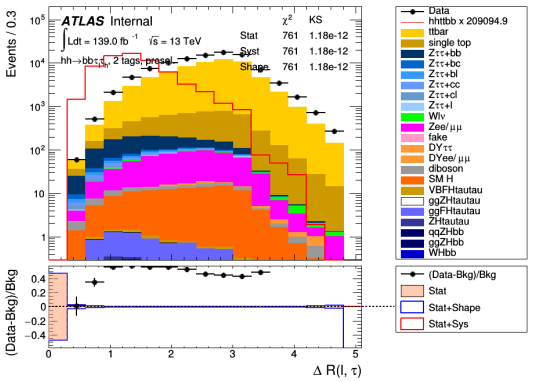

With Fake Factor

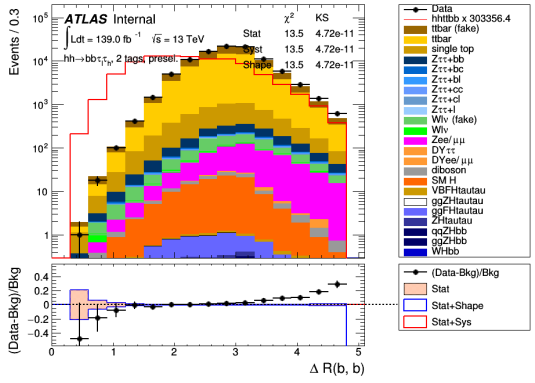

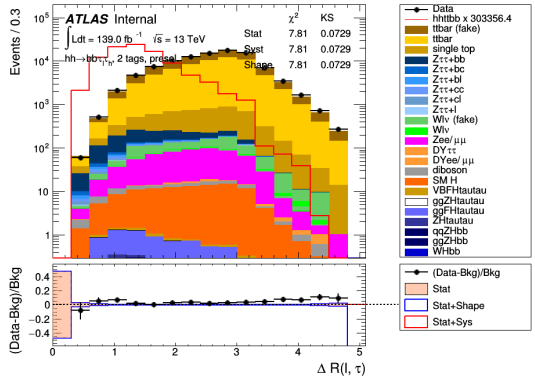

Bibliography

[20115] Identification and energy calibration of hadronically decaying tau leptons with the atlas experiment in pp collisions at $\sqrt{s} = 8$ TeV tev. The European Physical Journal C, 75(7), Jul 2015.

[20116] Performance ofb-jet identification in the atlas experiment. Journal of Instrumentation, 11(04):P04008–P04008, Apr 2016.

[A+99] A. Airapetian et al. ATLAS: Detector and physics performance technical design report. Volume 1. 5 1999.

[A+08] E. Abat et al. The ATLAS TRT barrel detector. JINST, 3:P02014, 2008.

[A+18] Morad Aaboud et al. Measurement of the W-boson mass in pp collisions at $\sqrt{s} = 7$ TeV with the ATLAS detector. feb 2018.

[AA+12] Georges Aad, Abajyan, et al. Observation of a new particle in the search for the Standard Model Higgs boson with the ATLAS detector at the LHC. Observation of a new particle in the search for the Standard Model Higgs boson with the ATLAS detector at the LHC. Phys. Lett. B, 716:1–29. 29 p, Sep 2012. Comments: 24 pages plus author list (38 pages total), 12 figures, 7 tables, revised author list.

[AAA+83] G. Arnison, A. Astbury, B. Aubert, C. Bacci, G. Bauer, A. Bézaguet, R. Böck, T.J.V. Bowcock, M. Calvetti, T. Carroll, P. Catz, P. Cennini, S. Centro, F. Ceradini, S. Cittolin, D. Cline, C. Cochet, J. Colas, M. Corden, D. Dallman, M. DeBeer, M. Della Negra, M. Demoulin, D. Denegri, A. Di Ciaccio, D. DiBitonto, L. Dobrzynski, J.D. Dowell, M. Edwards, K. Eggert, E. Eisenhandler, N. Ellis, P. Erhard, H. Faissner, G. Fontaine, R. Frey, R. Frühwirth, J. Garvey, S. Geer, C. Ghesquière, P. Ghez, K.L. Giboni, W.R. Gibson, Y. Giraud-Héraud, A. Givernaud, A. Gonidec, G. Grayer, P. Gutierrez, T. Hansl-Kozanecka, W.J. Haynes, L.O. Hertzberger, C. Hodges, D. Hoffmann, H. Hoffmann, D.J. Holthuizen, R.J. Homer, A. Honma, W. Jank, G. Jorat, P.I.P. Kalmus, V. Karimäki, R. Keeler, I. Kenyon, A. Kernan, R. Kinnunen, H. Kowalski, W. Kozanecki, D. Kryn, F. Lacava, J.-P. Laugier, J.-P. Lees, H. Lehmann, K. Leuchs, A. Léveque, E. Linglin, E. Locci, M. Loret, J.-J. Malosse, T. Markiewicz, G. Maurin, T. McMahon, J.-P. Mendiburu, M.-N. Minard, M. Moricca, H. Muirhead, F. Muller, A.K. Nandi, L. Naumann, A. Norton, A. Orkin-Lecourtois, L. Paoluzi, G. Petrucci, G.Piano Mortari, M. Pimiä, A. Placci, E. Radermacher, J. Ransdell, H. Reithler, J.-P. Revol, J. Rich, M. Rijssenbeek, C. Roberts, J. Rohlf, P. Rossi, C. Rubbia, B. Sadoulet, G. Sajot, G. Salvi, J. Salvini, J. Sass, A. Saudraix, A. Savoy-Navarro, D. Schinzel, W. Scott, T.P. Shah, M. Spiro, J. Strauss, K. Sumorok, F. Szoncso, D. Smith, C. Tao, G. Thompson, J. Timmer, E. Tscheslog, J. Tuominiemi, S. Van der Meer, J.-P. Vialle, J. Vrana, V. Vuillemin, H.D. Wahl, P. Watkins, J. Wilson, Y.G. Xie, M. Yvert, and E. Zurfluh. Experimental observation of isolated large transverse energy electrons with associated missing energy at s=540 gev. Physics Letters B, 122(1):103–116, 1983.

[AAA+16] Georges Aad, B Abbott, J Abdallah, B Abeloos, R Aben, M Abolins, OS AbouZeid, NL Abraham, H Abramowicz, H Abreu, et al. Muon reconstruction performance of the atlas detector in proton–proton collision data at $\sqrt{=}13$ tev. The European Physical Journal C, 76(5):292, 2016.

[Atk15] Ryan Atkin. Review of jet reconstruction algorithms. Journal of Physics: Conference Series, 645(1):012008, sep 2015.

[ATL15] Reconstruction, Energy Calibration, and Identification of Hadronically Decaying Tau Leptons in the ATLAS Experiment for Run-2 of the LHC. Technical report, CERN, Geneva, Nov 2015. All figures including auxiliary figures are available at https://atlas.web.cern.ch/Atlas/GROUPS/PHYSICS/PUBNOTES/ATL-PHYS-PUB-2015-045.

[ATL16] Optimisation of the ATLAS b-tagging performance for the 2016 LHC Run. Technical report, CERN, Geneva, 2016. All figures including auxiliary figures are available at https://atlas.web.cern.ch/Atlas/GROUPS/PHYSICS/PUBNOTES/ATL-PHYS-PUB-2016-012.

[ATL19] ATLAS. Measurements of the Higgs boson inclusive, differential and production cross sections in the 4ℓ decay channel at $\sqrt{s}$ = 13 TeV with the ATLAS detector. Technical report, CERN, Geneva, 2019. All figures including auxiliary figures are available at https://atlas.web.cern.ch/Atlas/GROUPS/PHYSICS/CONFNOTES/ATLAS-CONF-2019-025.

[ATL21] Search for resonant and non-resonant Higgs boson pair production in the $b\bar{b}\tau^+\tau^-$ decay channel using 13 TeV pp collision data from the ATLAS detector. Technical report, CERN, Geneva, 2021. All figures including auxiliary figures are available at https://atlas.web.cern.ch/Atlas/GROUPS/PHYSICS/CONFNOTES/ATLAS-CONF-2021-030.

[B$^+$13] Baglio et al. Journal of High Energy Physics, apr 2013.

[BBB$^+$83] M. Banner, R. Battiston, Ph. Bloch, F. Bonaudi, K. Borer, M. Borghini, J.-C. Chollet, A.G. Clark, C. Conta, P. Darriulat, L. Di Lella, J. Dines-Hansen, P.-A. Dorsaz, L. Fayard, M. Fraternali, D. Froidevaux, J.-M. Gaillard, O. Gildemeister, V.G. Goggi, H. Grote, B. Hahn, H. Hänni, J.R. Hansen, P. Hansen, T. Himel, V. Hungerbühler, P. Jenni, O. Kofoed-Hansen, E. Lançon, M. Livan, S. Loucatos, B. Madsen, P. Mani, B. Mansoulie, G.C. Mantovani, L. Mapelli, B. Merkel, M. Mermikides, R. Møllerud, B. Nilsson, C. Onions, G. Parrour, F. Pastore, H. Plothow-Besch, M. Polverel, J.-P. Repellin, A. Rothenberg, A. Roussarie, G. Sauvage, J. Schacher, J.L. Siegrist, H.M. Steiner, G. Stimpfl, F. Stocker, J. Teiger, V. Vercesi, A. Weidberg, H. Zaccone, and W. Zeller. Observation of single isolated electrons of high transverse momentum in events with missing transverse energy at the cern pp collider. Physics Letters B, 122(5):476–485, 1983.

[BBB$^+$20] Alessandra Betti, Adrian John Bevan, Petar Bokan, Edson Carquin, Allison McCarn Deiana, Christopher Deutsch, Jochen Dingfelder, Marisilvia Donadelli, Arnaud Ferrari, Kathryn Grimm, Carl Gwilliam, Natasha Domenica Hehir, Pawel Klimek, Stanley Lai, Katharine Leney, Tatjana Lenz, Zhiyuan Li, Andres Hugo Melo, Konstantinos Nikolopoulos, Adam Jackson Parker, Serban Protopopescu, Elliot Reynolds, Nikolaos Rompotis, Puja Saha, Tulin Varol Mete, Song-Ming Wang, Shahzad Ali, Thomas Andrew Schwarz, Jem Aizen Mendiola Guhit, Yanlin Liu, Bowen Zhang, Lei Zhang, Rodrigo Gamboa Goni, Shenjian Chen, Panagiotis Bellos, and Nicholas Luongo. Searches for Higgs boson pair production in the $b\bar{b}\tau^+\tau^-$ final state with 139 fb^{-1} of pp collision data with the ATLAS detector. Technical report, CERN, Geneva, 2020.

[BBBB97] J P Badiou, J Beltramelli, J M Baze, and J Belorgey. ATLAS barrel toroid: Technical Design Report. Technical design report. ATLAS. CERN, Geneva, 1997. Electronic version not available.

[BCLT10] W. Bentz, I. C. Cloet, J. T. Londergan, and A. W. Thomas. Reassessment of the NuTeV determination of the weak mixing angle. Phys. Lett. B, 693:462–466, 2010.

[BDWW16] Giles Barr, Robin Devenish, Roman Walczak, and Tony Weidberg. Particle physics in the LHC era. Oxford master series in particle physics, astrophysics, and cosmology. Oxford University Press, Oxford, 2016.

[BGH$^+$16] S Borowka, N Greiner, G Heinrich, SP Jones, M Kerner, J Schlenk, U Schubert, and T Zirke. Higgs boson pair production in gluon fusion at next-to-leading order with full top-quark mass dependence. Physical Review Letters, 117(1):012001, 2016.

[Bha11] Pushpalatha C. Bhat. Multivariate Analysis Methods in Particle Physics. Ann. Rev. Nucl. Part. Sci., 61:281–309, 2011.

[BSG13] G. Borowka S. Greiner, N. Heinrich. Full top quark mass dependence in higgs boson pair production at nlo. j. high energ. phys. 2016, 107 (2016). 2013.

[C+12] Chatrchyan et al. Observation of a new boson at a mass of 125 GeV with the CMS experiment at the LHC. Observation of a new boson at a mass of 125 GeV with the CMS experiment at the LHC. Phys. Lett. B, 716:30–61, 2012.

[Cab63] Nicola Cabibbo. Unitary symmetry and leptonic decays. Phys. Rev. Lett., 10:531–533, Jun 1963.

[CCFT64] J. H. Christenson, J. W. Cronin, V. L. Fitch, and R. Turlay. Evidence for the 2π Decay of the K_2^0 Meson. Phys. Rev. Lett., 13:138–140, 1964.

[CDE+10] M Capeans, G Darbo, K Einsweiller, M Elsing, T Flick, M Garcia-Sciveres, C Gemme, H Pernegger, O Rohne, and R Vuillermet. ATLAS Insertable B-Layer Technical Design Report. Technical report, 2010.

[CER97] ATLAS inner detector: Technical Design Report, 1. Technical design report. ATLAS. CERN, Geneva, 1997.

[CF12] Giovanni Costa and Gianluigi Fogli. Symmetries and group theory in particle physics., volume 823. Springer, 2012.

[CMS18] CMS. Measurements of properties of the Higgs boson in the four-lepton final state at $\sqrt{s} = 13$TeV. Technical report, CERN, Geneva, 2018.

[CMS19] CMS. Measurements of Higgs boson production via gluon fusion and vector boson fusion in the diphoton decay channel at $\sqrt{s} = 13$ TeV. Technical report, CERN, Geneva, 2019.

[Col08a] "ALICE Collaboration". "the alice experiment at the cern lhc". "JINST", "3":"S08002. 259 p", "2008". "Also published by CERN Geneva in 2010".

[Col08b] LHCb Collaboration. The LHCb Detector at the LHC. JINST, 3:S08005, 2008. Also published by CERN Geneva in 2010.

[Col10] Atlas Collaboration. The ATLAS Simulation Infrastructure. The European Physical Journal C, 270(3):2823–874, sep 2010.

[Col12] ATLAS Colaboration. Observation of a new particle in the search for the standard model higgs boson with the ATLAS detector at the LHC. Physics Letters B, 716(1):1–29, sep 2012.

[Col13a] ATLAS Collaboration. Evidence for the spin-0 nature of the higgs boson using atlas data. Physics Letters B, 726(1):120–144, 2013.

[Col13b] ATLAS Collaboration. Jet energy resolution in proton-proton collisions at $\sqrt{s} = 7$ TeV recorded in 2010 with the ATLAS detector. Jet energy resolution in proton-proton collisions at sqrt(s) = 7 TeV recorded in 2010 with the ATLAS detector. Eur. Phys. J. C, 73:2306, 2013. Comments: 13 pages plus author list (26 pages total), 15 figures, 1 table, submitted to European Physical Journal C.

[Col15a] ATLAS Collaboration. Combined measurement of the higgs boson mass in *pp* collisions at $\sqrt{s} = 7$ and 8 tev with the atlas and cms experiments. 114, May 2015.

[Col15b] ATLAS Collaboration. Measurements of higgs boson production and couplings in the four-lepton channel in *pp* collisions at center-of-mass energies of 7 and 8 tev with the atlas detector. Phys. Rev. D, 91:012006, Jan 2015.

[Col16a] ATLAS Collaboration. Performance of b-jet identification in the atlas experiment. Journal of Instrumentation, 11(04):P04008, apr 2016.

[Col16b] ATLAS Collaboration. Performance of *b*-Jet Identification in the ATLAS Experiment. Performance of *b*-Jet Identification in the ATLAS Experiment. JINST, 11:P04008, 2016. 111 pages plus author list + cover page (128 pages total), 55 figures, 17 tables, submitted to JINST, All figures including auxiliary figures are avail-

able at http://atlas.web.cern.ch/Atlas/GROUPS/PHYSICS/PAPERS/PERF-2012-04/.

[Col17a] ATLAS Collaboration. Jet energy scale measurements and their systematic uncertainties in proton-proton collisions at $\sqrt{s} = 13$ TeV with the ATLAS detector. Jet energy scale measurements and their systematic uncertainties in proton-proton collisions at $\sqrt{s} = 13$ TeV with the ATLAS detector. Phys. Rev. D, 96(7):072002, 2017. 51 pages in total, author list starting page 35, 15 figures, 1 table, submitted to Phys. Rev. D., all figures including auxilary figures are available at https://atlas.web.cern.ch/Atlas/GROUPS/PHYSICS/PAPERS/PERF-2016-04/.

[Col17b] Atlas Collaboration. Performance of the ATLAS Track Reconstruction Algorithms in Dense Environments in LHC run 2. Performance of the ATLAS Track Reconstruction Algorithms in Dense Environments in LHC run 2. Eur. Phys. J. C, 77(10):673, 2017. 44 pages in total, author list starting page 28, 17 figures, 1 table, submitted to EPJC, All figures including auxiliary figures are available at http://atlas.web.cern.ch/Atlas/GROUPS/PHYSICS/PAPERS/PERF-2015-08/.

[Col19] ATLAS Collaboration. Cross-section measurements of the higgs boson decaying into a pair of mml:math xmlns:mml="http://www.w3.org/1998/math/MathML". Physical Review D, 99(7), apr 2019.

[cp96] ATLAS calorimeter performance. ATLAS calorimeter performance: Technical Design Report. Technical design report. ATLAS. CERN, Geneva, 1996.

[cs97] ATLAS central solenoid. ATLAS central solenoid: Technical Design Report. Technical design report. ATLAS. CERN, Geneva, 1997. Electronic version not available.

[CSS08a] Matteo Cacciari, Gavin P. Salam, and Gregory Soyez. The anti-kt jet clustering algorithm. Journal of High Energy Physics, 2008(04):063, apr 2008.

[CSS08b] Matteo Cacciari, Gavin P Salam, and Gregory Soyez. The anti-ktjet clustering algorithm. Journal of High Energy Physics, 2008(04):063–063, Apr 2008.

[dF+17] de Florian et al. Handbook of LHC Higgs Cross Sections: 4. Deciphering the Nature of the Higgs Sector. CERN Yellow Reports: Monographs. CERN, Geneva, 2017. 869 pages, 295 figures, 248 tables and 1645 citations. Working Group web page: https://twiki.cern.ch/twiki/bin/view/LHCPhysics/LHCHXSWG.

[EB64] François Englert and Robert Brout. Broken symmetry and the mass of gauge vector mesons. Physical Review Letters, 13:321–323, 1964.

[EC21a] ATLAS Experiment and CERN. The atlas detector. 2021. Online; Last access 27-02-2021.

[EC21b] ATLAS Experiment and CERN. Trigger and data acquisition, 2021. Online; Last access 27-02-2021.

[ect97] ATLAS end-cap toroids. ATLAS end-cap toroids: Technical Design Report. Technical design report. ATLAS. CERN, Geneva, 1997. Electronic version not available.

[EMNN87] O JP Eboli, GC Marques, SF Novaes, and AA Natale. Twin higgs-boson production. Phys. Lett. B;(Netherlands), 197(1/2), 1987.

[ESW03] Richard Keith Ellis, William James Stirling, and Bryan R Webber. QCD and collider physics. Cambridge monographs on particle physics, nuclear physics, and cosmology. Cambridge University Press, Cambridge, 2003. Photography by S. Vascotto.

[FFH+14] R. Frederix, S. Frixione, V. Hirschi, F. Maltoni, O. Mattelaer, P. Torrielli, E. Vryonidou, and M. Zaro. Higgs pair production at the lhc with nlo and parton-shower effects. Physics Letters B, 732:142–149, 2014.

[GHK64] G. S. Guralnik, C. R. Hagen, and T. W. B. Kibble. Global Conservation Laws and Massless Particles. Phys. Rev. Lett., 13:585–587, 1964.

[Gla61] Sheldon L. Glashow. Partial-symmetries of weak interactions. Nuclear Physics, 22(4):579–588, 1961.

[GM56] M. Gell-Mann. The interpretation of the new particles as displaced charge multiplets. Nuovo Cim., 4(S2):848–866, 1956.

[Gre64] O. W. Greenberg. Spin and unitary-spin independence in a paraquark model of baryons and mesons. Phys. Rev. Lett., 13:598–602, Nov 1964.

[gro16] Trigger group. 2015 start-up trigger menu and initial performance assessment of the ATLAS trigger using Run-2 data. Technical Report ATL-DAQ-PUB-2016-001, CERN, Geneva, Mar 2016.

[Gro23] LHC Higgs Working Group. Lhc higgs cross section working group web page (2016). 02 2023.

[GSW62] Jeffrey Goldstone, Abdus Salam, and Steven Weinberg. Broken symmetries. Phys. Rev., 127:965–970, Aug 1962.

[H+07] Andreas Hocker et al. TMVA - Toolkit for Multivariate Data Analysis. 3 2007.

[Hig64a] Peter W. Higgs. Broken Symmetries and the Masses of Gauge Bosons. Phys. Rev. Lett., 13:508–509, 1964.

[Hig64b] Peter Ware Higgs. Broken symmetries, massless particles and gauge fields. Phys. Lett., 12:132–133, 1964.

[HK85] H.E. Haber and G.L. Kane. The search for supersymmetry: Probing physics beyond the standard model. Physics Reports, 117(2):75–263, 1985.

[HN65] M. Y. Han and Y. Nambu. Three-triplet model with double SU(3) symmetry. Phys. Rev., 139:B1006–B1010, Aug 1965.

[hue17] Measurement of the tau lepton reconstruction and identification performance in the ATLAS experiment using pp collisions at $\sqrt{s} = 13$ TeV. Technical Report ATLAS-CONF-2017-029, CERN, Geneva, May 2017.

[Jac05] John Neil Jackson. The ATLAS semiconductor tracker (SCT). Nucl. Instrum. Meth. A, 541:89–95, 2005.

[Kar05] Savely G. Karshenboim. Precision physics of simple atoms: QED tests, nuclear structure and fundamental constants. Physics Reports, 422(1):1–63, 2005.

[KM73] Makoto Kobayashi and Toshihide Maskawa. CP-Violation in the Renormalizable Theory of Weak Interaction. Progress of Theoretical Physics, 49(2):652–657, 02 1973.

[lac96] ATLAS liquid-argon calorimeter. ATLAS liquid-argon calorimeter: Technical Design Report. Technical design report. ATLAS. CERN, Geneva, 1996.

[Lee73] T. D. Lee. A theory of spontaneous t violation. Phys. Rev. D, 8:1226–1239, Aug 1973.

[Lee15] Claire A Lee. Missing pt reconstruction at atlas. Journal of Physics: Conference Series, 645(1):012012, sep 2015.

[lis16] ATLAS list. Electron efficiency measurements with the ATLAS detector using the 2015 LHC proton-proton collision data. Technical report, CERN, Geneva, 2016. All figures including auxiliary figures are available at https://atlas.web.cern.ch/Atlas/GROUPS/PHYSICS/CONFNOTES/ATLAS-CONF-2016-024.

[LLL+08] W Lampl, S Laplace, D Lelas, P Loch, H Ma, S Menke, S Rajagopalan, D Rousseau, S Snyder, and G Unal. Calorimeter Clustering Algorithms: Description and Performance. Technical report, CERN, Geneva, 2008. All figures including auxiliary figures are available at https://atlas.web.cern.ch/Atlas/GROUPS/PHYSICS/PUBNOTES/ATL-LARG-PUB-2008-002.

[LY56] T. D. Lee and C. N. Yang. Question of parity conservation in weak interactions. Phys. Rev., 104:254–258, Oct 1956.

[Min17] Bartosz Mindur. ATLAS Transition Radiation Tracker (TRT): Straw tubes for tracking and particle identification at the Large Hadron Collider. Nucl. Instrum. Meth. A, 845:257–261, 2017.

[Mob16] Esma Mobs. The CERN accelerator complex. Complexe des accélérateurs du CERN. 2016. General Photo.

[Mor17] David M. Morse. Latest results on di-Higgs boson production with CMS. Latest results on di-Higgs boson production with CMS. Technical report, CERN, Geneva, 2017. LHCP 2017 Proceedings, CMS CR-2017/211.

[MOS23] Vanja Morisbak and Farid Ould-Saada. Search for new physics with atlas at lhc - z dilepton resonance at high mass. 02 2023.

[MtAC14] Zachary Marshall and the ATLAS Collaboration. Simulation of pile-up in the atlas experiment. Journal of Physics: Conference Series, 513(2):022024, jun 2014.

[Nis55] Kazuhiko Nishijima. Charge Independence Theory of V Particles*. Progress of Theoretical Physics, 13(3):285–304, 03 1955.

[NN53] Tadao Nakano and Kazuhiko Nishijima. Charge Independence for V-particles*. Progress of Theoretical Physics, 10(5):581–582, 11 1953.

[Noe71] Emmy Noether. Invariant variation problems. Transport theory and statistical physics, 1(3):186–207, 1971.

[OAA+14] Keith A Olive, Kaustubh Agashe, Claude Amsler, Mario Antonelli, Jean-Francois Arguin, David M Asner, H Baer, Henry R Band, RM Barnett, Tullio Basaglia, et al. Review of particle physics. Chinese physics C, 38(9):090001, 2014.

[Pat16] C. Patrignani. Review of particle physics. Chinese Physics C, 40(10):100001, oct 2016.

[Peq08] Joao Pequenao. Event cross section in a computer generated image of the atlas detector. 2008.

[Per00] Donald H. Perkins. Introduction to High Energy Physics. Cambridge University Press, 4 edition, 2000.

[Pes18] Michael E Peskin. An introduction to quantum field theory. CRC press, 2018.

[Pur12] Andrew Purcell. Go on a particle quest at the first CERN webfest. Le premier webfest du CERN se lance à la conquete des particules. page 10, 2012.

[RS99] Lisa Randall and Raman Sundrum. Large mass hierarchy from a small extra dimension. Physical Review Letters, 83(17):3370–3373, oct 1999.

[Sal68] Abdus Salam. Weak and Electromagnetic Interactions. Conf. Proc. C, 680519:367–377, 1968.

[WAH+57] C. S. Wu, E. Ambler, R. W. Hayward, D. D. Hoppes, and R. P. Hudson. Experimental test of parity conservation in beta decay. Phys. Rev., 105:1413–1415, Feb 1957.

[Wei67] Steven Weinberg. A model of leptons. Phys. Rev. Lett., 19:1264–1266, Nov 1967.

[WO22] R. L. Workman and Others. Review of Particle Physics. PTEP, 2022:083C01, 2022.